Universität Stuttgart

Coarse-Grained Simulations of Molecular Catalysis in Confined Spaces

Von der Fakultät für Mathematik und Physik der Universität Stuttgart zur Erlangung der Würde eines Doktors der Naturwissenschaften (Dr. rer. nat.) genehmigte Abhandlung

Vorgelegt von
Ingo Tischler
aus Ludwigsburg

Hauptberichter: Prof. Dr. Christian Holm

Mitberichter: Prof. Dr. Johannes Roth

Tag der mündlichen Prüfung: 30.10.2023
Institut für Computerphysik der Universität Stuttgart
2023

Contents

Contents

Zusammenfassung

Katalysatoren sind chemische Stoffe, welche die Aktivierungs-
energie einer chemischen Reaktion senken ohne bei der Reakti-
on selbst verbraucht zu werden. Obendrein ermöglicht die Re-
duktion der Aktivierungsenergie, dass viele Reaktionen über-
haupt stattfinden können. Aufgrund dieser Eigenschaften sind
Katalysatoren für die heutige Industrie essenziell. Schätzungs-
weise werden katalytische Prozesse bei der Herstellung von
mehr als 80 % aller chemischen Produkten verwendet [1]. Auf-
grund dieses Bedarfs an Katalysatoren sind Möglichkeiten um
eben jene Prozesse zu optimieren ein wichtiges Ziel der aktu-
ellen Katalyseforschung.

Ein vielversprechender Ansatz zur Verbesserung katalyti-
scher Eigenschaften ist der Einschluss eines molekularen Kata-
lysators in nanoporösen Medien. Die Idee hierfür ist die Nach-
ahmung von Biokatalysatoren, sogenannten Enzymen. Wäh-
rend der katalytischen Reaktion an einem Enzym, wird ein
Substratmolekül selektiv mittels des Schlüssel-Schloss Prinzips
an das Enzym gebunden. Dadurch findet die Reaktion im-
mer unter den gleichen Rahmenbedingungen statt, was dafür
sorgt, das keine unerwünschten Nebenreaktionen stattfinden.
Der Einschluss des molekularen Katalysators in nanoporösen
Medien sorgt zudem dafür, dass die Freiheitsgrade der Mole-
kulardynamik eingeschränkt werden und die Reaktion dadurch
selektiver wird. Um diese Einschlusseffekte zu erforschen und
nutzbar zu machen wurde der Sonderforschungsbereich (SFB)

Contents

1333 ins Leben gerufen. Die hier vorliegende Dissertation ist als Teilprojekt dieses SFBs entstanden.

In Rahmen dieses Projektes wurden Computersimulationen angewandt um genauen Mechanismen zu verstehen, welche bei Reaktionen von eingeschlossenen molekularen Katalysatoren auftreten. Zunächst betrachteten wir diese Systeme im Allgemeinen um dabei die Transporteigenschaften der Reaktanten besser zu verstehen. Als Methode hierfür wurde ein Kontinuumsansatz gewählt. Anschließend wurden die Simulationen immer weiter verfeinert um die Lücke zur atomistischen Größenskala zu schließen.

Mit den Simulationen auf der Kontinuumsskala sollte der Substrattransport zum und weg vom Katalysator untersucht werden, um damit die Porengeometrie und die Position des Katalysators in der Pore optimieren zu können. Dazu wurde ein finite Volumen Advektions-Diffusions-Reaktions Löser verwendet. Da der Porendurchmesser im Bereich von wenigen Nanometern liegt, mussten bei dieser Methode auch thermische Dichtefluktuationen Berücksichtigt werden. Nachdem die Methode zusammengesetzt und getestet war, stellte sich jedoch heraus, dass die Reaktionsprozesse für die Katalyse in nanoporösen Medien viel langsamer ablaufen als die Diffusionsprozesse. Dadurch verteilen sich entstehende Reaktionsprodukte praktisch gleichmäßig in der Simulationsbox, ohne dass sich zur Untersuchung wichtige Dichtegradienten hätten ausbilden könnten.

Nachdem sich dieser Kontinuumsansatz sich als nicht zielführend herausstellte, wendeten wir uns eines detailreicheren coarse-grained Simulationsmodell zu. Dazu betrachteten wir die ringschließende Metathese Reaktion, bei der der Effekt des

Einschlusses bereits experimentell gezeigt werden konnte [2, 3]. Bei dieser Reaktion geht es darum, das eine Oligomerkette mit sich selbst einen Ringschluss bildet. Dabei kann es aber auch passieren, dass das Oligomer mit anderen Oligomeren in seiner Umgebung reagiert, was eine Polymerisation zur folge hat. Grundsätzlich können immer beide dieser Reaktionswege auftreten. Der Effekt des Einschlusses wirkt sich bei dieser Reaktion so aus, dass Ringschließungen gefördert und Polymerisationen unterdrückt werden. Um die genauen Gründe für dieses Verhalten zu erfahren wendeten wir zunächst Polymertheorie an. Dazu betrachteten wir zunächst Random-Walk Modell eines Oligomers, welches in einem Abstand d zu einer flachen reflektierenden Wand startet. Dabei konnte gezeigt werden, dass dieses Oligomer einen durchschnittlich kleineren Ende-zu-Ende Abstand aufweist als ein freies Oligomer. Ebenso gilt für diesen Fall auch, dass die beiden Enden des Oligomers häufiger in einem für eine ringschließende Reaktion relevanten Abstand zu finden sind. Dabei konnte ein optimaler Abstand ermittelt werden, in welchem das Oligomer zur Wand festgehalten werden sollte, um die Wahrscheinlichkeit für einen Ringschluss zu optimieren. Diese polymertheoretische Analyse wurde mittels einer Molekulardynamik Simulation geprüft und reproduziert.

Das die bisherige Analyse immer nur ein Oligomer und eine flache Wand in Betracht zog, wurde im Rahmen einer weiteren Forschung nun auch Porensystem in denen viele Oligomere in Lösung vorliegen untersucht. Dazu musste zunächst einmal ein grobkörniges Molekulardynamik-Reaktionmodell entwickelt werden. Dieses wurde dann auf verschiedene Systeme angewendet um bei denen dann Wandeffekte, Einschlusseffekte und Krümmungseffekte untersucht wurden. Dabei konnte ge-

zeigt werden, dass all diese Effekte einen positiven Einfluss auf die Bildung von Ringpolymeren haben. Zum Teil konnten diese Effekte dadurch erklärt werden, dass die lokale Oligomerdichte in der Nähe einer Wand oder in der Pore geringer ist, als im Rest des Systems.

In einem realen Experiment kommen wesentlich mehr Effekte zum tragen als die hier untersuchten, wie zum Beispiel dipolare Molekülwechselwirkungen. Jedoch ist das Resultat eine Überlagerung aller möglichen Effekte, welche sich experimentell nur nur schwer individuell untersuchen lassen. Wie in dieser Dissertation erneut gezeigt wird, bieten Simulationen eine wichtiges Werkzeug, diese komplexen Systeme zu abstrahieren und dabei wichtige Erkenntnisse zu gewinnen.

1. Introduction

Catalytic reactions are an essential part of today's industry. It is estimated that more than 80% of all chemically manufactured goods are produced using catalysis [1]. Examples include everyday plastics, pharmaceuticals, cosmetics or ammonia for use in fertilizers via the Haber process, which alone is responsible for an estimated 1% of total global energy consumption [4]. The reason catalysis is so widely used in industry is because of its ability to speed up a reaction and change the selectivity to favor the desired products. This is what made many reactions possible in the first place.

This heavy use of catalysis therefore requires a high level of research to find new catalytic reactions or improve existing ones. These improvements can be both economic and environmental. For example, the goal might be to make a reaction faster, cheaper and easier to apply on an industrial scale. On the other hand, it is also desirable to look for another reaction pathway that produces less, possibly toxic, waste as byproducts.

Enzymes are a special type of catalyst. These biocatalysts are large, complex proteins that are essential for many of life's processes such as metabolism. Over billions of years of evolution, each enzyme has been perfected to catalyze one particular reaction. This specialization makes enzymes the fastest known catalysts in organic chemistry [5] and on top of that they rarely produce waste products. The disadvantage is that

1. Introduction

they can only catalyze reactions in a very narrow range of environmental parameters such as temperature or pH.

It is therefore only natural that research into improving catalysts tries to imitate some of the properties of enzymes. One of these properties is that the substrate binds to the enzyme prior to the reaction, thereby reducing its molecular degrees of freedom. The reaction can then only take place at a locally confined reactive site of the enzyme. Inspired by these confinement induced effects, scientists found different ways utilize them to improve the catalytic properties [6, 7, 8, 9, 10]. This approach of mimicking biocatalysis led to the founding of **C**ollaborative **R**esearch **C**enter (CRC) 1333, within the framework of which the research of this dissertation was carried out.

The title of CRC 1333 is: "Molecular Heterogeneous Catalysis in Confined Geometries". A molecular catalyst is a single molecule that drives a reaction without being consumed by it. A catalytic reaction is called heterogeneous when the catalyst and the reacting substrates are not in the same state of matter. This may be that liquid substances flow over a catalytic surface or, in the case of molecular catalysis, that the catalysts are bound to a surface. To reduce the degrees of freedom the catalysts are confined in a porous medium with an inner diameter of a few manometers. Therefore the aim of CRC 1333 is to research how molecular catalysis is influenced by confinement and develop methods to utilize these confinement effects. The scale of the nanoporous media was set to have a diameter of $2nm < d < 50nm$, which classifies them as meso pores.

The research of CRC 1333 was conducted from three different fields of study: materials, catalysis and analysis/simulations. The first field is concerned with porous materials in which the

catalysts can be anchored. Research was done on many different materials, such as **c**ovalent **o**rganic **f**rameworks (COFs) [11, 12] or mesoporous silica [13]. Here it was investigated how these different materials can be produced and provided with "docking sites" in order to later anchor the catalyst to them.

For the catalysis research, as a central field of study of the CRC, various reactions were tested to qualify and quantify the effects of confinement. One reaction that showed a significant molecular confinement effect was the ring-closing metathesis reaction, in which an enhanced formation of cyclic oligomers was observed [2, 3].

The field of simulation and analysis acts as a supporting filed for the others disciplines. On the one hand, the analysis approach used and improved methods to measure the pore structure, such as atomic probe tomography [14, 15], or obtained information on where exactly the catalysts are located in the pore, using **n**uclear **m**agnetic **r**esonance spectroscopy (NMR)[16]. On the other hand, simulations on different scales were used to gain insights into the mechanisms involved. At the quantum scale, **d**ensity **f**unctional **t**heory (DFT) simulations were used to study the reaction mechanisms [17] or the structuring process of COFs [18]. At the atomistic scale, adsorption processes within the pore were analyzed by **a**ll-**a**tom **m**olecular **d**ynamics (AA-MD) simulations [19]. On the larger scales, the simulations of this project took place.

The goal of this project was to investigate the substrate transport processes in and within the pores. We decided to take a top-down approach, starting with a continuum-level simulation and later moving on to more refined methods, thus closing the gap on the system scale with the other simulation

1. Introduction

projects of CRC 1333.

When analyzing the catalytic porous system on the continuum scale, we are not dealing with a set of discrete substrate particles, but with locally dependent particle densities within a flow field. In the scale of this approximation, the density distribution follows the dynamics of diffusion and advection. Thus, any local density spreads out and also moves with the fluid in which it is dissolved. These laws of MD are expressed by a set of **p**artial **d**ifferential **e**quations (PDEs). For the simulation these equations are solved numerically. The PDEs also need to be modified to account for reactions and catalytic boundary conditions. However, due to the small size of the pores, we arrive at a length scale where thermal density fluctuations can be important, especially if observables of the system are non-linearly dependent on the fluctuating density. This the case for many reactions.

The investigation done with the continuum model is discussed in Chapter 3. The aim was test such a thermalized advection-diffusion-reaction model to see if it could be used to analyze transport through the nanopores containing the catalysts. For the implementation we used two software packages: `ESPResSo` [20] and `pystencils` [21]. Once the implementation was complete, we were able to validate it against various analytically solvable systems. The code was also bench marked to show its excellent scaling behavior. In the end, however, it turned out that the molecular reactions are relatively slow compared to the diffusion within the pore, so that the density profile is essentially homogeneous and the system is in diffusive equilibrium.

Since the continuum approach was unfit to model molecu-

lar catalysis under confinement, we switched to mode detailed, **c**oarse-**g**rained **m**olecular **d**ynamics simulations (CG-MD). The reaction we modeled in this way was the ring-closing metathesis reaction, because the confinement seemed to have a direct influence on the polymer structure, which should be possible to reproduce with CG-MD. To test whether this was true, a random walk analysis was carried out beforehand. This study is described in detail in Chapter 4, where we solved the problem analytically to investigate the effects of a reflective flat wall on a polymer random walk that arises near it. This study showed that the probability of the random walk ending near its origin increases when there is a wall nearby, which should also result in an increase in the probability of the ring closing metathesis reaction.

With this theoretical investigation as a basis, we continue with the CG-MD simulation in Chapter 5. We have developed a reaction model in which particle bonds are formed when certain particles collide and are broken at a given rate. The catalyst to which the particles attach is placed in different geometries to disentangle the various surface, confinement and curvature effects that are all present simultaneously in the experiments. With this approach, we have succeeded in measuring effects of a similar magnitude to those observed in the experiments, but with the addition of gaining insights into how these effects are composed.

The work of this dissertation has been partially published in these publications:

> **I. Tischler**, F. Weik, R. Kaufmann, M. Kuron, R. Weeber, C. Holm. "A thermalized electrokinetics model including stochastic reactions suitable for multiscale sim-

ulations of reaction-advection-diffusion" In: *Journal of Computational Science*, 63:101770, September (2022)
URL: https://doi.org/10.1016/j.jocs.2022.101770
Data repository: https://doi.org/10.18419/darus-2258

I. Tischler, A. Schlaich, C. Holm. "The presence of a wall enhances the probability for ring-closing metathesis: insights from classical polymer theory and atomistic simulations" In: *Macromolecular Theory and Simulations*, 30(2):2000076, March (2021)
URL: https://doi.org/10.1002/mats.202000076
Data repository: https://doi.org/10.18419/darus-1371

I. Tischler, A. Schlaich, C. Holm. "Disentanglement of surface and confinement effects of the diene metathesis reaction in mesoporous confinement" In: *ACS Omega* (2023)
URL: http://doi.org/10.1021/acsomega.3c06195
Data repository: https://doi.org/10.18419/darus-3642

There were also contributions towards a chapter of a book:

R. Weeber, J.-N. Grad, D. Beyer, P. M. Blanco, P. Kreissl, A. Reinauer, **I. Tischler**, P. Košovan, and C. Holm. "ESPResSo, a versatile open-source software package for simulating soft matter systems" In *Reference Module in Chemistry, Molecular Sciences and Chemical Engineering* Elsevier (2023).
ISBN: 978-0-12-409547-2
URL: https://doi.org/10.1016/B978-0-12-821978-2.00103-3

2. Theoretical Background

In this chapter, the knowledge required for understanding the further chapters will be recapitulated. First we give an overview of catalysis (Section 2.1) and deepen our understanding using the ring-closing metathesis reaction. Because this reaction depends on the properties of oligomers, an insight into polymer physics is provided in Section 2.2. Lastly, the numerical methods used in this work are described in Section 2.3, which range from coarse-grained molecular dynamic to continuum simulations.

2.1. Catalysis

Chemical reactions are processes in which reactants are converted into products. These processes can be either endothermic, meaning that they consume energy, or exothermic, meaning that they produce energy. The change in energy in a reaction system is called the Gibbs energy

$$\Delta G = \Delta H - T\Delta S \quad , \tag{2.1}$$

consisting of the heat difference or enthalpy ΔH and an entropy-related change $T\Delta S$. In order for a reaction to get started, an energy barrier must usually be overcome. This activation energy E_a is energy needed to break-up of the internal structure of the reactants, which then rearrange to form the product. This activation energy is usually overcome by heating up the
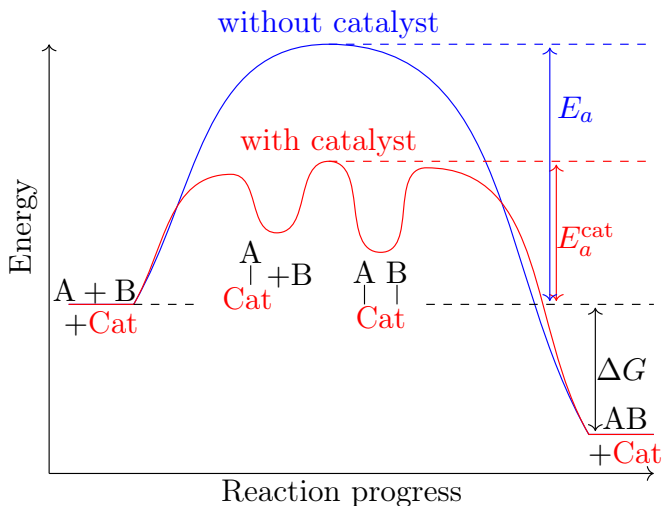
Figure 2.1.: Energetic levels during the reaction process with and without catalyst. The example reaction has the form A + B → AB. The reaction pathway with the catalyst has a smaller activation energy $E_a^{\mathrm{cat}} < E_a$, but the energy difference ΔG between the reactants and the product remains the same.

reactants. To lower this activation energy, a catalyst can be used. A catalyst is a substance that can chemically bind to the reactants, facilitating the breaking of the bonds. Once the reaction is complete, the catalyst returns to its initial state and can catalyze the reaction again. The different energy levels of a reaction with and without a catalyst are shown in Figure 2.1.

The reduction of the activation energy completely changes the kinetics of a reaction. The speed of a reaction is defined by

its reaction rate R, which describes the change in concentration over time. The dependence of the reaction rate on the different reactant concentrations is given by the rate equation:

$$R = k \prod_i c_i^{\alpha_i} \quad , \tag{2.2}$$

where k is the reaction rate constant, c_i is the concentration of the various reactants i and α_i denotes the partial order of that reactant. While it may be simple to say that a catalyst changes the rate constant, in reality the matter is more complex [22]. In the various elementary reaction steps in which the reactants react with the catalyst, the order may be partial, negative or even dependent on other reaction steps. This complexity can mean that catalytic reactions do not obey the power law of the rate equation. However, in many cases this is still a good approximation.

Apart from the fact that the reaction can be carried out at a lower temperature, a catalyst also makes many reactions possible in the first place. For the same group of reactants, there can be several different reactions that can occur. These different reactions also have different activation energies. So when the lowest energy barrier is overcome during heating, this reaction starts and consumes the reactants. This can be denaturation of the reactants or some other undesirable reaction. A catalyst designed for a specific reaction sets the activation energy of the desired reaction to the lowest and thus enables the synthesis of the desired product.

Catalysts can be classified into homogeneous and heterogeneous catalysts [23], depending on whether the catalyst and the reactants are in the same or in a different state of matter. Heterogeneous catalysts are often metals that are processed to

have a large surface area. The reactants come in contact with them in liquid or gaseous form. Due to the stability of these catalysts, heterogeneous catalysis can be carried out at very high temperatures, resulting in a high reaction throughput. In addition, they can be easily scaled up for industrial purposes.

Homogeneous catalysis, on the other hand, usually involves organic molecules with a metal atom in their reactive center. These organometallic complexes are dissolved in a solution with the reactants. This means that the catalyst is always in contact with the reactants, so that the reaction takes place throughout the entire solution. After the reaction is complete, the catalyst and the products must be separated again. The thermal stability of the catalyst complex also determines the maximum temperature at which the reaction can be carried out. However, the benefit of the homogeneous catalysis is that the catalyst molecules can be customised to perform one specific desired reaction.

Another classification of catalysts are biocatalysts or enzymes. They are made of amino acids and are much more complex than normal molecular catalysts, but have enormous advantages in terms of reaction selectivity and speed [5]. One mechanism that makes them so superior is their binding site and catalytic site. The binding site controls which molecules can bind to it, and once a molecule is bound, the enzyme wraps itself around the reactant. This restricts the conformations of the molecule and forces the reactive site to act at the exact location of the reactant. When the reaction is complete, the enzyme opens up and releases the product. The problem with using enzymes, however, is that they are too complex to model them from scratch, which means that we can only use enzymes

that are known from nature, or use gen manipulation to modify existing ones [24].

When looking for the improvement of an existing catalytic reaction, three properties have to be considered: Speed, stability and selectivity. The speed of a reaction is defined by the reaction rate R, which indicates how much reactant can be converted into a product over time. Stability indicates how many reactions a single catalyst can undergo before it becomes inactive. Even if catalysts are not consumed by the reactions, they can still become inactive, e.g. through denaturation or when a reaction molecule gets stuck on the catalyst. However, these events are unlikely. Stability is described by the **turn**over **n**umber (TON), which indicates the average number of reactions in a catalyst's life cycle. An ideal catalyst does not deactivate and therefore has a TON of infinity. For real molecular catalysts the TON are typically in the range between 10^2 and 10^4, but may also reach up to 10^6 [25]. Since undesirable side reactions occur in many reactions, the selectivity S is a measure of how likely it is that the desired reaction will occur. It can be quantified by the amount of desired and total product produced:

$$S_{\text{wanted}} = \frac{N_{\text{wanted}}}{N_{\text{total}}} \quad .$$ (2.3)

An important topic in the field of catalysis improvement are confinement effects, which occur when the catalytic reaction takes place in a very confined space. Confinement effects is a very broad term, because they summarize a variety of different effects that occur simultaneously when the catalytic process takes place in confinement. There are also many ways apply the confinement to a catalyst. One example are zeolites

[26, 27], which are microporous, crystalline aluminosilicate materials with pore sizes of $d < 1$nm. In these zeolites, larger molecules flowing through them are restricted in their movement, forcing a structural change. This allows them to adsorb onto the material, which releases heat. This heat of adsorption is then sufficient to trigger the reaction on the molecule [28]. As we can see, there are many different effects at play, such as surface structure, pore size or adsorption strength, which add up to the confinement effect. It is also possible to use confinement in homogeneous catalysis, e.g. by using self-assembled container molecules [29, 30], which can be described as ring-shaped or hollow molecules where the reaction takes place in the center.

Within the research project of the **c**ollaborative **r**esearch **c**enter (CRC) 1333, we wanted to investigate the effects of confinement on molecular catalytic reactions. The confinement itself is achieved by anchoring the catalyst in a mesoporous medium with diameters of 2 nm $< d <$ 50 nm. One of the reactions selected for this purpose is described below.

2.1.1. Ring-Closing Metathesis

A particular group of catalytic reactions is known as olefin metathesis, for which its discoverers Robert H. Grubbs, Yves Chauvin and Richard R. Schrock were awarded the Nobel Prize in Chemistry in 2005 [31]. The reaction applies to a pair of carbon-carbon double bonds and swaps their bonding partners. An example of this is shown in Figure 2.2. It is a fairly simple reaction that also produces fewer hazardous by-products than many other organic reactions. Because this reaction only targets double bonds, it finds its uses in research where it can

$$R_1 - C = C - R_2$$
$$\xrightleftharpoons{\text{cat.}}$$
$$R_3 - C = C - R_4$$

$$
\begin{array}{cc}
R_1 & R_2 \\
| & | \\
C & C \\
\| & \| \\
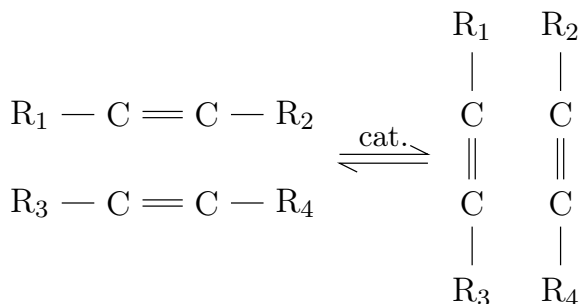C & C \\
| & | \\
R_3 & R_4
\end{array}
$$

Figure 2.2.: Schematic representation of the redistribution of the double bond partners in the olefin metathesis reaction. Note that only the double bonds are affected and the remainder attached to each carbon atom remains attached to the same atom. This is an idealized example because the molecules are not arranged in the same order, which means that the products end up containing any two of the residues R_1 to R_4.

be used to discover new candidates for pharmaceutical drugs [32]. Other industrial application would be the synthesis of substances like perfumes [33], or to refine products obtained from natural coal, gas or oil [34].

A special case of metathesis occurs when the reaction molecules have several olefin bonds in them. In the simplest case, this is an alkene chain in which the double bonds are located at both ends of the chain. When the reaction occurs between two chains, they join together to form a polymer chain that is twice as long and now has three double bonds, one at each
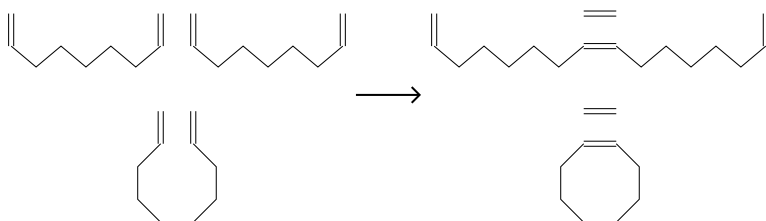
Figure 2.3.: Illustration of the different reaction pathways of diene metathesis. The polymerization is shown at the top, the ring-closing metathesis at the bottom.

end and one in the middle. This polymerization process can be repeated as long as a suitable substrate is available.

However, the reaction can also take a different path. Instead of rearranging the double bonds of two different alkene chains, two olefin bonds at the ends of the same molecule can fuse together. The resulting product is then a cycloalkene, giving this process the name ring-closing metathesis. An illustration of the two reaction pathways can be seen in Figure 2.3. The size of these cycloalkenes depends on the size of the substrate molecules, and if the alkene chain was long to begin with, the resulting ring-closed molecules are called macrocycles, which have numerous applications in medicine or industry [35, 36, 37, 38, 39].

Both of these processes also produce some ethylene, which is a free carbon atom pair connected by a double bond. Technically, it is possible for these ethylene molecules to again perform the metathesis reaction with the other products, thus reversing the reaction. However, due to their small size, the ethylene molecules evaporate relatively quickly and their absence sup-
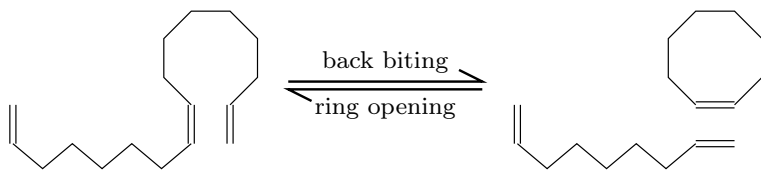
Figure 2.4.: Illustration of the backbiting reaction (left to right) or the ring opening polymerization (right to left).

presses this reverse reaction. Also, as long as the ring-closed and polymerized products remain in the system, their olefin bonds can again undergo metathesis reactions. Meaning that rings may open up and polymerize together in a process called ring opening metathesis polymerization. The end carbon pair of one polymer may also react with a carbon pair within their backbone, producing ring-closed products, as illustrated in Figure 2.4. This is then called back biting [40].

In diene metathesis, these pathways occur, but not with equal probability. The selectivity depends on which reaction events are more likely: that the ends of two different oligomers combine, or that the substrate bends enough to allow its two ends to react. This results in a so called ring-chain equilibrium [41], for which the ring-closing selectivity can be quantified as:

$$S_{RC} = \frac{N_{RC}}{N_{RC} + N_P} \quad , \tag{2.4}$$

where N_{RC} and N_P is the amount of ring-closed or polymerized products obtained during the reaction. This ring-chain-equilibrium is depending on the enthalpy and entropy of the system. Controlling which reactions take place is of interest for

industrial purposes, since one usually wants to obtain a particular product from a reaction. While for short chains the ring strain is the dominating energy contribution, for longer chains this can be neglected due to their higher flexibility [42]. A shift in selectivity toward polymerization can be achieved by a high substrate concentration [43]. The more oligomers present in the solution, the greater the likelihood that the ends of two oligomers will fuse together. In contrast, optimizing the reaction to promote ring closure is more complicated. Running the reaction at low concentrations increases the ring-closing selectivity, but is not feasible for large-scale production, because low substrate densities lead to low product densities. Because these macrocycle products can be used in many applications, it is desired to find ways to increase the ring-closing selectivity whilst running the catalysis at high substrate concentration. One way to overcome this limitation is to develop more stable catalysts, which live long enough to disassemble the product polymers to ring via the back-biting process[44].

Another approach to increase the selectivity of ring closure is to use confinement effects by placing the catalyst in mesopores and performing the reaction there. The idea behind this is that confinement restricts the configurations of the oligomers and forces them to coil up more [45]. However, this confinement introduces a multitude of different effects, like the interaction of the substrates with the pore surface or the influence of the curvature of the pore. These confinement effects are studied in the scope of the CRC 1333, under which the work for this thesis was carried out. In this work, simulation techniques are used to understand the experimental results performed by Ziegler et al. [2, 3] on this reaction and to find which confinement

effects can occur under which circumstances.

2.2. Polymer Physics

The diene metathesis reaction is a reaction of several polymer chains that can take place either inter- or intramolecularly, depending on the configuration of the polymers. To understand which of the two reactions takes place, a basic introduction to polymer physics [46] is required.

The word polymer can be derived from the Greek words "poly" and "mer", meaning "many parts", referring to molecules made up of many monomers, meaning "one part". When a polymer consists of only a "few parts", it is called an oligomer. The word monomer has slightly different meanings depending on the scientific background. Physicists use it to describe the individual repeating units of a longer polymer chain. Chemists, on the other hand, use it to describe a molecule that can be polymerized. This means that the substrate olefin chain of metathesis is called a monomer by chemists and a polymer/oligomer by physicists. However, this dissertation will continue to use the physics terminology.

A polymer can be considered as a set of N connected beads forming a chain, where N is large and the behavior is often in the limit of infinity. Technically, polymers can also have cross-links and branching, but here we restrict ourselves to linear polymers. While there are some properties that are trivial to transfer from the monomer to the polymer, such as mass, there are other properties that are not so intuitive. An example of this is how the diffusion coefficient of a polymer is determined from the diffusion coefficient of the monomers. Finally, there

are properties that can only be used to describe polymers and are not applicable to single monomers, such as how far apart the ends of the polymer are.

There are various models of varying complexity for analyzing polymers. The simplest model is the so-called random walk, in which all interactions between the monomers are ignored and the polymer is constructed step by step. With a discrete step size of l in one dimension, the polymer can be expressed as a sequence:

$$X_0 = 0 \tag{2.5a}$$

$$X_n = X_{n-1} \pm l \quad \text{with} \quad 0 < n \leq N - 1 \quad . \tag{2.5b}$$

If the chances of moving in either direction are equal, then the probability of the random walk ending at a position x is given by the binomial distribution:

$$\mathcal{P}(x, N) = l \binom{N}{x} 0.5^N. \tag{2.6}$$

Calculating the different moments of X_N yields:

$$\langle X_N \rangle = 0 \quad \text{and} \tag{2.7}$$

$$\left\langle (X_N - \langle X_N \rangle)^2 \right\rangle = \langle X_N^2 \rangle - \langle X_N \rangle^2 = l^2 N \quad . \tag{2.8}$$

This means that the random walk will most likely end at the origin, however, the average distance between the two end points is

$$d_{\text{e2e}} = \sqrt{\langle X_N^2 \rangle} = l\sqrt{N}. \tag{2.9}$$

Random walks in higher dimensions work similarly, where the direction of the step is chosen along a random axis. Figure 2.5 (left) shows such a random walk in two dimensions.
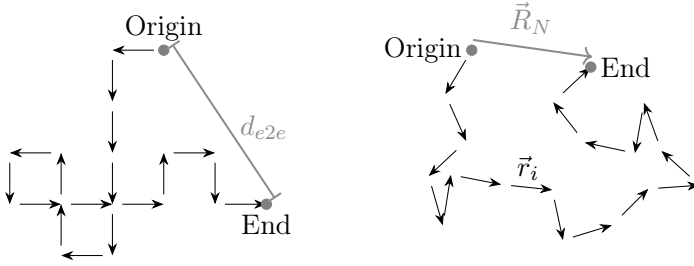
Figure 2.5.: Comparison of a 2D random walk (left) and a freely jointed chain (right).

The moments and the final distance for the random walk in higher dimensions remain the same as in one direction. This can be explained by the independence of the different directions, with the effective number of steps in each direction decreasing with the number of dimensions D, since only one of D moves on average occur in one particular dimension. The number of different dimensions and the effective number of steps per dimension cancel each other out

$$\langle \mathbf{X}_N \rangle = \mathbf{0} \quad , \tag{2.10}$$

$$\langle \mathbf{X}_N^2 \rangle - \langle \mathbf{X}_N \rangle^2 = \sum_i^N \frac{\langle \mathbf{X}_N^2 \rangle}{N} = l^2 N \quad . \tag{2.11}$$

If the direction of the steps is not restricted to the axis of one particular dimension, then the model becomes a freely jointed chain (Figure 2.5 right). With the directional step $\mathbf{r}_i$ ($|\mathbf{r}_i| = l$),

2. Theoretical Background

the end-to-end vector $\mathbf{R}_N$ is given as the sum of all steps:

$$\mathbf{R}_N = \sum_{i=1}^{N} \mathbf{r}_i \quad . \tag{2.12}$$

Because of rotational symmetry the first moment and the average ending position is again the origin:

$$\langle \mathbf{R}_N \rangle = \mathbf{0} \quad . \tag{2.13}$$

The variance requires some small calculations:

$$\langle R_N^2 \rangle = \left\langle \sum_{i=1}^{N} \mathbf{r}_i \cdot \sum_{j=1}^{N} \mathbf{r}_j \right\rangle = \sum_i \sum_j \langle \mathbf{r}_i \cdot \mathbf{r}_j \rangle = \sum_{i=1}^{N} l^2 = l^2 N \quad . \tag{2.14}$$

Here it was assumed that two different steps are completely uncorrelated

$$\langle \mathbf{r}_i \cdot \mathbf{r}_j \rangle = \delta_{ij} r_i^2 \quad . \tag{2.15}$$

Comparing Equations (2.11) and (2.15), we find that the variance for the freely jointed chain is the same as for the random walk. Since the directions of the different steps are independent and have uniform probability to point in any direction, the central limit theorem can be applied to obtain the probability density for the end of the chain.

$$\mathcal{P}(\mathbf{R}_N, N) = \left(\frac{D}{2\pi l^2 N} \right)^{\frac{D}{2}} e^{-\frac{D R_N^2}{2 l^2 N}} \quad . \tag{2.16}$$

Given a subset V, the probability $\mathcal{P}_V(N)$ of ending a random walk in V after N steps can be calculated by

$$\mathcal{P}_V(N) = \int_V P(\mathbf{R}_N, N) \mathrm{d}\mathbf{R}_N \quad . \tag{2.17}$$
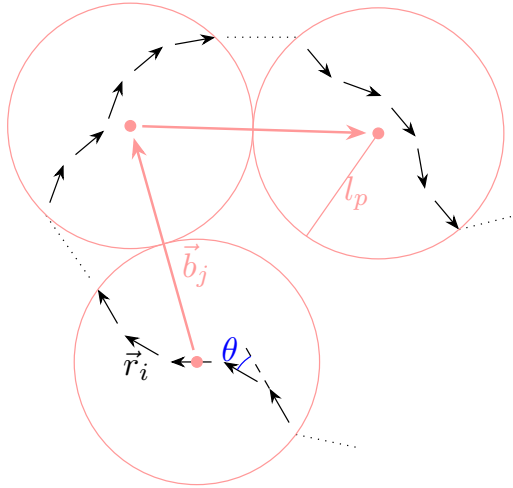
Figure 2.6.: Schematic of a freely rotating chain with the angle
θ between the steps. The segments of the chain are
joined to form a freely jointed chain with a larger
step size b. l_p shows the persistence length, which
is about half a Kuhn length in the limit of small
angles.

This idea, of where a polymer is likely to end is built upon and
used for the analysis in Chapter 4.

The next step to increase the complexity of the model is
to assume fixed bond angles θ between the steps, while the
rotation remains random, hence the name freely rotating chain.
With the addition of bond angles, this model represents a more
realistic polymer.

This gives the polymer some of its stiffness, but also leads
to correlations between the individual steps, which invalidates

the results of the earlier models. These correlations can be expressed by the occurring angle θ_{ij} between the steps $\mathbf{r}_i$ and $\mathbf{r}_j$. This model is much more difficult to handle on the scale where the steps are highly correlated. The correlation decays fast for monomers that are far apart in the chain. The length scale in the chain for which two steps are considered uncorrelated is called the persistence length l_p. Using l_p we can rescale this chain into a freely jointed chain with a larger step size. This new larger step groups the small correlated steps together so that these new steps are no longer significantly correlated. The resulting chain also has fewer steps than the original. This new step size is called the Kuhn length b and can be calculated as follows:

$$b = l\frac{1 + \cos\theta}{1 - \cos\theta}\frac{1}{\cos\frac{\theta}{2}} \quad , \tag{2.18}$$

For the detailed derivation of the Kuhn-length we refer to Rubinsteins "Polymer Physics" [46]. The number of segments in the rescaled chain $\tilde{N}$ is chosen so that the chains have the same maximum end-to-end distance $R_{\text{max}} = Nl$:

$$\tilde{N} = \frac{R_{\text{max}}}{b} = \frac{Nl\cos\theta}{b} \quad . \tag{2.19}$$

This approximation of short correlated steps to longer uncorrelated steps is shown in Figure 2.6. There are other models that restrict the rotation of the steps, for example, but the idea of how to deal with this is the same: we break down several correlated steps into fewer uncorrelated ones and use the freely rotating chain model to calculate other properties.

One such property would be a measure of the size of the polymer and how much space it occupies. While for linear polymers it is possible to use the average distance between the

ends for this, for other types of polymers, such as ring-shaped polymers, this property is undefined. Therefore, the gyration radius R_g is introduced, which is calculated from the average of the squared distances to the centre of mass $\mathbf{r}_{\text{com}}$ of each position:

$$\mathbf{r}_{\text{com}} = \frac{1}{N} \sum_{i=1}^{N} \mathbf{r}_i \quad , \tag{2.20}$$

$$R_g^2 \equiv \frac{1}{N} \sum_{i=1}^{N} (\mathbf{r}_i - \mathbf{r}_{\text{com}})^2 \quad . \tag{2.21}$$

R_g represents the effective length scale of which many different processes such as rotation take place. R_g gives some insight into the structure of a polymer, because it describes how the monomers are distributed in regards to the center of mass. For that reason R_g can be determined via light scattering experiments by measuring the angular dependence of the intensity of the scattered light. On the other hand R_g also gives us insights into the behavior of polymers near impenetrable walls. If a polymer is near an impenetrable surface, it is restricted in the possible number of configurations it can have. This reduction in the degrees of freedom also leads to a decrease in entropy. For a polymer in solution that means, that due to entropic reasons it is less likely that its center of mass is located in a volume close to a impenetrable surface than in a volume without any boundary present. While this is already the case when one end of the polymer is R_{max} from the boundary, it is negligible until the distance is within the length scale of R_g. For these and shorter distances, the number of configurations decreases significantly, leading to lower and lower densities near
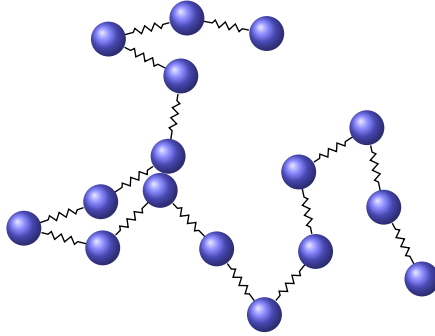
Figure 2.7.: Illustration of the bead-spring model.

the wall. A more detailed impact of the changes imposed on the configurations is discussed in Chapter 5.

We now move from the static description of polymers to the dynamic one. On long time scales, a polymer can be seen as a single large particle that is subject to diffusion and is entrained by the solvent. How large this particle is and how much friction it has is determined by the structure of the polymer. One model for analyzing polymer behavior is the so-called Rouse model [47]. This model assumes that the polymer is an ideal chain of beads connected by springs, hence the name "bead-spring model". A schematic representation of this model can be seen in Figure 2.7. The model is defined by the spring length b and the number of beads $\tilde{N}$. There are no excluded volume effects of the beads and they interact with each other only through the connecting springs with spring constant k. Each bead is coupled independently to the surrounding medium via the friction coefficient γ. This results in the following Langevin

equation of motion of the individual beads:

$$\gamma \frac{\partial \mathbf{r}_i}{\partial t} = k \left(\mathbf{r}_{i-1} - 2\mathbf{r}_i + \mathbf{r}_{i+1} \right) + \mathbf{f}_i \quad , \qquad (2.22)$$

where $\mathbf{f}_i$ is a thermal noise term. The acceleration term is missing because for the time scales of interest it becomes negligible. The system is therefore overdamped. The thermal noise obeys ther fluctuation dissipation theorem and is defined by

$$\langle \mathbf{f}_i(t) \rangle = \mathbf{0} \qquad \text{and} \qquad (2.23\text{a})$$

$$\langle \mathbf{f}_i(t)\mathbf{f}_j(t') \rangle = 6\gamma k_\mathrm{B} T \delta(t - t')\delta_{ij} \quad . \qquad (2.23\text{b})$$

Because we are in a thermal system we can rewrite the spring constant in terms of the thermal energy $k = \frac{3k_\mathrm{B}T}{b^2}$. When being in the limit for long times, the friction of each bead on average acts separately on the polymer. This means that the effective friction coefficient γ_eff that the polymer experiences, can be expressed as the sum of the individual friction of the beads:

$$\gamma_\mathrm{eff} = \tilde{N}\gamma \quad . \qquad (2.24)$$

Within this limit of long times we can apply the Einstein-Smoluchowski [48, 49] relation to translate the friction into a diffusion coefficient:

$$D_\mathrm{eff} = \frac{k_\mathrm{B}T}{\gamma_\mathrm{eff}} = \frac{k_\mathrm{B}T}{\tilde{N}\gamma} \quad . \qquad (2.25)$$

However, this assumption of a single diffusion coefficient only works on longer time scales. On short time scales, the internal elasticity of the connected springs becomes relevant. The time scale is defined by the Rouse time τ, which is the

relaxation time of the movement of the beads perpendicular to their spring axis. As long as these normal motions of the beads are in equilibrium, D_{eff} is a good approximation to the diffusion coefficient.

For a good derivation of the relaxation time of the bead spring model by solving the coupled differential equation of the bead motion, I recommend Ref.[50]. In the end, τ turns out to be:

$$\tau = \frac{b^2 \tilde{N}}{3\pi^2 D_{\text{eff}}} = \frac{\gamma \tilde{N}^2 b^2}{3\pi^2 k_{\text{B}} T} \quad . \tag{2.26}$$

While the Rouse model can predict the behavior of polymer melts quite well, the deviation from the experiments for polymers in solution is quite large. This is due to the neglect of the hydrodynamic interaction. Therefore, Zimm [51, 52] improved Rouse's model to take into account the hydrodynamic interaction between the beads. This interaction potential $\mathbf{H}_{ij}$ between different beads decreases with the reciprocal distance of these beads. However, since this non-linear tensor function is difficult to handle, it is usually used as the mean value around which it fluctuates in the equilibrium state. There it reads:

$$\langle \mathbf{H}_{ij} \rangle = \frac{1}{6\pi\eta} \left\langle \frac{1}{|\mathbf{r}_j - \mathbf{r}_j|} \right\rangle \quad , \text{ for } i \neq j \tag{2.27}$$

with η being the viscosity of the solvent. Including this into the Langevin equation (Equation (2.22)), leads to:

$$\frac{\partial \mathbf{r}_i}{\partial t} = \sum_j^{\tilde{N}} \langle \mathbf{H}_{ij} \rangle \left[k \left(\mathbf{r}_{j-1} - 2\mathbf{r}_j + \mathbf{r}_{j+1} \right) + \mathbf{f}_j \right] \quad , \tag{2.28}$$

Since the friction to which the beads are subjected comes from the solvent, it can be shown that the coefficient of friction

of the Rouse model is translated into the viscosity of the Zimm model via the following relationship:

$$\eta = \frac{8\gamma}{3b\sqrt{N}\sqrt{6\pi^3}} \quad . \tag{2.29}$$

With this the relaxation time and the diffusion coefficient turn out to be:

$$\tau = \frac{\eta b^3 \tilde{N}^{\frac{3}{2}}}{\sqrt{3\pi}k_\mathrm{B}T} \approx 0.325 \frac{\eta R_g^3}{k_\mathrm{B}T} \qquad \text{and} \tag{2.30}$$

$$D = \frac{8k_\mathrm{B}T}{3\sqrt{6\pi^3}\eta b\sqrt{N}} \approx 0.196 \frac{k_\mathrm{B}T}{R_g} \quad , \tag{2.31}$$

where the approximation of the radius of gyration via the Flory exponent ν [53] was used:

$$R_g = b\tilde{N}^\nu \quad . \tag{2.32}$$

The Flory exponent is a measure of how good or bad a solvent is for a particular polymer. If it is a bad solvent, the polymer tends to curl up to reduce its effective surface area with the solvent ($\nu \approx 1/3$). The opposite is true for a good solvent, where the surface area is increased by expansion ($\nu \approx 3/5$). For the derivation, a θ solvent ($\nu = 0.5$) was assumed, where the polymer behaves similar to a random walk.

Experiments show that the Zimm model is a much better model for describing polymers in solution and that the scaling of D and τ with the number of beads is correct. To simplify the hydrodynamic interactions of a polymer and a fluid, we can define a hydrodynamic radius R_H, which is the radius of a hypothetical sphere that has the same hydrodynamic properties

as the dissolved polymer. Since this is how the polymer interacts with the solvent on average, the ensemble average can be obtained from dynamic light scattering measurements. Theoretically, this can be calculated by averaging the reciprocal of the distance between the beads, which is a measure of how strongly these beads are connected by hydrodynamics:

$$\frac{1}{R_H} = \frac{2}{N\,(N-1)} \sum_{i=0}^{N} \sum_{j>i}^{N} \frac{1}{|\mathbf{r}_i - \mathbf{r}_j|} \quad . \qquad (2.33)$$

This property can be used to validate polymer models from molecular dynamic simulations by comparing them with experimental values.

From this we can conclude that the hydrodynamic radius influences the diffusion coefficient:

$$D_{\text{eff}} = \frac{k_{\text{B}}T}{6\pi\eta R_H} \quad . \qquad (2.34)$$

The diffusion coefficient obtained from Equations (2.31) and (2.34) are slightly different, where the difference between them can usually neglected.

2.3. Numerical Methods

We use the language of mathematics to describe the world as it is. However, due to the ever-changing nature of things, the resulting equations usually turn out to be systems of differential equations. There is rarely a general analytical solution to these equations, so simplifications are necessary. These can be achieved by restricting the degrees of freedom of the system. In such an ideal world, physicists can make analytic predictions.

Reality, however, is usually not ideal. Instead of oversimplifying the system and finding an analytical solution, it is also possible to obtain a numerical solution by simulating a well-defined system.

A simulation can be understand as a virtual representation of a system, where the differential equations define the rules of that system. To handle the infinitesimal changes in the differential, they are approximated by small finite differences. Thus, time differentials can be discretized into a time step and space differentials into a grid. Then the system can be integrated step by step.

However, this requires a huge amount of calculations to be done. 100 years ago, such calculations were done by persons who did the computations, so called (human) computers. This was a slow and lengthy process. With the advent of digital computers in the 1940s, these numerical calculations became easier to perform. Since then, the technical complexity of computers has increased in accordance with Moore's Law [54], which states that the number of transistors in integrated circuits doubles every one to two years. This exponential growth in computing power has also made it possible to perform more complex simulations.

Simulations are now an essential part of industry and science, where they bridge the gap between theories and experiments. On the one hand, they can be used to check whether a theory is correct by replicating experimental results in a simulation. If they match, one can also analyze which processes lead to these results, which is not always possible experimentally. On the other hand, simulation can also predict the results of experiments. In this way, experiments can be better focused on

interesting points in the parameter space and the number of unnecessary experiments can be reduced.

Simulations can be applied on many different length and time scales. On the smallest scale, they are used to study quantum chemical problems by calculating the wave functions of electrons for a given number of atoms. In this way, one can gain insights into chemical reaction mechanisms or determine the structure of molecules. A commonly used method is the **d**ensity **f**unctional **t**heory (DFT) [55], which is used to find the solutions of the Kohn-Sham equations [56] to determine the electron wave functions. However, this leads to an eigenvalue problem that requires an enormous computational effort that scales with the number of electrons cubed ($\mathcal{O}(N^3)$). This method can therefore only be used for small systems (number of atoms < 1000).

One step higher on the scale ladder are the **m**olecular **d**ynamics (MD) simulations, in which the atoms form the system and the electronic structure is neglected. The motion of these atoms is described by Newton's equations of motion. Since atoms are only affected by atoms that are nearby, the computational effort scales linearly with the number of atoms ($\mathcal{O}(N)$). The number of atoms that can be processed can therefore be very large. It is also possible to combine several atoms into a larger bead, which further reduces the computational costs. This process is called **c**oarse-**g**raining (CG). MD simulations are used to study solvating behavior or diffusion processes in porous media.

For systems where the individual details of the atoms are irrelevant and only their collective properties become interesting, a continuum model can be used. Here, explicit particles are ap-

proximated by an implicit particle density that could be solved numerically by the Poisson equation or the Navier-Stokes equations. These partial differential equations are discretized on a grid, assuming that the local properties are homogeneously distributed within each grid cell. This discretization then allows the gradients to be calculated by the differential quotient of neighboring cells. Depending on the differential equations, there are different methods to solve them, e.g. the finite element method or the finite volume method, we will discuss the latter in more detail later. Since these methods can be applied wherever the underlying properties can be considered continuous, their range of application is very broad and extends from microfluidics across aerodynamics up to global weather forecasting.

Many scientific problems, such as catalysis in confinement, are usually too complex to simulate with just one of the above methods. There are many different things happening on many different scales: The reaction itself takes place on a quantum scale, the diffusion of the reactants on an atomistic scale, and the flow in and out of the confinement is large enough to be described as a continuum. Since there have been other projects in the CRC that look at the problem from the quantum and atomistic scales, a top-down approach was chosen for this project. Thus, we start at the continuum scale and then move on to coarse-grained MD simulations to capture all facets of the problem. Continuing in this section we go into the details of the simulation methods used.

2. Theoretical Background

2.3.1. Molecular Dynamic Simulations

The Integrator Scheme

Problems caused by the physical movements of atoms/particles can be analyzed using MD simulations. The forces acting on a particle determine its acceleration, velocity and position according to Newton's law of motion:

$$\mathbf{F}_i = m \cdot \mathbf{a}_i = m \cdot \dot{\mathbf{v}}_i = m \cdot \ddot{\mathbf{r}}_i \quad , \qquad (2.35)$$

where i denotes the index of the particle. The force $\mathbf{F}_i$ can either arise from an external field, or stem from the interaction of the particles $(\mathbf{F}_i(\mathbf{r}_1, \dot{\mathbf{r}}_1, \ldots, \mathbf{r}_N, \dot{\mathbf{r}}_N))$, which couple the equations of motion of the different particles. However, as long as the interactions between the particles are defined, it is possible to calculate the forces on each particle for a given snapshot. By incrementing the time t with small single time steps Δt and using a Taylor expansion of the velocity $\mathbf{v}_i(t+\Delta t)$ and the position $\mathbf{r}_i(t + \Delta t)$, the following update rules can be determined:

$$\mathbf{v}_i(t + \Delta t) = \mathbf{v}_i(t) + \Delta t \mathbf{a}_i(t) + \mathcal{O}(\Delta t^2) \qquad \text{and} \qquad (2.36a)$$
$$\mathbf{r}_i(t + \Delta t) = \mathbf{r}_i(t) + \Delta t \mathbf{v}_i(t) + \mathcal{O}(\Delta t^2) \quad , \qquad (2.36b)$$

where the $\mathcal{O}$ notation indicates the order of the neglected terms. The error scales with the highest term considered, which is of first order with the time step. According to these rules, the new particle positions and velocities are determined, from which this process can be repeated by calculating the forces at this new time. This simple method is called the

Euler method. However, it is rarely used because the error
scales linearly with the time step. On top of that the Euler
method shows an energy drift for many kinds of systems. A
better method that is often used is the Leapfrog method, where
the velocity is shifted by half a time step so that the derivatives
are not one-sided but centralized:

$$\mathbf{v}_i(t + \frac{\Delta t}{2}) = \mathbf{v}_i(t - \frac{\Delta t}{2}) + \Delta t \mathbf{a}_i(t) \qquad \text{and} \qquad (2.37a)$$

$$\mathbf{r}_i(t + \Delta t) = \mathbf{r}_i(t) + \Delta t \mathbf{v}_i(t + \frac{\Delta t}{2}) \quad . \qquad (2.37b)$$

This small change leads to a second order error and its sym-
metry makes it symplectic. A symplectic integrator ensures
that the resulting trajectory is still described by Hamiltonian
mechanics. This suppresses energy drifts and makes them fa-
vorable for long-term chaotic systems, like MD. For analytical
purposes, the velocity and positions should be read out sim-
ultaneously, which can be achieved by doing the velocity in-
tegration in two steps. This then leads to the Velocity-Verlet
algorithm, which is mathematically equaivalent to the Leapfrog
method and hence also symplectic:

1. Calculate the half step velocities: $\mathbf{v}_i(t + \frac{\Delta t}{2}) = \mathbf{v}_i(t) + \frac{1}{2}\Delta t \mathbf{a}_i(t)$.

2. Determine the new positions (2.37b).

3. Compute the new forces $\mathbf{F}_i(t + \Delta t)$ and accelerations $\mathbf{a}_i(t + \Delta t)$.

4. Update the second half step of the velocities: $\mathbf{v}_i(t + \Delta t) = \mathbf{v}_i(t + \frac{\Delta t}{2}) + \frac{1}{2}\Delta t \mathbf{a}_i(t + \Delta t)$.

Forces and Potentials

Once the integration rule has been established, we can move to calculating the forces. The forces acting on a particle can come from many different sources, for example external fields, frictional forces or interactions with other particles. They are usually independent and can simply be summed up. External forces in MD simulations are either predefined, such as a constant electric field in a capacitor, or arise from coupling with other methods, such as the flow field of a fluid in which the particles are dissolved. Frictional forces are discussed later in this section. The interaction between particles at the molecular level is defined by the electrons. On the one hand there are Coulomb and dipole interactions, which can be attractive or repulsive depending on the parity of the ionic charge or the orientation of the dipoles. But uncharged atoms also interact via their electrons, through van der Waals forces [57, 58] or the Pauli exclusion principle [59]. In the former, electron density fluctuations cause a local dipole moment. This also polarizes the electron density of the neighboring atoms and leads to an attractive force that rapidly decreases with distance. The Pauli principle, on the other hand, produces a strong repulsive force when the electron orbitals of two atoms collide. Electrons are fermions, and multiple fermions cannot occupy the same quantum state simultaneously. When two orbitals overlap, this principle is broken, so that the wave function of the electrons in this region becomes zero. The wave functions are thus pushed apart, which leads to a repulsive force.

A pair potential often used in simulations that combines the Van der Waals and Pauli forces is the **L**ennard-**J**ones potential

(LJ) [60]

$$U^{\mathrm{LJ}}(r_{ij}) = 4\epsilon \left[\left(\frac{\sigma}{r_{ij}} \right)^{12} - \left(\frac{\sigma}{r_{ij}} \right)^{6} \right] \quad , \qquad (2.38)$$

where $r_{ij} = |\mathbf{r}_i - \mathbf{r}_j|$ is the distance between the two interacting particles. ϵ and σ define the energy and length scales of the interaction. The term r_{ij}^{-12} models the repulsion due to the Pauli principle and the term $-r_{ij}^{-6}$ models the van der Waals attraction. The minimum of this potential is $U(r_{ij} > \sqrt[6]{2}\sigma) = -\epsilon$. Technically, this potential has an infinite effective range, but since it quickly drops to zero for distances $r_{ij} > \sqrt[6]{2}\sigma$, it is usually used in a truncated and shifted version, so that the potential acts only within the cut-off distance r_{cut}:

$$U_{\mathrm{trunk}}^{\mathrm{LJ}}(r_{ij}) = \begin{cases} U^{\mathrm{LJ}}(r_{ij}) - U^{\mathrm{LJ}}(r_{\mathrm{cut}}), & \text{for } r_{ij} \leq r_{\mathrm{cut}} \\ 0, & \text{for } r_{ij} > r_{\mathrm{cut}} \end{cases} .$$
$$(2.39)$$

For distances $r_{ij} > r_{\mathrm{cut}}$ the potential is set to zero, and to be continuous at this cut-off, the total potential is shifted by $U^{\mathrm{LJ}}(r_{\mathrm{cut}})$. Common values for the cut-off are between $2.5\sigma < r_{\mathrm{cut}} < 10\sigma$. However, when dealing with particles that do not attract each other, the limiting distance can be set to the spatial minimum of the potential $r_{\mathrm{cut}} = \sqrt[6]{2}\sigma$. This potential is then called the **W**eeks-**C**handler-**A**nderson (WCA) potential [61]. A diagram showing these different potentials can be seen in Figure 2.8.

While these potentials can be used to represent an inert gas of individual atoms, to represent molecules we need a way to describe the covalent bonds between the atoms. These chemical bonds are created by a pair of electrons located in a com-
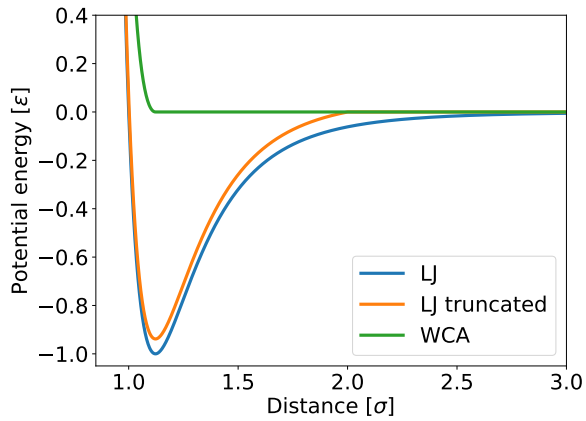
Figure 2.8.: Comparison of the LJ potential with the truncated and shifted LJ potential and the WCA potential. The cut-off for the truncated potential is $r_{\mathrm{cut}} = 2.0\sigma$.

mon orbital between two atoms. This system has its lowest energy at a certain distance, called the bond length r_{bond}. If the atoms are too far apart, the electrons pull them back together, and if the atoms get too close, the overlap of the orbitals has a repulsive effect. In simulations, these bonds are achieved by a potential that only acts on the bonded particles. The simplest model here uses a harmonic potential:

$$U^{\text{H}}(r) = \frac{1}{2} K^{\text{H}} \left(r - r_{\text{bond}} \right)^2 \quad ,$$

(2.40)

where r is the distance between the particles and K^{H} is the spring constant. This potential induces an harmonic oscillation around the bond length r_{bond}. However, in systems where the energy of the particles can vary locally, the amplitude of these fluctuations would also vary greatly. In reality, a large amplitude can break these bonds, but in MD simulations one wants to have static bonds. A more sophisticated potential that limits these fluctuations is the FENE (**f**inite **e**xtension **n**on-linear **e**lastic) potential [62]:

$$U^{\text{FENE}}(r) = -\frac{1}{2} K^{\text{FENE}} \Delta r_{\text{max}}^2$$
$$\cdot \ln \left[1 - \left(\frac{r - r_{\text{bond}}}{\Delta r_{\text{max}}} \right)^2 \right] \quad ,$$

(2.41)

where Δr_{max} is the maximum amplitude of the oscillations around the bond length before the potential diverges.

Another approach to modeling the bond interaction is the Kremer-Grest model [63], which uses the FENE potentials to represent the attractive part, while the repulsive part is taken

over by the WCA potential. So for the above equations, set $r_{\text{bond}} = 0$ and the oscillations will be around the minimum of $U^{\text{WCA}}(r) + U^{\text{FENE}}(r)$. This location can be set by K and Δr_{max}.

Molecules with three or more atoms are not only defined by the bond pair potentials of their atoms, but also have a certain internal structure. This results from the orbital arrangements of the atoms that have multiple bonds. Basically there is a preferred angle between two bonds. This bond angle ϕ_{bond} depends on the type and number of bonds that the central atom has. In simulations, harmonic potentials are often used for these type of bonds:

$$U^{\text{angle}}(\phi) = \frac{1}{2} K^{\text{angle}} \left(\phi - \phi_{\text{bond}} \right)^2 \quad . \tag{2.42}$$

In a full atomistic simulation, the torsion of the bonds can also be modeled in a similar way, but this is not relevant for the simulations used in this dissertation.

There are many different ways to parametrize the bonded and non-bonded potentials. These parametrizations are commonly known as force fields, which define all possible interactions of the particles within the system. The choice of force field depends strongly on the system and the properties one wants to analyze. For example, there are force fields such as OPLS [64], which is optimized for simulating the properties of liquids, or the AMBER force field [65], which is often used in protein research.

Once the potentials are defined, the forces can be calculated as derivatives of the potentials

$$\mathbf{F}_i = -\boldsymbol{\nabla} U_i^{\text{total}} \quad . \tag{2.43}$$

For the algebraic potentials described above, this can be done analytically; for others where this is not possible, a numerical derivative can also be used. The beauty of cut-off potentials is that they are constant after the cut-off distance and therefore do not introduce any force. This means that particles further apart than this distance do not exert a force on each other. Thus, the number of pairs of particles that must be considered to calculate the total force on each particle can be drastically reduced.

Periodic Boundary Conditions

Due to the limitation of computational hardware, an MD simulation takes place in a finite box. If the boundary of this box were impenetrable, the surface interactions with this box would have a significant influence on the dynamics of the system. This effect weakens with increasing system size thanks to the square-cube law. For example, in crystal lattices with 10^3 atoms, almost half of the atoms (488 out of 1000) are on the surface. For 100^3 atoms, the outer atoms make up only 5.9% and for 1000^3 it is 0.6%. However, it is not always possible to simulate larger systems just to reduce this effect. To get around this, **p**eriodic **b**oundary **c**onditions (PBC) are used, where, if a particle crosses the system boundary, its positions are folded to the opposing side of the system. Mathematically, the system behaves as if it were mapped onto a hyper-torus. The system thus repeats itself, and from within the system it appears to be infinite. This must also be taken into account when calculating the distances between particles, as the distance to the repeating particles across PBCs also plays a role. A common practice is that particles can only interact with the

nearest image of another particle, which is called the minimum image convention.

Thermalization

Microscopic physical systems are usually not completely isolated, but coupled to a reservoir with which energy, particles or volume are exchanged. Through this coupling, these extensive properties are transformed into their intensive counterparts such as temperature, chemical potential or pressure, which then define the ensemble.

Constant-energy MD simulations are rather uncommon because the integrator scheme used must be energy conserving over a long period of time. However, due to the limited precision of floating point numbers in computer hardware, rounding errors occur in the calculations, which can add up over time and cause a small energy drift. By simulating a canonical ensemble, where energy fluctuates and dissipates, this problem is circumvented. There are several methods to achieve a constant temperature. One of these is the Langevin thermostat [66], which uses the Langevin dynamics [67] as an extension of Newton's equation to calculate the drag force $\mathbf{F}_D(\mathbf{v}, t)$:

$$\mathbf{F}_D(\mathbf{v}, t) = -\gamma \mathbf{v} + \sqrt{2\gamma k_{\mathrm{B}} T} \, \boldsymbol{\eta}_i(t) \quad . \tag{2.44}$$

Here γ is the friction coefficient and $\boldsymbol{\eta}_i(t)$ is a random noise term acting on the particle i which satisfies α, β for all spatial coordinates:

$$\langle \eta_i^\alpha(t) \rangle = 0 \qquad \text{and} \tag{2.45a}$$

$$\left\langle \eta_i^\alpha(t) \eta_j^\beta(t') \right\rangle = \delta_{\alpha\beta} \delta_{ij} \delta(t - t') \quad . \tag{2.45b}$$

Each particle therefore experiences random, uncorrelated forces. The acceleration due to these "kicks" and the deceleration due to the drag force determine the velocities of the particles and ensure that the average kinetic energy follows:

$$\frac{m\bar{v}^2}{2} = \frac{3}{2}k_\mathrm{B}T \quad .$$

(2.46)

This thermostat controls the temperature of the system and is also used as an implicit solvent. The particles in the solution are subject to Brownian motion due to collisions with the solvent molecules. The forces resulting from the collisions are already dealt with in the Langevin equation, so that even freely moving particles move as if they were under the influence of Brownian motion. This means that solvent particles are not needed in the simulation, which frees up a lot of computing resources. However, the hydrodynamic properties of the solvent are neglected in the process, and it depends on the system whether the solvent should be represented explicitly or implicitly.

Grand Canonical Ensemble

Another type of ensemble is the grand canonical ensemble (μVT), in which a chemical potential μ defines the exchange of particles of the system and the reservoir. Such exchanges can be modeled by so-called **M**onte **C**arlo (MC) moves. These MC trial moves attempt to apply random particle exchanges to the system. Possible changes for which MC moves can be used are:

- Displacement of particles inside of the system

2. Theoretical Background

- Insertion of particles to the system

- Removal of particles from the system

Whether these trial moves are accepted or rejected is depending on the change in energy that the move exerts on the system. The acceptance probability follows the Boltzmann distribution:

$$\mathcal{P}_{\text{acc}} \sim e^{-\frac{\Delta E}{k_\text{B} T}} \quad . \tag{2.47}$$

This ensures that the system remains in thermal equilibrium. In addition, any move performed has a non-zero probability of being reversed. This principle is called detailed balance and ensures that any thermodynamically possible state can be reached.

In the **g**rand **c**anonical **M**onte-**C**arlo (GCMC) method, only insertion and removal moves are considered, while the motion is handled by MD. Either a new particle is inserted at a random position or a randomly selected existing particle is removed. The acceptance probability of any one of these moves depends on the probability that this specific move was chosen relative to the probability that the corresponding reverse move can be chosen. This is done to ensure detailed balance. Since an insertion move requires the new particle to be placed within a volume, the probability of selecting this move scales with $\alpha_{\text{in}} \sim \frac{1}{V}$. For a particle distance, a certain particle must be selected, so the probability scales with $\alpha_{\text{out}} \sim \frac{1}{N}$. Combining this with the Boltzmann distribution we can obtain the prob-

abilities of accepting the insertion $\mathcal{P}_{\text{in}}$ and removal $\mathcal{P}_{\text{in}}$ moves

$$\mathcal{P}_{\text{in}} = \min\left[1, \frac{V\Lambda^{-3}}{N+1}\exp\left(\frac{\mu - \Delta E}{k_{\text{B}}T}\right)\right] \qquad \text{and} \qquad (2.48\text{a})$$

$$\mathcal{P}_{\text{out}} = \min\left[1, \frac{N}{V\Lambda^{-3}}\exp\left(\frac{-\mu - \Delta E}{k_{\text{B}}T}\right)\right] \qquad . \qquad (2.48\text{b})$$

Here V is the volume of the system, Λ is the thermal de Broglie wavelength of the molecule, N is the number of molecules in the system before the shift, μ is the desired chemical potential and ΔE is the energy difference caused by the insertion/removal of the movement.

The procedure for GCMC is to alternate between a series of MD steps and multiple MC moves. The number of MD steps or MC moves should be large enough to ensure that the system in in a relaxed state and uncorrelated to the state before performing these moves or steps.

Coarse-Graining

The computational effort required to perform MD simulations increases with the number of particles in the simulation box. The exact scaling of the computational effort depends on the methods used and the system properties. In the ideal case, however, the scaling can only be linear. Often it is necessary to reduce the computational cost, because the system in question contains too many particles or has to be evaluated over a long period of time. One way to speed up the simulations is to use what is known as coarse graining (CG), in which several interconnected particles are combined into a single larger particle. Since these larger particles have different interaction

properties, a different force field must be used. For example, in a united-atom force field, a carbon atom of a polymer and the hydrogen atoms attached to it are treated as a single particle, rather than three or four particles. This coarse-graining can go even further, as in the MARTINI force field [68], where four of these one-atom carbon backbone particles are combined into one large sphere.

Although the reduction in the number of particles leads to an enormous acceleration of the simulation, it is also accompanied by a loss of details. Therefore, it must be examined with caution how and to what extent the missing details influence the properties of the system one is interested in.

This concludes the introduction to MD simulations, which are necessary for a better understanding of the later chapters. There is much more to MD than could be explained in this chapter, such as the treatment of long-range forces in electrostatics [69, 70]. But the physics of these forces is not important for this thesis, here we refer to standard references for the interested reader

2.3.2. Diffusion-Advection Systems

MD simulations are based on knowledge about the pair interactions of atoms and use this to analyze the emergent properties of a collection of many particles. Continuum simulations, on the other hand, are defined by these emergent properties, which are classified by underlying **p**artial **d**ifferential **e**quations (PDEs) of a system. The challenge is to find the solution of these PDEs under the boundary conditions given by the real system.

The advection-diffusion system of interest for this work con-

sists of several different species in solution. A simple example is an ink droplet in water. Initially, the ink is highly localized, but then it starts to spread out by diffusion. However, the water is also in motion and carries the ink with it, which is called advection or convection. Other examples are dissolved ions in the electric field of a capacitor or the transport of nutrients through porous media.

The Diffusion-Advection Model

In this derivation of the model, only one dissolved particle species is considered, which means that the subscript identifying the species can be omitted. Later, when electrostatics and reactions are considered, they will be reintroduced. The density ρ of a species can vary locally and is propagated by fluxes $\mathbf{j}$ according to the continuity equation:

$$\frac{\partial \rho}{\partial t} = -\boldsymbol{\nabla} \cdot \mathbf{j} \quad . \tag{2.49}$$

The fluxes can be separated into a diffusion and an advection flux:

$$\mathbf{j} = \mathbf{j}^{\mathrm{diff}} + \mathbf{j}^{\mathrm{adv}} \quad . \tag{2.50}$$

According to Fick's law [71], the diffusion flux can be described by:

$$\mathbf{j}^{\mathrm{diff}} = -D\boldsymbol{\nabla}\rho \quad , \tag{2.51}$$

where D is the diffusion coefficient. Technically, D can be space-dependent, but the systems under investigation are rather dilute and have no temperature gradient, so it can be assumed to be constant.

The advection flow, on the other hand, is determined by the flow of the solvent, and the solutes move with it:

$$\mathbf{j}^{\text{adv}} = \rho \mathbf{u} \quad . \tag{2.52}$$

The velocity of the fluid $\mathbf{u}$ can be determined by the incompressible Navier-Stokes equations:

$$\tilde{\rho} \left(\frac{\partial \mathbf{u}}{\partial t} + \mathbf{u} \cdot \boldsymbol{\nabla} \mathbf{u} \right) = -\boldsymbol{\nabla} p + \eta \nabla^2 \mathbf{u} + \mathbf{f} \qquad \text{and} \tag{2.53a}$$

$$\frac{\partial \tilde{\rho}}{\partial t} + \boldsymbol{\nabla} \tilde{\rho} \mathbf{u} = 0 \quad . \tag{2.53b}$$

Here $\tilde{\rho}$ is the density of the fluid, p is the pressure, η is the viscosity and $\mathbf{f}$ is a force acting on the fluid. These Navier-Stokes equations have been shown to describe the fluid behavior with good accuracy for many length scales and even for turbulent flow.

Not only does the fluid pull around the species, but the diffusion of the species also causes a force on the fluid. So when a species is pulled through the solvent, the solvent starts to move with it. This drag force is described as:

$$\mathbf{f} = \frac{1}{\nu} \mathbf{j}^{\text{diff}} \quad , \tag{2.54}$$

with the mobility ν. Via the Einstein-Smoluchowski relation this mobility can be connected to the diffusion coefficient by

$$D = \nu k_{\text{B}} T \quad . \tag{2.55}$$

Flux Discretization

With the Equations (2.50) to (2.54) the advection-diffusion system is completely determined. While it is possible to find analytical solutions for some special cases (e.g. laminar flow and 1D symmetry), a general solution is not known. Therefore, numerics is used to solve these equations. The method chosen for this work is a finite-volume method, that is density preserving. The **L**attice-**B**oltzmann (LB) is method used to solve the Navier-Stokes equations. The method is inspired by the work of Rempfer et al. [72], which builds on a model by Capuani et al. [73].

The numerical approach relies on discretizeíng the space into a grid of small cells. The properties within these cells are treated as constant over the cell volume. The grid used here is a regular Cartesian grid with grid constant a_i, where $i \in x, y, z$ denotes the direction. Time is also discretized, which is then incremented with the time step Δt.

The density from one cell can only be transported to the neighboring cells via the fluxes. This means that the flow direction is also discretized. However, there are different ways to define what neighboring cells are, depending on whether they have a common face, edge or corner. So in 2D the flows can consider only 4 face neighbors or also the 4 corner neighbors. This is commonly called a stencil. The notation for these stencils is DXQY, where X is the dimension of the system and Y is the number of cells a cell can interact with. Since the cell can interact with itself, $Y - 1$ is the number of neighbors considered. Typical stencils are shown in Figure 2.9. The directed discretized fluxes can only act between 2 cells and shift the density between them. This means that the flux is at the
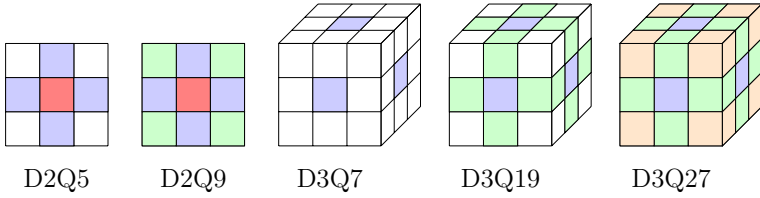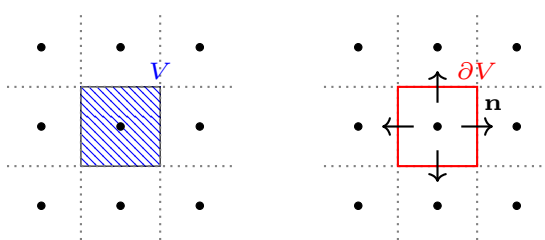
| D2Q5 | D2Q9 | D3Q7 | D3Q19 | D3Q27 |

Figure 2.9.: Illustration of the different neighboring cells considered for different stencils. Colored cells are recognized by the stencils. Red marks the origin cell (inside of the cube for 3D). Blue are the face neighbors, green the edge neighbors and orange the corner neighbors.

cell boundaries, which corresponds to an offset of half a grid spacing. This is then called a staggered grid.

The essence of the finite-volume method is that you integrate the time derivative of the density over a small volume and use Gauss' theorem to rewrite it as an integral of the fluxes through the surface. The beauty of this is that the integrals are easy to calculate, since the density in each cell and the fluxes over each surface are constant, and the integral turns into a simple sum. Evaluating these sums leads to an updating formula of the density over the flows. An illustration of this finite volume approach is shown in Figure 2.10.

With this the discretized form of the continuity equation (2.49) is:

$$\frac{\rho(\mathbf{x}, t + \Delta t) - \rho(\mathbf{x}, t)}{\Delta t} = \sum_{i \in \text{n.n.}} j_i(x + \frac{\mathbf{a}_i, t}{2})\frac{1}{a_i A_0} \quad , \quad (2.56)$$

$$\int\limits_{V} \frac{\partial \rho}{\partial t}\,\mathrm{d}V \overset{\text{Gauss's theorem}}{=} - \oint\limits_{\partial V} \mathbf{j} \cdot \mathbf{n}\,\mathrm{d}A$$

$$V\frac{\rho(t+\Delta t)-\rho(t)}{\Delta t} = -\sum_i j_i A_i$$

Figure 2.10.: Illustration of the 2D finite volume scheme. **n** is the normal vector on the surface of the cell and A_i is the surface area in the i-th direction. Figure adapted from [74]

where the summation goes over all nearest neighbors and $\mathbf{a}_i$ is the direction to these cells. A_0 represents the area of the interface between the cells. However, this becomes ambiguous if not only area neighbors but also edge or corner neighbors are considered, because then this area does not exist. Therefore, it is better to treat it simply as a renormalisation factor, so that this summation does not overestimate the acting fluxes [73]. In the appendix A it is explained how A_0 can be determined.

For the discretization of the diffusion flux (2.51), finite differences are used to calculate the gradient of the density, and since the fluxes are shifted by half a grid cell, this differential is calculated in the correct place and does not require interpolation:

$$j_i(\mathbf{x} + \frac{\mathbf{a}_i}{2}, t) = -D\frac{\rho(\mathbf{x} + \mathbf{a}_i, t) - \rho(\mathbf{x}, t)}{|a_i|} \quad . \tag{2.57}$$

The advection flow is handled somewhat differently. The velocity used for this is calculated with the LB method, which uses the same grid discretization. This means that the velocities obtained are evaluated at the correct location. The species density within a cell is shifted by this fluid velocity. The advection flux is then determined by the overlap of the displaced cell and the neighboring grid cells. This scheme is shown in Figure 2.11.

With the discretization of the diffusion and advection fluxes, the foundation of this model is ready. However, the simulation of an empty box would be uninteresting and therefore boundary conditions are needed. Apart from the periodic boundary conditions discussed in the section on MD, one typically distinguishes between two types of boundary conditions, Dirichlet and Neumann boundary conditions. Dirichlet boundary con-
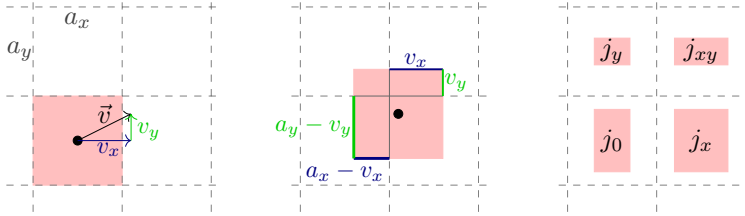
Figure 2.11.: Illustration of how the discretized advection fluxes are determined. The overlap area is calculated from the velocity and the grid spacing. j_0 describes the flux of the non-moving density, while the others are the fluxes into the respective cells.

ditions define a solution of the PDE at the location of the boundary. Neumann boundary conditions, on the other hand, enforce the value of the derivative of the property. To apply these boundary conditions, a cell is marked as a boundary and the properties are set accordingly. With this, the system can now be specified. If one wants a diffusion channel with an inlet and an outlet, then the channel walls can be realized by setting the fluxes into the boundary to zero. The inlets and outlets are constant then density boundary conditions and the velocity can also be set there.

Electrostatics

Until now the dissolved species handled with this model had no net charge. However, for many applications, like salt solutions, these species are charged and interact which each other electrostatically. This means that a species feels a force according

to an electric field, but also that a density gradient of a charged species creates an electric field in the first place. If there are oppositely charged species present, they will also cause electrostatic screening effects, according to the Debye-Hückel theory [75]. Because the species are are no longer independent from each other, we introduce the index k to denote them. The electrostatic forces lead to a drift velocity $\mathbf{v}_k$ of the species:

$$\mathbf{v}_k^{\text{drift}} = \nu_k \mathbf{F}_k = \nu_k q_k \boldsymbol{\nabla}\Phi \quad , \tag{2.58}$$

where q_k is the charge of the species k and Φ the electrostatic potential given by the Poisson equation:

$$\nabla^2\Phi = \frac{1}{\epsilon}\sum_{k \in \text{species}} q_k \rho_k = \frac{\rho^{\text{charge}}}{\epsilon} \quad , \tag{2.59}$$

where ρ^{charge} is defined as the charge density over all species. To decouple macroscopic and microscopic properties, the susceptibility ϵ is often written in terms of the Bjerrum length l_{B}

$$\epsilon = \frac{e^2}{4\pi l_{\text{B}} k_{\text{B}} T} \quad . \tag{2.60}$$

With the drift velocity the resulting flux concludes to be :

$$\mathbf{j}_k^{\text{diff}} = -D_k \boldsymbol{\nabla}\rho_k - \nu_k q_k \rho_k \boldsymbol{\nabla}\Phi \quad . \tag{2.61}$$

The discretization of the updated diffusion flux is analogous to the previous discretization:

$$\begin{aligned} j_{k,i}(\mathbf{x} + \frac{\mathbf{a}_i}{2}, t) = {}& - D_k \frac{\rho_k(\mathbf{x} + \mathbf{a}_i, t) - \rho_k(\mathbf{x}, t)}{|a_i|} \\ & - \nu_k q_k \rho_k(\mathbf{x} + \frac{\mathbf{a}_i}{2}, t) \frac{\Phi(\mathbf{x} + \mathbf{a}_i, t) - \Phi(\mathbf{x}, t)}{|a_i|} \quad , \end{aligned} \tag{2.62}$$

where the density value in between the cells is just the arithmetic mean of both cells:

$$\rho_k\left(\mathbf{x} + \frac{\mathbf{a}_i}{2}, t\right) = \frac{\rho_k(\mathbf{x}, t) + \rho_k(\mathbf{x} + \mathbf{a}_i, t)}{2} \quad . \tag{2.63}$$

Since the Poisson equation has no time dependence, it can be discretized into a series of linear equations by applying finite differences to the Laplace operator. For simplicity, only the 1D case is considered, and because of linear independence, the other directions are analogous.

$$\rho^{\text{charge}}(x, t) = \epsilon \frac{\Phi(x - a_x, t) - 2\Phi(x, t) + \Phi(x + a_x, t)}{a_x^2} \tag{2.64}$$

This results in a set of N_x linear equations, where N_x is the number of cells in that direction. Many different methods can be used to solve this trigonal system, such as Gauss elimination or successive over-relaxation. However, since the system is periodically repeated, the discrete Poisson equation can be easily transformed into Fourier space, resulting in:

$$\hat{\rho}^{\text{charge}}(k, t) = \epsilon \frac{e^{\frac{-2\pi i k}{N_x}} \hat{\Phi}(k, t) - 2\hat{\Phi}(k, t) + e^{\frac{2\pi i k}{N_x}} \hat{\Phi}(k, t)}{a_x^2}$$

$$= 2\epsilon \frac{\cos\left(\frac{2\pi k}{N_x}\right) - 1}{a_x^2} \hat{\Phi}(k, t)$$

$$= G(k)\hat{\Phi}(k, t) \quad . \tag{2.65}$$

This determines the Greens-function $G(k)$, which relates the Fourier transformed charge density and the transformed po-

tential. In 3D this Greens-function turns out to be:

$$G(\mathbf{k}) = 2\epsilon \sum_{j\in x,y,z} \frac{\cos\left(\frac{2\pi k_j}{N_j}\right) - 1}{a_j^2} \quad . \qquad (2.66)$$

After calculating the $\hat{\Phi}$ from $\hat{\rho}^{\text{charge}}$, an inverse Fourier transform is applied to obtain the charge potential. This completes the electrostatic part of the model, which can now be used for salt solutions and, with the application of a boundary condition to the charge potential, also for electrolyte flow within capacitors. This also gives the method the name **e**lectro**k**inetic model EK. Suitable applications for this model can be found in research areas ranging from the transport of electrolytes through porous media via biomolecules and colloids in ion-containing solutions [76, 77, 78] to the study of microfluidic mechanisms such as pumps [79] or selective particle traps [72, 80]. An extension of the electrokinetic model to moving colloids in binary fluid flows has also recently been achieved [81].

Reactions

Another way in which different diffusive species can interact is through reactions [82]. In this case, the species are converted into each other depending on their local densities. The reaction rate $R_{\tilde{k}}$ of the reaction $\tilde{k}$ in which this conversion occurs is determined by the rate equation:

$$R_{\tilde{k}} = \Gamma_{\tilde{k}} \prod_{i\in\text{reactants}} \rho_i^{\alpha_{\tilde{k},i}} \quad , \qquad (2.67)$$

with $\Gamma_{\tilde{k}}$ as reaction rate constant and $\alpha_{\tilde{k},i}$ as the reaction order of the different species i taking part in the reaction. The change

in density due to the reaction is then given by:

$$\frac{\partial \rho_k}{\partial t} = s_{\tilde{k},k} R_{\tilde{k}} \quad , \qquad (2.68)$$

where $s_{\tilde{k},k}$ are the stoichiometric coefficients of species k in the reaction $\tilde{k}$. Here we use the notation that the stoichiometric coefficients of the reactants are negative, while the products are signed positive.

The discretization of the reactions is rather simple. The local reaction rate can be calculated directly from the discretized densities. Finite-differences are used for the density propagation:

$$\rho_k(\mathbf{x}, t + \Delta t) = \rho_k(\mathbf{x}, t + \Delta t) + \Delta t s_{\tilde{k},k} R_{\tilde{k}}(\mathbf{x}, t) \quad . \qquad (2.69)$$

There are two ways to represent these reactions. The first way is to apply them as bulk reactions, so that the reaction takes place everywhere in the system. A simple example of this would be the autodissociation of water. The other way is to represent them locally, for example at the boundaries where they model, i.e. a catalytic reaction. In this way, one can study substrate transport towards and away from a catalyst. The use of bulk and surface reactions allows the study of the self-chemistry of active colloids [83, 84], where H_2O_2 on a Pt-coated side of the colloids is catalyzed

$$H_2O_2 \xrightarrow{\text{Pt}} O_2 + 2\,H^+ + 2\,e^-. \qquad (2.70)$$
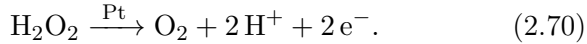
While the elections remain in the colloid, the hydrogen atoms go in solution and diffuse around the colloid. On the other Au-coated side of the colloid, these ions are reduced to water

and hydrogen with the electrons inside the colloids

$$H_2O_2 + O_2 + 6\,H^+ + 6\,e^- \xrightarrow{\text{Au}} 4\,H_2O. \qquad (2.71)$$
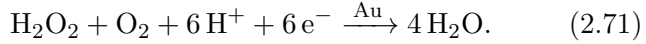
Since the ion cloud around the colloid is asymmetric, the charges inside the colloid exert a force on the ions that moves the colloid. However, during this process, mass reactions also play an important role, as the autodissociation of H_2O_2 into ions enhances the ion gradients [85]

$$H_2O_2 \rightleftharpoons HO_2^- + H^+. \qquad (2.72)$$
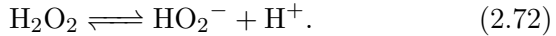
An other possible application for this model is to analyze diffusion or flow-driven reactions [86].

2.4. Summary

In this chapter, the basics of catalysis, polymer physics and numerical simulation methods were discussed to provide the background for a better understanding the following chapters. In Chapter 3, the diffusion-advection reaction system is extended to include thermal fluctuations so that systems where these cannot be neglected can be simulated with better accuracy. Subsequently, in Chapter 4, polymer theory is used to gain insight into the influence of walls on the ring closure probability of the metathesis reaction. In Chapter 5, coarse-grained MD simulations in a grand canonical ensemble are used to further investigate the mechanism of ring-closing metathesis in mesopores in different geometries.

3. Fluctuating Advection-Diffusion-Reaction Method

This chapter is based on the following publication. My contribution waere implementation of the fluctuating reactions, benchmarking and validation.

The **c**ollaborative **r**esearch **c**enter (CRC) 1333's simulation projects span several length and time scales. While there are projects that analyze the subject on quantum and all-atom scales, in this project it has been studied on continuum and coarse-grained scales. We began at the large scales utilizing continuum simulations. In this approach, we neglect the individual reaction molecules within the pore and consider them as densities of different species. These densities obey the advection-diffusion-reaction equations solved on a discretized grid.

The pore systems under investigation have a diameter of $d \in [5, 50]$ nm, so the resolution of the grid had to be chosen accordingly. For the given substrate concentration, it turns

out that the number of molecules per cell that make up the density is rather small ($N < 100$). With such a low number of particles, thermal fluctuations of the density become significant. Since the model is based on the assumption that the molecules behave like an ideal gas, the density fluctuation also scales with the square root of the number of particles per cell $\sqrt{N}$. This means that for low number of particles, the relative fluctuations become larger.

For many applications, these density fluctuations are irrelevant because the dependence on density is linear. In those cases the density deviations from the average density cancel out. However, on small scales many counterexamples can be found including fluctuation-induced instabilities [87], pattern formation [88, 89], stochastic processes in cell biology [90] and transport properties [91, 92]. In our case the density scaling of reactions is determined by the rate equation (2.67), which can be linear or non-linear depending on the reaction order. In the simulation, the amount of product produced over time can therefore be different, regardless of whether fluctuations are taken into account or not.

A small example of this is the reaction $2A \rightarrow B$. Any particle of type A can react with any other particle of the same type. This means that for a box with N particles in it, there are $N(N-1)$ possibilities for a reaction to take place. Even though not all reactions can take place, this determines how likely the reaction is. Therefore, the order for this reaction is two. Now, if the number of particles changes due to thermal fluctuations, the number of reactions that take place also changes. Because of the non-linearity, the increase in the number of particles has a greater effect on the number of reactions

than the decrease in the number of particles. This means that the number of reactions is higher on average when fluctuations are present, which is why the thermalization of the fluxes cannot be neglected for the systems of interest. Since the importance of fluctuations on the scales of the pores is known, the first task of the project was to implement and test these fluctuations. This includes the thermalization of the diffusion, advection and reaction part, which all need to be thermalized, so that none of these methods acts as an energy sink to the other ones. The thermalization of the **L**attice-**B**oltzmann (LB) method has long been solved and implemented [93, 94].

3.1. Thermalization of the Advection-Diffusion Method

The addition of thermal fluctuations to the diffusion advection model is not a completely novel idea and has been done before [95, 96, 97, 98], however in those cases the incompressible Navier-Stokes equation was solved via a finite volume scheme, while we solve the compressible one with LB instead.

The derivation of the fluctuation term follows ref. [99]. We begin with the over-damped Langevin equation for N particles of the same species:

$$\frac{\partial \mathbf{r}_i(t)}{\partial t} = \boldsymbol{\eta}_i(t) - \boldsymbol{\nabla}\psi(\mathbf{r}_i, t) \quad , \tag{3.1}$$

where i indicated the different particles, $\Psi(\mathbf{r}_i, t)$ is a potential field acting on the particles and $\eta_i(t)$ is an uncorrelated random

3. Fluctuating Advection-Diffusion-Reaction Method

noise term, defined by:

$$\langle \boldsymbol{\eta}_i(t) \rangle = \mathbf{0} \tag{3.2a}$$

$$\langle \eta_i^\mu(t)\eta_j^\nu(t') \rangle = 2D\delta_{ij}\delta_{\mu\nu}\delta(t-t') \quad , \tag{3.2b}$$

where μ and ν index the different components of the vector.

The particle positions can also be described by a particle density function via delta functions, where $\rho_i(\mathbf{r}, t) = \delta(\mathbf{r}_i(t) - \mathbf{r})$ defines the density of single particle. The density functions of all particles then returns:

$$\rho(\mathbf{r}, t) = \sum_{i=1}^{N} \rho_i(\mathbf{r}, t) = \sum_{i=1}^{N} \delta(\mathbf{r}_i(t) - \mathbf{r}) \quad . \tag{3.3}$$

Let f be an arbitrary function, for which we can calculate its value at any position $\mathbf{r}_i$ via the integral over the single particle density:

$$f(\mathbf{r}_i(t)) = \int_{\mathbb{R}^3} d^3\mathbf{r} f(\mathbf{r})\rho_i(\mathbf{r}, t) \quad . \tag{3.4}$$

We will use this function f to compare its classical and stochastic derivative, which will give us insights into the stochastic process influencing the density. The classical derivative is straightforward:

$$\frac{df(\mathbf{r}_i(t))}{dt} = \int_{\mathbb{R}^3} d^3\mathbf{r} f(\mathbf{r})\frac{\partial \rho_i(\mathbf{r}, t)}{\partial t} \quad . \tag{3.5}$$

For the stochastic one the use of Itô calculus [100] is required, which describes how integrals of stochastic processes can be determined. The differential of a stochastic process dX_t can be described by the addition of a deterministic part with the

drift velocity μ_t and a Brownian process B_t with a variance of σ_t:

$$\mathrm{d}X_t = \mu_t\mathrm{d}t + \sigma_t\mathrm{d}B_t \quad . \tag{3.6}$$

When a function undergoes this stochastic process we can use Taylor-extension to obtain its time evolution:

$$\begin{aligned}
\mathrm{d}f =& \frac{\partial f}{\partial t}\mathrm{d}t + \frac{\partial f}{\partial x}\mathrm{d}x + \frac{1}{2}\frac{\partial^2 f}{\partial x^2}\mathrm{d}x^2 + \dots \\
=& \frac{\partial f}{\partial t}\mathrm{d}t + \frac{\partial f}{\partial x}(\mu_t\mathrm{d}t + \sigma_t\mathrm{d}B_t) \\
& + \frac{1}{2}\frac{\partial^2 f}{\partial x^2}\mathrm{d}x^2(\mu_t^2\mathrm{d}t^2 + 2\mu_t\sigma_t\mathrm{d}t\mathrm{d}B_t + \sigma_t^2\mathrm{d}B_t^2) \quad .
\end{aligned} \tag{3.7}$$

We are only interested in parts which are of first order in $\mathrm{d}t$. However, it turns out that the Brownian process $\mathrm{d}B_t$ scales with the square root of $\mathrm{d}t = \mathrm{d}B_t^2$. Therefore this term also needs to be considered:

$$\mathrm{d}f = \left(\frac{\partial f}{\partial t} + \mu_t\frac{\partial f}{\partial x} + \frac{\sigma_t^2}{2}\frac{\partial^2 f}{\partial x^2}\right)\mathrm{d}t + \sigma_t\frac{\partial f}{\partial x}\mathrm{d}B_t \quad . \tag{3.8}$$

Because the Brownian process for this case is resulting from the over-damped Langevin equation (3.1), the drift velocity, variance and time derivative are given as:

$$\boldsymbol{\mu}_t = -\boldsymbol{\nabla}\psi(\mathbf{r}_i, t) \quad , \tag{3.9a}$$

$$\sigma_t = \sqrt{2D} \quad \text{and} \tag{3.9b}$$

$$\frac{\mathrm{d}\mathbf{B}_t}{\mathrm{d}t} = \frac{\boldsymbol{\eta}_i(t)}{\sqrt{2D}} \quad . \tag{3.9c}$$

Using this the time derivative of f results to be:

3. Fluctuating Advection-Diffusion-Reaction Method

$$\frac{\mathrm{d}f(\mathbf{r}_i)}{\mathrm{d}t} = \overbrace{\frac{\partial f(\mathbf{r}_i)}{\partial t}}^{=0} + \boldsymbol{\nabla}_i f(\mathbf{r}_i)\left(\boldsymbol{\mu}_t + \sigma_t\frac{\mathrm{d}\mathbf{B}_t}{\mathrm{d}t}\right) + \frac{\sigma^2}{2}\boldsymbol{\nabla}_i^2 f(\mathbf{r}_i)$$

$$= \int_{\mathbb{R}^3} \mathrm{d}^3\mathbf{r} f(\mathbf{r})\Big[\boldsymbol{\nabla}_i\cdot\big(-\rho_i(\mathbf{r},t)\boldsymbol{\nabla}_i\psi(\mathbf{r},t) + \rho_i(\mathbf{r},t)\boldsymbol{\eta}_i(t)\big)$$

$$+ D\boldsymbol{\nabla}_i^2\rho_i(\mathbf{r},t)\Big] \quad . \tag{3.10}$$

With the classical (3.5) and the stochastic time derivative (3.10) now determined, the difference of these two then results to be:

$$\frac{\partial\rho_i(\mathbf{r}_i,t)}{\partial t} = \boldsymbol{\nabla}_i\cdot\big(-\rho_i(\mathbf{r},t)\boldsymbol{\nabla}_i\psi(\mathbf{r},t) + \rho_i(\mathbf{r},t)\boldsymbol{\eta}_i(t)\big)$$

$$+ D\boldsymbol{\nabla}_i^2\rho_i(\mathbf{r},t) \quad . \tag{3.11}$$

Summing up over all particles i returns:

$$\frac{\partial\rho(\mathbf{r},t)}{\partial t} = \boldsymbol{\nabla}\cdot(-\rho(\mathbf{r},t)\boldsymbol{\nabla}\psi(\mathbf{r},t)) + \xi(\mathbf{r},t)$$

$$+ D\boldsymbol{\nabla}^2\rho(\mathbf{r},t) \quad , \tag{3.12}$$

where the noise field $\xi(\mathbf{r},t)$ is defined as:

$$\xi(\mathbf{r},t) = \sum_{i=1}^{N}\boldsymbol{\nabla}\cdot(\rho_i(\mathbf{r},t)\boldsymbol{\eta}_i(t)) \quad . \tag{3.13}$$

This amplitude of noise is now dependent on the density and has the correlation:

$$\langle \xi(\mathbf{r}, t)\xi(\mathbf{r}', t')\rangle = 2D\delta(t - t')$$
$$\cdot \boldsymbol{\nabla}_r \cdot \boldsymbol{\nabla}_{r'} \left(\delta(\mathbf{r} - \mathbf{r}')\rho(\mathbf{r}, t) \right) \quad . \tag{3.14}$$

Since the sum in the definition of the noise field is hard to come by, it is preferred to search for a different noise field, which has the same statistical properties. It turns out that a noise field which is statistically identical is:

$$\xi'(\mathbf{r}, t) = \boldsymbol{\nabla} \cdot \left(\boldsymbol{\eta}(\mathbf{r}, t)\sqrt{\rho(\mathbf{r}, t)} \right) \quad , \tag{3.15}$$

where the global noise field $\boldsymbol{\eta}$ is defined by:

$$\langle \boldsymbol{\eta}(\mathbf{r}, t)\rangle = \mathbf{0} \qquad \text{and} \tag{3.16a}$$
$$\langle \eta^{\mu}(\mathbf{r}, t)\eta^{\nu}(\mathbf{r}', t')\rangle = 2D\delta_{\mu\nu}\delta(t - t')\delta(\mathbf{r} - \mathbf{r}') \quad . \tag{3.16b}$$

Substituting ξ with ξ' in Equation (3.12) and also reintroducing the advective flux, results in:

$$\frac{\partial\rho(\mathbf{r}, t)}{\partial t} = \boldsymbol{\nabla} \cdot \mathbf{j} \qquad \text{and} \tag{3.17a}$$
$$\mathbf{j} = \underbrace{\rho(\mathbf{r}, t)\boldsymbol{\nabla}\psi(\mathbf{r}, t)}_{\mathbf{j}^{\text{pot}}} + \underbrace{D\boldsymbol{\nabla}\rho(\mathbf{r}, t)}_{\mathbf{j}^{\text{diff}}}$$
$$+ \underbrace{\sqrt{\rho(\mathbf{r}, t)}\boldsymbol{\eta}(\mathbf{r}, t)}_{\mathbf{j}^{\text{fluct}}} + \underbrace{\rho(\mathbf{r}, t)\mathbf{u}(\mathbf{r}, t)}_{\mathbf{j}^{\text{adv}}} \quad . \tag{3.17b}$$

With this we obtained a more general version of the Poisson equation (2.59), which now describes the density behavior under the consideration of fluctuations.

3. Fluctuating Advection-Diffusion-Reaction Method

With this done, the discretization of the fluctuation flux also needs to be taken care of. Because the fluxes only exist on the staggered grid the density and the fluxes needs to be determined in between the grid cells:

$$
j_i^{\text{fluct}}(\mathbf{x} + \frac{\mathbf{a}_i}{2}, t) = \sqrt{\rho(\mathbf{x} + \frac{\mathbf{a}_i}{2}, t)} \eta(\mathbf{x} + \frac{\mathbf{a}_i}{2})
$$

$$
\approx \sqrt{\frac{\rho(\mathbf{x}, t) + \rho(\mathbf{x} + \mathbf{a}, t)}{2}} \eta(\mathbf{x} + \frac{\mathbf{a}_i}{2}) \quad , \quad (3.18)
$$

where a Gaussian white noise field $\mathcal{W}$ is used to define the noise η:

$$
\eta(\mathbf{x}, t) = \sqrt{2D} \mathcal{W}(t) \quad . \tag{3.19}
$$

The important thing here is, that the time integral, which is used to approximate properties in the next time step, doesn't scale linearly with the time step, but rather with its square root:

$$
\int_t^{t+\Delta t} dt' \mathcal{W}(t') = \sqrt{\Delta t} \mathcal{W}(t) \quad . \tag{3.20}
$$

Using this for the update rule results in:

$$
\rho(\mathbf{x}, t + \Delta t)) = \rho(\mathbf{x}, t) + \Delta t \sum_{i \in \text{n.n.}} \frac{1}{a_i A_0}
$$

$$
\cdot \left[j_i^{\text{diff}}(\mathbf{x} + \frac{\mathbf{a}_i}{2}, t) + j_i^{\text{pot}}(\mathbf{x} + \frac{\mathbf{a}_i}{2}, t) \right.
$$

$$
+ j_i^{\text{adv}}(\mathbf{x} + \frac{\mathbf{a}_i}{2}, t)
$$

$$
\left. + \frac{1}{\sqrt{\Delta t}} j_i^{\text{fluct}}(\mathbf{x} + \frac{\mathbf{a}_i}{2}, t) \right] \quad . \tag{3.21}
$$

This concludes the derivation of the thermalized density flux fluctuation and how they are handled numerically. However, the process of reactions, which also is highly fluctuating by nature, still needs to be taken care of. The method for this originated from Gillespie [101]. A chemical reaction during one time step can be viewed as a Poisson process, as long as the single reaction events are independent from each other. This enforces the condition that the change in substrate density throughout a single time step $[t, t + \Delta t]$ is small enough to neglect any influence the reaction probability. One way to ensure this is to choose a sufficiently small time step. With the Poisson random variable $\mathcal{P}(R_{\tilde{k}}(\mathbf{r}, t), \Delta t)$ it is defined how many reaction processes occur within the time step Δt. The reaction rate $R_{\tilde{k}}$ for the reaction $\tilde{k}$ was defined in rate equation (2.67):

$$R_{\tilde{k}} = \Gamma_{\tilde{k}} \prod_{i \in \text{reactants}} \rho_i^{\alpha_{\tilde{k}, i}} \quad . \tag{2.67}$$

Knowing the number of reactions per time step, the update rule on the density is then changed to:

$$\rho_k(\mathbf{x}, t + \Delta t) = \rho_k(\mathbf{x}, t) + s_{\tilde{k}, k} \mathcal{P}(R_{\tilde{k}}(\mathbf{r}, t), \Delta t) \quad . \tag{3.22}$$

The Poisson distribution is used as a distribution of discrete events, however, for this application a description with floating point values is needed. So to get there we transform the Poisson distribution $\mathcal{P}$ into an normal distribution $\mathcal{N}$, which is a good approximation when many reaction events happen within the same time step $\mathcal{P}(R_{\tilde{k}}(\mathbf{r}, t), \Delta t) >> 1$. The resulting normal distribution $\mathcal{N}(m, \sigma^2)$ is defined by the mean $\mu = R_{\tilde{k}}(\mathbf{r}, t)$ and the variance $\sigma^2 = R_{\tilde{k}}(\mathbf{r}, t)$. This Gaussian distribution can

furthermore be simplified by stretching and shifting into one where the mean is $\mu = 0$ and the variance $\sigma^2 = 1$, which then results into the update rule of:

$$
\begin{aligned}
\rho_k(\mathbf{x}, t + \Delta t) =& \rho_k(\mathbf{x}, t) + s_{\tilde{k},k} R_{\tilde{k}}(\mathbf{r}, t)\Delta t \\
&+ s_{\tilde{k},k}\sqrt{R_{\tilde{k}}(\mathbf{r}, t)\Delta t}\mathcal{N}(0, 1) \quad .
\end{aligned} \tag{3.23}
$$

This change from Poisson to Gaussian distribution only works when the time step is chosen to be large enough for many reactions to occur. This means that for this model to work physically correct, two conditions on the time step have to be meet, one for the small density changes within one time step and the other for the transition to the normal distribution.

3.2. Implementation and Benchmarking

In practice, the model is implemented by coupling three solvers: a finite-volume solver for the diffusion-advection equation [73, 102], a Fourier-based solver for obtaining the electrostatic potential from the charge distribution via the Poisson equation [102], and a LB hydrodynamic implementation [103]. The employed LB utilizes a D3Q19 stencil and a two-relaxation-time collision operator [104]. The thermalization of the LB fluid was handled by adding fluctuations to the stress modes as introduced by Dünweg et al. [93]. The simulation package ESPResSo [105, 20] contains all necessary components. As they are largely based on regular grids and matrix-vector operations, all algorithms are well suited for deployment on graphics processing units (GPUs). ESPResSo hence implements such accelerated versions [106, 102].

For the implementation of the fluctuations and reactions we will be using pystencils[21], because for future releases of ESPResSo (4.3 and onward) the manually written grid based solver kernels will be replaced by ones generated using sympy, pystencils and lbmpy[107]. sympy is a python module which interprets mathematical equations. pystencils can then discretize partial differential equations given to it onto a Cartesian grid. With all the update rules defined, it compiles them into a c++ kernel, which can be executed. The last module, lbmpy, uses pystencils to generate kernels and solve the Navier-Stokes equations by the LB method. During this code generation process one can specify the target platform, i.e. whether the code shall be executed on the CPU, GPU or via OpenMP. It is also possible to change the floating point precision, which one can use to optimize the balance between performance and numerical accuracy. The Fourier-based Poisson solver is not generated and is manually implemented into ESPResSo. The pure pystencils implementation was used to test and validate the method.

The full algorithm, including **e**lectro**k**inetics (EK), reactions and LB involves the following steps:

1. Calculate total charge from per-species densities and valencies

2. Obtain the electrostatic potential for the charge distribution by solving the Poisson equation via the Fourier solver

3. Calculate the fluxes, including thermal fluctuations, using Eq. (3.17b)

4. Based on the fluxes, add external forces to the coupled LB fluid (Eq. (2.54))

5. Add sources and sinks to the fluxes based on chemical reactions (Eq. (3.23))

6. Apply any boundary conditions to the densities and fluxes

7. Solve the continuity equation (Eq. (2.49))

8. Propagate the LB fluid by one step

9. Advect the densities according to the LB fluid's velocities. This is done using a volume-of-fluid approach, more formally known as *corner-transport upwind scheme* [73, 108].

While the underlying equations are straightforward, there are some details that need to be discussed. For the derivation of the advection-diffusion method, it is assumed that the particle density per cell is large enough to be considered as a continuum. However, for some examples, like the ion distributions in mesoporous media, one would need a very fine grid resolution to resolve the Debye layer and to reproduce the geometry. This in turn would result in a small average density per grid cell ($\approx 10 - 20/a^3$), and it is possible that locally some cells may reach a density below $\rho(\mathbf{r}_i) < 1/a^3$. If one would then calculate the amplitude of the fluctuations as stated in Equation (3.18), the resulting fluctuation could be larger than the density in the cell, which would mathematically lead to a negative density. This is unphysical and also leads to a numerical breakdown in the next time step. To circumvent this issue, we scale down the amplitude of the fluctuations smoothly to

be less than the local density. For that we define a smoothed Heaviside function:

$$H(n) = \begin{cases} 0 & n < 0 \\ n & 0 < n < 1 \\ 1 & 1 < n \end{cases} , \tag{3.24}$$

which we use to rescale the average density of Equation (3.18):

$$\mathbf{j}_i^{\text{fluc}}\left(\mathbf{x} + \frac{\mathbf{a}_i}{2}, t\right) = H(\rho(\mathbf{x} + \mathbf{a}_i, t)) H(\rho(\mathbf{x}, t)) \eta\left(\mathbf{x} + \frac{\mathbf{a}_i}{2}, t\right)$$

$$\cdot \sqrt{\frac{\rho(\mathbf{x} + \mathbf{a}_i, t) + \rho(\mathbf{x}, t)}{2}} . \tag{3.25}$$

The same is applied to the fluctuating reactions (3.23).

To generate the random noise, we choose the Philox pseudo-random number generator, which has good performance on both CPU and GPU [109]. The Philox generator is counter-based, hence it does not have an internal state. Instead, pseudo-random numbers are generated from a few deterministic numbers such as the time step counter and the coordinates of the lattice cell for which a flux is to be calculated. It is of importance that the random numbers used in a cell at a domain border and in the corresponding ghost layer are the same, otherwise the fluxes would not be equal, and the density would not be conserved. Here, key-based generators are particularly useful in parallel programming, as the same random numbers can be generated at both sides of the periodic boundary without the need for communication.

To benchmark the implementation, we measured the computation time per time step for the D3Q19 and D3Q27 stencil with single (4-byte) and double (8-byte) precision on a GPU.

3. Fluctuating Advection-Diffusion-Reaction Method

This benchmark can be seen in fig. 3.1, which also shows the linear scaling with the number of cells for this method. For this, we chose a system with only one species and no charges. The test system is run on a NVIDIA Tesla V100. The times are measured from the pystencils implementation and include the time the Python script needs to start the kernels each time step, and due the slow start-up of the kernels this computation time is roughly equal for small systems. Excluding the kernel initiation time, one can confirm that this method scales linearly with system size. The different stencils also show that larger data processing results in slower simulation speeds. On the other hand it is also evident that utilizing single-precision floating point arithmetic speeds up the simulation by a factor of 1.21, however we generally do not recommend running EK in single precision. The D3Q19 kernel is also faster then the D3Q27 by a factor of 1.57.

Let us now look at the memory bandwidth usage of the kernels: there are three kernels that need to be run every time step and for each of them the data of the cells needs to be transported from the memory to the processing unit and back. The three kernels do calculations of the fluxes, updating the density based on the fluxes due to the continuity equation, and synchronizing the density over the periodic boundary, respectively. Summing up the data that needs to be transported for each cell, we get 15 floating point numbers for the flux calculation kernel (1 for the density, 3 for the velocity, one for the potential and 10 for the D3Q19 staggered fluxes), 11 for the continuity kernel (1 for the density and 10 for the fluxes) and 1 for the synchronizing kernel. So for every cell on every time step, we need a throughput of 54 floating point numbers. For
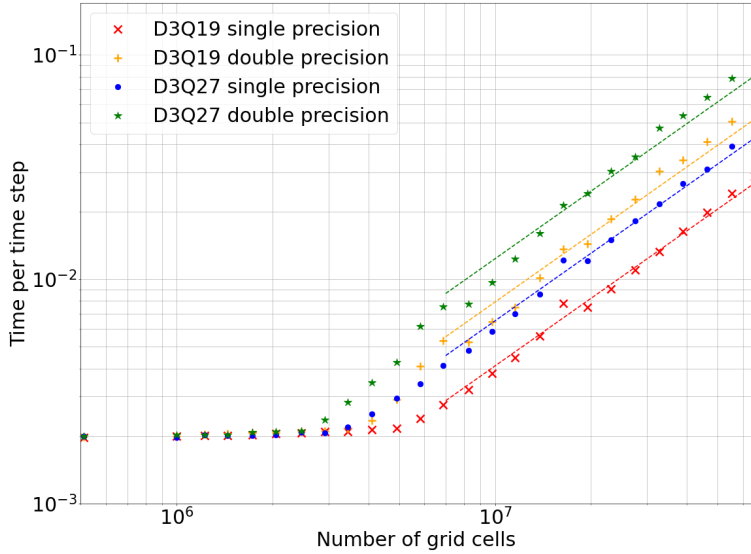
Figure 3.1.: Computation time per time step on GPU for different stencils and different floating point precisions. The fits demonstrates that for large enough system the method scales linearly with the number of grid points.

a system of 320^3 cells running in double precision, this corresponds to 14.2 GB of data that need to be transported each time step. The NVIDIA Tesla V100 GPU used for this benchmark provides a memory bandwidth of 900 GB/s. This should give us around 64 time steps per second. This is a very optimistic estimate because not all data needed for the calculations are on the local cell, but also on its neighboring cells. If this data is not present in the cache at that point, it needs to be transferred again. For simplicity, let us assume that every time data from a neighboring cell is being accessed, this data also needs to be transported to the processor. For the flux calculation we need the information of the density of the adjacent cells, which adds nine floating point numbers to the data throughput per cell. For the continuity equation we also need the nine fluxes that are not stored in the local cell. So all in all with both transport directions we need a throughput of 90 floating point numbers per cell per time step. With this assumption, we arrive at a maximum of 38 time steps per second. Our measured rate for this test system is 33.0 Hz, which is 87 % of the theoretical limit.

The implementation in pystencils is very instructive and easy to use, as it is closer to the mathematical description of the algorithm than a hand-written implementation. Moreover, it will form the basis of diffusion-advection-reaction simulations in the upcoming versions of ESPResSo. The integration with a **m**olecular **d**ynamics (MD) package makes it possible to combine EK simulations with, e.g., colloids and polymers represented as particles. There are mainly three options to choose from. The first one is the direct coupling of point particles via interpolation of the forces it receives from the fluid and the species

and vice versa. While this method is convenient and efficient, the accuracy and the discretization artifacts strongly depend on the interpolation scheme and the grid spacing used. The second way is to use raspberry particles [110], which are basically a collection of point particles to represent a single larger particle. Using the interpolation scheme with these raspberries, the accuracy increases due to the better description of the volume of the particle, however, this comes with an increase in computational cost. The final method used in ESPResSo is to represent the particles as a moving boundary condition. While the principle behind this were developed by Ladd [111] for a LB fluid, it was further enhanced by Kuron et al. [78] to be applied to the EK method. This approach comes at even more computational cost, but the reward is an accurate description of the near and the far field of the fluid around the particles. This has been shown to be suitable for investigating (self-)electrophoresis problems [83]. In future works we plan to use these methods for coupling particles to our thermalized EK model.

3.3. Validation

In this section, we demonstrate the correctness of our implementations using several scenarios for which the results are either known analytically or where they can be obtained using alternative methods.

3.3.1. Density Distribution inside of a Reaction Slit Pore System

Fig. 3.2 shows the concentration profile of two species in a slit pore system. On one wall, the conversion of species A to species B is being catalyzed, while the reverse happens on the other side. Such a system can then be described as

$$R_A(x) = \delta \left(x + \frac{d}{2} \right) k_B \rho_B(x)$$

$$- \delta \left(x - \frac{d}{2} \right) k_A \rho_A(x) \quad , \tag{3.26a}$$

$$R_B(x) = -R_A(x) \quad , \tag{3.26b}$$

$$\frac{\partial \rho_A(x,t)}{\partial t} = D_A \frac{\partial^2 \rho_A(x,t)}{\partial x^2} + R_A(x) \quad , \tag{3.26c}$$

$$\frac{\partial \rho_B(x,t)}{\partial t} = D_B \frac{\partial^2 \rho_B(x,t)}{\partial x^2} + R_B(x) \quad , \tag{3.26d}$$

where $R_i(x)$ is the local reaction rate of species i, and k_A and k_B are the reaction rate constants at the different sides of the slit pore. Because we are investigating this system in equilibrium, we can set the time derivatives to zero, which results in

$$D_A \frac{\partial^2 \rho_A(x)}{\partial x^2} = -R_A(x) \qquad \text{and} \tag{3.27a}$$

$$D_B \frac{\partial^2 \rho_B(x)}{\partial x^2} = -R_B(x). \tag{3.27b}$$

Solving this source-drain-diffusion system yields a linear density profile for the steady-state solution:

$$\rho_A(x) = -\frac{2 \cdot \rho_0 \left(x - \frac{d}{2} + \frac{D_A}{k_A} \right)}{D_A \cdot \left(\frac{1}{k_A} + \frac{1}{k_B} + \frac{d}{2} \left(\frac{1}{D_A} + \frac{1}{D_B} \right) \right)} \quad , \tag{3.28}$$

where ρ_0 is the initial density, d the width of the slit pore, D_i the diffusion constant of species i, and k_A and k_B are the reaction rates of the reaction A $\rightarrow$ B and B $\rightarrow$ A, respectively.

The simulated system shows that the fluctuations have a significant impact on the density profile, but averaging the density profile over 10000 uncorrelated time steps yields excellent agreement with the predicted density profile.

3.3.2. Ideal Gas and Coulomb Gas Density Distribution

Let us now turn to situations where thermal fluctuations are of importance. To determine whether the fluctuation model results in the correct physical behavior, we calculate the density distribution of an ideal gas. To this end we take a system of N non-interacting particles contained in a volume V. The probability that a sub-volume $v \subset V$ encloses n particles is given by

$$P(n) = \binom{N}{n} \left(\frac{v}{V} \right)^n \left(\frac{V - v}{V} \right)^{N-n} \quad . \tag{3.29}$$

In the limit of $N \rightarrow \infty$ and $v \ll V$ this equation turns into the Poisson distribution

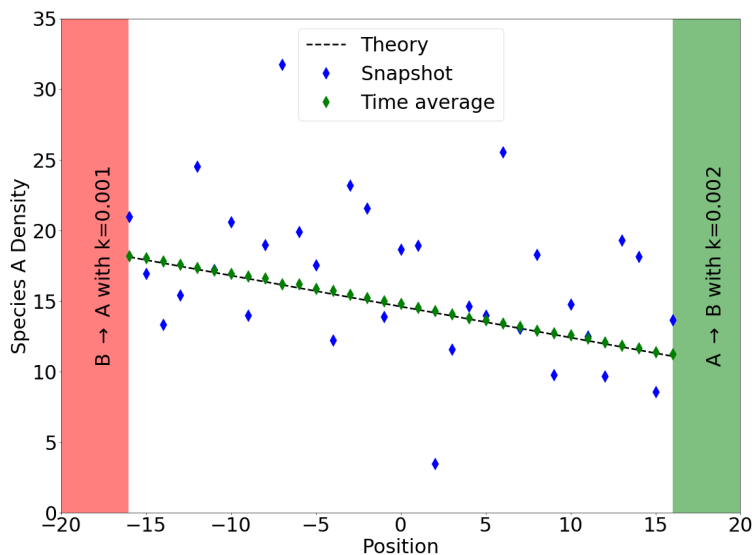$$P(n) = \frac{\bar{n}^n e^{-\bar{n}}}{n!} \quad , \tag{3.30}$$

Figure 3.2.: Density distribution of a slit pore system, where on either side the opposite reaction takes place. For the time average 10000 uncorrelated time steps were used.

where $\bar{n} = N\frac{v}{V}$. We compare the simulation data obtained from the fluctuating EK model against this equation. Additionally, we also compare the data to the density histogram obtained via a MD simulation of non-interacting particles based on the Langevin equation. The results are displayed in Figure 3.3, which show that the MD simulation and the EK model simulation are in good agreement with the theoretical prediction.
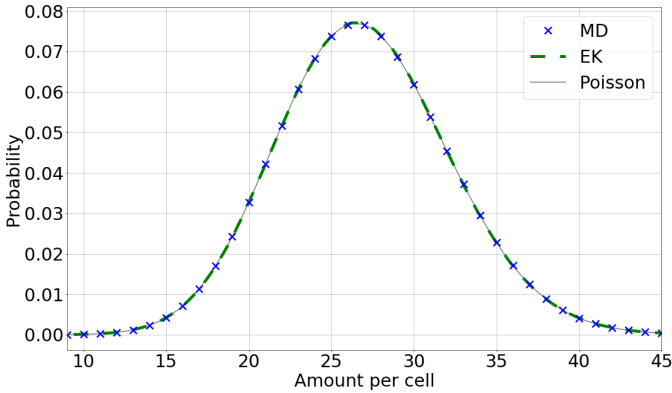
Figure 3.3.: Comparison of the density histogram of an ideal gas for a fluctuating EK simulation (green), a MD simulation (blue), and the predicted theoretical distribution (grey).

The measurement of the density histogram was performed for different stencils to analyze the grid dependency. This yielded an average deviation from the theory for the D3Q19 stencil of $\overline{\Delta P}_{D3Q19} = 5.5 \cdot 10^{-5}$. For the D3Q7 stencil this resulted in $\overline{\Delta P}_{D3Q7} = 5.1 \cdot 10^{-5}$ and for the D3Q27 stencil we found

$\overline{\Delta P}_{D3Q27} = 6.5 \cdot 10^{-5}$. These deviations are three orders of magnitude smaller then the maximum value, and the differences between these values result from statistical inaccuracies and not from methodological discrepancies. A measurement with twice the grid spacing was also performed which resulted in $\overline{\Delta P}_{D3Q19,2} = 1.5 \cdot 10^{-4}$. While here the differences compared to theory are significant larger then for the normal grid spacing, the number of measurements which accumulate to the histogram is also divided by a factor of 8. Therefore the error of such a measurement should be larger by a factor of $2\sqrt{2}$, which matches the deviation we measure.

Next, we demonstrate that the electrostatic solver works in conjunction with thermal fluctuations. To this end, we examine the density histogram of a Coulomb gas containing an equal amount of positively and negatively charged ions. Since an analytical prediction is not available, we compared the EK simulation against a MD simulation of charged particles. In the MD simulation, the charges have to be prevented from coming too close to each other. This is accomplished using an excluded-volume interaction like the **W**eeks-**C**handler-**A**nderson (WCA) potential [61]. The results of those simulations can be found in Figure 3.4. While the EK model provides a good approximation of the MD simulation, is has a slightly larger variance, which likely originates from the fact that the MD simulation contains excluded volume interaction, whereas the EK model does not.
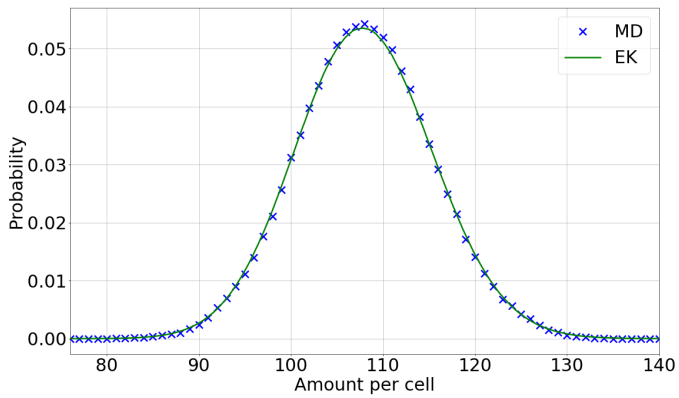
Figure 3.4.: Comparison of the density histogram for a Coulomb gas for the fluctuating EK simulation (green) and the MD simulation (blue).

3.3.3. Effect of Thermal Fluctuations on the Rate of Chemical Reactions

While the fluctuations do not change the equilibrium state of a system, they can have an influence on the dynamics of sufficiently complex systems. As an example, we consider the case of a reactive system where the reaction rate depends nonlinearly on the concentration of the species. In other words, the reaction order is not equal to one.

For example, let us look at the reaction of

$$2A \rightarrow B \quad . \tag{3.31}$$

We can then define the rate equation as

$$\frac{d\rho_B(t)}{dt} = -\frac{1}{2}\frac{d\rho_A(t)}{dt} = k\rho_A(t)^2 \quad , \tag{3.32}$$

where k is the reaction rate constant. With the initial concentration of $\rho_A(0) = \rho_0$ and $\rho_B(0) = 0$, the product density is obtained as

$$\rho_B(t) = \frac{\rho_0}{2}\left(1 - \frac{1}{2kt\rho_0 + 1}\right) \quad . \tag{3.33}$$

However, when fluctuations take place, the density-dependent term $\rho_A(t)^2$ of Equation (3.32) needs to be replaced by its expectation value $\langle\rho_A(t)^2\rangle$. Under the assumption that at any time during the reaction ρ_A follows an ideal gas distribution, and approximating the Poisson distribution (Eq. (3.30)) by a Gaussian distribution with mean $\langle\rho_A\rangle$ and variance $\sqrt{\langle\rho_a\rangle}$, the expectation value is given by

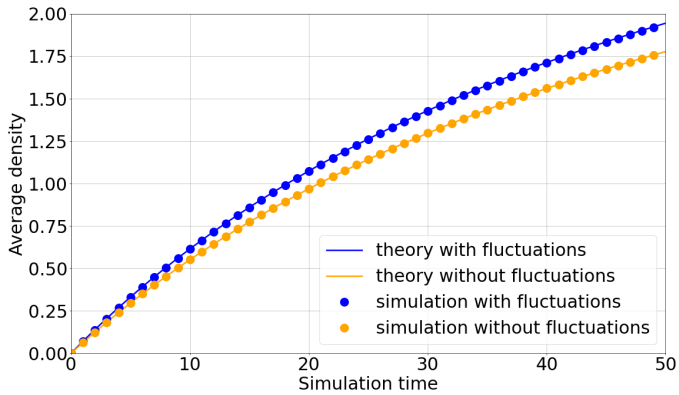$$\langle\rho_A^2\rangle = \langle\rho_a\rangle^2 + \langle\rho_A\rangle \quad . \tag{3.34}$$

Figure 3.5.: Reaction product density plotted over time. The reaction is of the type $2A \rightarrow B$, where the reaction rate was set to $r \propto [A]^2$. The initial density was set to be $\rho_A(0) = 8$. The theory curves are from Equations (3.33) and (3.35).

Inserting this into Eq. (3.32) and solving the **o**rdinary **d**ifferential **e**quations (ODE) yields a product density of

$$\widetilde{\rho}_B(t) = \frac{\rho_0}{2} \left(1 - \frac{1}{e^{2kt} (\rho_0 + 1) - \rho_0} \right) \quad , \tag{3.35}$$

which differs from eq. (3.32). A plot of those product densities is displayed in Figure 3.5. It can be seen that with fluctuations the amount of product B created over time is larger than without the fluctuations. Both cases are in good agreement with the theoretical predictions.

3.3.4. Reaction-Advection-Diffusion with Fluctuations

To demonstrate that all of the aforementioned algorithms can be applied together, we have set up a model reaction-advection-diffusion system. It consists of a channel system in which the reaction $2A + B \rightarrow C$ takes place. We divided the inlet of the substrates into 3 equal parts. The upper and lower one are used for injecting species A, and in the middle part of the channel species B is injected.

The fluid advects the species through the channel, and the diffusion leads to a broadening of the density profile while the substrates move along the channel. In the growing area where species A and B overlap, the reaction can take place and the product C is created. The fluctuations add noise to all 3 density profiles. An image of this system is displayed in Figure 3.6. This shows a broadening of the density profiles of species A and B along the flow direction due to diffusion. Species C can only be created at the interfaces between species A and B, however, due to the broadening of the density profiles in the
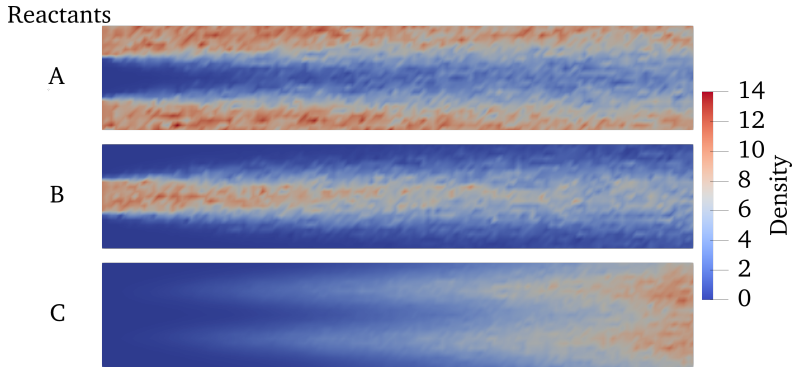
Figure 3.6.: Reactant and product densities in a channel with fluid driving them from left to right. The reaction taking place has the form $2A + B \rightarrow C$. The upper two images show the density of educt species A and B and the bottom one is the product density C. As inlet and outlet boundary conditions we used constant density and velocity boundary condition. The density is defined in simulation units.

later part of the channel, the intersection between those spe-
cies increases, which also leads to more product being created.
The fluctuations can be observed in all three species profiles.

The influence of fluctuations on such a system are shown
in Figure 3.7, where we show the amount of products that
leaves the channel. As theoretically expected, the fluctuations
have a significant impact on the turnover rate of this reaction,
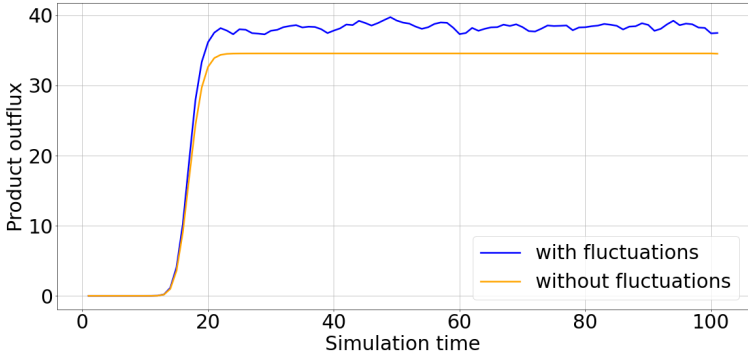where we obtain an increase of 11% over the simulation without
fluctuations.

Figure 3.7.: The amount of products that flows out of the chan-
nel over time. The channel system is described in
Figure 3.6. For comparison the system was meas-
ured with and without thermal fluctuations.

3.4. Applicability on the catalytic mesopore system

Despite the success of the implementation, it turns out that this model is not feasible to be applied to the catalytic reactions in the mesopores. The reason for this is that the reaction rate is rather slow compared to the diffusion driven transport. With a grid resolution that is fine enough to model the mesopore, we will be at a scale, where one molecular catalyst needs to be represented by one or even multiple grid cells. The number of substrate molecules a single catalyst can turn over per second usually ranges from 10^{-2} s^{-1} to 10^2 s^{-1} [1]. Even with a fast catalyst, we still need a long enough simulation to form enough products for them to have an influence on the system. However, the time scale we are working on is determined by the diffusion coefficients, which are in the ranges of $D \approx 1$ nm^{2}ns^{-1} for the substrate molecules that we are interested in [2]. This shows that the diffusion processes inside of the pores are on the nanosecond time scale, while the reactions take milliseconds to occur. This means that the system is in a local diffusive equilibrium, where any products produces are transported away immediately. Applying the fluctuating advection-diffusion-reaction method on such systems would simply result in a constant density profile.

This means that a model like this needs to be applied on a slightly larger scale, where transport and reactions are on similar scales. For example, instead of looking inside of the pores, where the catalysts are immobilized, we move one step outward an investigate how the substrate moves towards and away from the pores in the first place. Because one pore contains multiple catalysts, the reaction is faster. Also, due the not being limited in the grid resolution to the mesopore anymore, bigger

time steps can also be applied. So these systems could look like some sort of transport pores branching into the reaction pores. This, however, will be subject of future research that has not been pursued in this thesis.

3.5. Summary

Fluctuations play an important role in many dynamical processes on the nanoscale, and depending on the system under consideration, it may be necessary to include these fluctuation to have consistent physical description of reaction-advection-diffusion processes. We discussed in this chapter how to combine mesh-based solvers for thermalized EK, chemical reactions, and fluctuating hydrodynamics. Apart from the physical consistency, we demonstrated that thermal fluctuations need to be added to the EK solver to correctly reproduce the chemical reactions rates when the reaction order is not unity. Furthermore, when using an unthermalized EK model coupled to a thermalized LB solver, the thermal energy of the LB fluid would be depleted by the unthermalized EK solver. A similar depletion can be expected when a thermalized MD simulation is coupled to an unthermalized EK or hydrodynamic solver.

We furthermore described two implementations of the reaction-advection-diffusion algorithms. The implementation is based on automatic code generation using pystencils and lbmpy, and is provided as a jupyter notebook in the appendix B or at the data repository [112].

However, it turned out that this model is not feasible to be applied to the currently researched topic of the CRC 1333, due to the slow reactions in comparison to the diffusion of

the reactants. Therefore, in the next chapters we change to a coarse-grained MD model.

4. Random Walk Analysis of the Ring-Closing Metathesis

This chapter is based on the following publication. My contribution were the random walk analysis, simulations and data analysis.

Since the continuum approach is not feasible for the analysis of catalysis in confinement, we decided to go one step deeper on the simulation scales and use a coarse-grained MD model. This will then be applied to a specific reaction rather than a general one. One promising reaction for this study was ring-closing metathesis (Section 2.1.1), which has also been studied experimentally by the **C**ollaborative **R**esearch **C**enter (CRC) 1333.

The idea of how confinement affects this reaction is quite simple. Polymer chains near impenetrable walls have a smaller number of possible configurations. On the premise that ring closure can only occur when the ends of a polymer are close together, we can assume that removing all configurations

where the polymer ends are on different sides of a wall should increase the likelihood that the ends are close together. Adding curvature to this effect could lead to a focusing effect, like a curved mirror.

Although this idea seems plausible, we wanted a more detailed theoretical description. So before modeling this reaction in a coarse-grained simulation, we used polymer theory to gain some quantitative insights into the issue of end-to-end distances of polymers near surfaces.

This investigation was carried out in two parts. First, we used a random walk where the origin is at a fixed distance from a reflecting flat wall. Here we can mathematically analyze how the end-to-end distance and the probability of the free end being near the origin is affected by the wall. In the second part, we use an united atom **m**olecular **d**ynamics (MD) model where one end is tethered at a distance from a wall. With this, we wanted to see if the theory holds up and what the effects of the excluded volumes are.

4.1. Random Walk Theory close to Reflecting Surface

From the theory of a freely jointed chain 2.2 we know that the probability to end such a chain at $\mathbf{x}$ in 3D space is given by:

$$\mathcal{P}(\mathbf{x}) = \left(\frac{3}{2\pi R^2} \right)^{\frac{3}{2}} e^{\frac{-3\mathbf{x}^2}{2R^2}} \quad , \tag{4.1}$$

where we have introduced the length of the random walk, $R^2 = Nb^2$, with the Kuhn-length b.
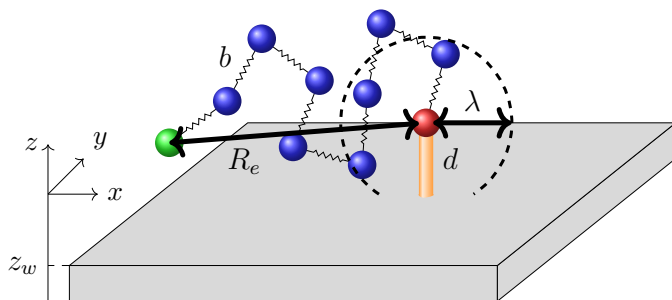
Figure 4.1.: Illustration of the polymer model. The origin of the chain (red) is held in place at a fixed linker length d. R_e marks the end-to-end distance between the beginning and the end (green) of the chain. The dashed circle indicates the reaction radius λ of the sphere over which Equation (4.6) is integrated.

4. Random Walk Analysis of the Ring-Closing Metathesis

Considering all random walks which have the same end-to-end distance $R_e = |\mathbf{x}|$ from the origin we obtain the probability distribution $\mathcal{P}_e(R_e)$ by integrating Eq. (4.1) over the surface of a sphere of radius R_e:

$$\mathcal{P}_e(R_e) = 4\pi R_e^2 \left(\frac{3}{2\pi R^2} \right)^{\frac{3}{2}} e^{\frac{-3R_e^2}{2R^2}} \quad . \qquad (4.2)$$

To investigate interfacial and confinement effects on a random walk we introduce a reflecting wall at $z_w = -d$ (see Figure 4.1). A reflection occurs if in step i, a displacement is selected that would end in $z_i - z_w < 0$. In this case, the z-coordinate is mirrored at the wall such that $z_i = |z_i - z_w|$. While this approach does not conserve the step length b upon a collision with the wall, it has the advantage of a well-defined inert, and impenetrable wall, without any additional degrees of freedom. The corresponding random walk now starts a distance d away from the surface, which corresponds to the distance of a stiff linker fixing polymer in space. The probability distribution function to find the other end of the polymer at position $\mathbf{x}$, is then given by [113]:

$$\mathcal{P}(\mathbf{x}, d) = \begin{cases} \mathcal{P}(\mathbf{x}) + \mathcal{P}(2d\hat{\mathbf{e}}_z - \mathbf{x}) & z \geq -d \\ 0 & z < -d \end{cases} \quad . \qquad (4.3)$$

Integration over the surface of a sphere of size R_e to obtain the end-to-end distance yields:

$$\mathcal{P}_e(R_e, d) = \frac{\mathcal{P}_e(R_e)}{2} \left[\int_0^{\theta_e} \sin(\theta_e) \left(1 + e^{\frac{-6d(d + R_e \cos(\theta_e))}{R^2}} \right) d\theta_e \right]$$

$$= \frac{\mathcal{P}_e(R_e)}{2} \left[\frac{R^2}{6dR_e} \left(e^{\frac{-6d(d + R_e \cos(\theta_e))}{R^2}} - e^{\frac{-6d(d + R_e)}{R^2}} \right) \right.$$

$$\left. + 1 - \cos(\theta_e) \right] \tag{4.4}$$

$$\text{with} \quad \theta_e = \begin{cases} \pi & R_e \leq d \\ \pi - \arccos\left(\frac{d}{R_e}\right) & R_e > d \end{cases} \quad ,$$

which describes the end-to-end distribution of a random walk confined by a flat wall at distance d.

We now investigate the influence of the end-to-end probability distribution Eq. (4.4) on the ring-closing probability. Whilst the latter depends on many variables including the local environment, diffusion, and transport of the substrate etc., here we assume that this scales linearly with polymer return probability $\mathcal{P}_{pr}(d, \lambda)$. This assumption holds to leading order, as the ring-closing can only happen if the two polymer ends meet at least a characteristic distance λ away from catalytic center, as indicated in Figure 4.1. The reaction radius λ thus describes a sphere around the origin encapsulating the details of the catalytic reaction. The polymer return probability is correspondingly obtained by integrating the end-to-end distribution up to λ by

$$\mathcal{P}_{pr}(\lambda, d) = \int_0^{\lambda} \mathcal{P}_e(R_e, d) \, dR_e \quad . \tag{4.5}$$

It is instructive to compare the polymer return probability close to an interface to the case where the polymer is in bulk ("free" case, i.e. the polymer does not interact with the surface in the limit $d \to \infty$). To this end, we define the excess return probability due to the wall as

$$\mathcal{P}_{ex}(\lambda, d) = \frac{\mathcal{P}_{pr}(\lambda, d)}{\mathcal{P}_{pr}(\lambda, \infty)} - 1 \quad . \tag{4.6}$$

Equation (4.6) directly yields the increase in return probability — which we assume to be proportional to the selectivity increase — for an ideal polymer attached to a surface at a linker distance d.

To connect the ideal polymers that underlie a random walk to chemically realistic alkane chains below, we rescale all lengths in our model by the Kuhn length defined as [46]:

$$b = \frac{\langle R_e^2 \rangle}{R_{\max}} = \frac{\langle R_e^2 \rangle}{(n-1)l \cos\left(\frac{\theta}{2}\right)} \quad . \tag{4.7}$$

Here, $R_{\max}$ is the maximal end-to-end distance of the polymer in equilibrium, n is the number of monomers, l is the bond length, and θ is the bond angle of the chemically realistic chains. This allows the mapping of the end-to-end distance to an equivalent freely jointed chain of segment length b, with the corresponding number of Kuhn segments

$$N = \frac{R_{\max}}{b} \quad . \tag{4.8}$$

Using such a mapping, any polymer will display the same average and-to-end distance as a random walk, in the limit of long polymers.

4.2. Polymer Simulation

We model n-alkane chains using a chemically realistic united atom force field, with potential energy functions summarized in Table 4.1. The solvent was treated implicitly via Langevin dynamics with the Verlet integration scheme. To match the diffusion coefficient of methane, we chose a friction coefficient of $\gamma = 2.566/k_\mathrm{B}T$. We set the temperature to $T = 300$ K, and the timestep to $\Delta t = 8$ fs. The total time over which each simulation was sampled was $t = 160$ μs. In analogy to the experiments performed by Ziegler et al.[2], simulations for two sets of chain lengths $n \in \{18, 28\}$ were performed using the ESPResSo software package[20].

   In line with the theoretical considerations above we get rid of additional simulation parameters by employing a purely reflective wall. Particle positions which, after a position update are within the wall, are reflected according to $z_i = |z_i - z_w|$, and their velocities in z-direction are reversed. The position of the $n = 1$ monomer was fixed at a distance d from the reflecting wall and the end-to-end distance distribution was sampled for $d \in [0 \text{ Å}, 19 \text{ Å}]$. The sampling resolution was $\Delta d = 0.25$ Å for $4 \text{ Å} < d < 14 \text{ Å}$, and $\Delta d = 1$ Å in all other cases.

4.3. Comparison of Theory and Simulations

The resulting end-to-end distance probability distribution from Equation (4.4), and the united atom MD simulations, are found in Figure 4.2. For the random walk theory one can easily proof that the random walk case for $d/b = 0$, i.e. the random walk starts on the wall, is equal to the end-to-end distance probability distribution of an unconfined (free) random walk. This is

Table 4.1.: United atom force field parameters taken from Ref. [114]. The Lennard-Jones interactions have only been accounted for if between the two particles of the chain, there are at least 3 other particles (1-4 exclusion).

Pair bond potential $E(r) = \frac{k_r}{2}(r - r_0)^2$		
Pair	r_0 [Å]	k [kcal/mol/Å^2]
CH_2 - CH_2	1.53	899
CH_2 - CH_3	1.53	899

Angle bond potential $E(\theta) = \frac{k_\theta}{2}(\theta - \theta_0)^2$		
Pair	θ_0 [°]	k_θ [kcal/mol/rad^2]
CH_2 - CH_2 - CH_2	112	120
CH_2 - CH_2 - CH_3	112	120

Dihedral bond potential
$$E(\phi) = \frac{1}{2}\left[k_\phi^1\left(1 - \cos(\phi)\right) + k_\phi^2\left(1 - \cos(2\phi)\right) + k_\phi^3\left(1 - \cos(3\phi)\right)\right]$$

Pair	k_ϕ^1 [kcal/mol]	k_ϕ^2 [kcal/mol]	k_ϕ^3 [kcal/mol]
CH_2 - CH_2 - CH_2 - CH_2	1.6	-0.8	3.24
CH_2 - CH_2 - CH_2 - CH_3	1.6	-0.8	3.24

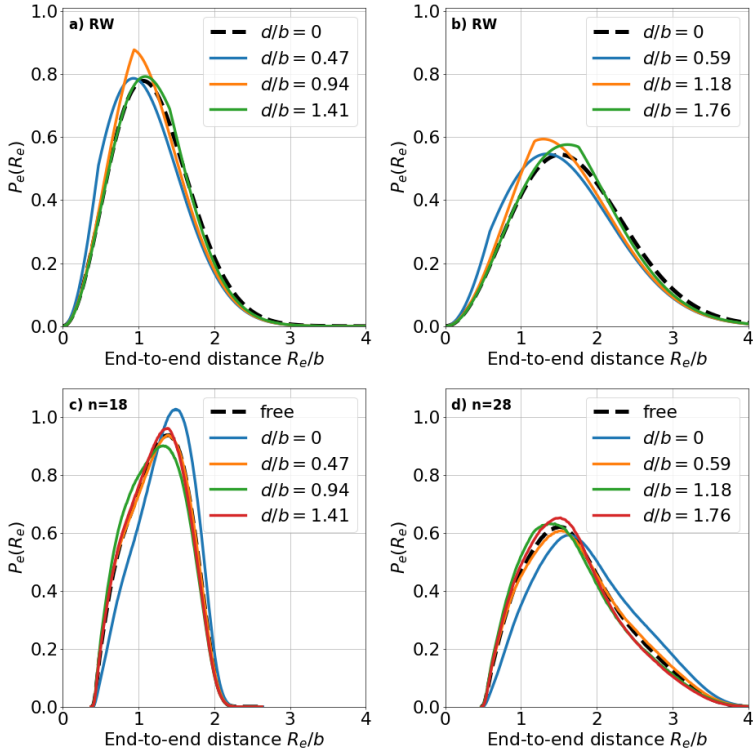| LJ-parameters $E(r) = 4\epsilon\left[\left(\frac{\sigma}{r}\right)^{12} - \left(\frac{\sigma}{r}\right)^6\right]$		
Pair	σ [Å]	ϵ [kcal/mol]
$CH_2 \cdots CH_2$	4.009	0.09344
$CH_2 \cdots CH_3$	4.009	0.14546
$CH_3 \cdots CH_3$	4.009	0.22644

Figure 4.2.: End-to-end probability distributions obtained via random walk theory (top) using Equation (4.4) and simulations (bottom) for the polymer chain lengths 18 (left) and 28 (right). The theoretical model used the Kuhn length b, and corresponding Kuhn segments N, calculated from the simulation data (Equation (4.7) and (4.8)). For the shorter chain these parameters are $b_{18} = 8.5$, and $N_{18} = 1.71$. For the longer chain, they are $b_{28} = 6.8$ and $N_{28} = 3.49$.

due to the symmetry of the system.

Moving the starting location slightly away from the wall results in a shift towards smaller end-to-end distances. If one increases the distance d to values of about the average end-to-end distance of the free random walk, the end-to-end distance starts to approach the free case again. This time, however, the peak of the distribution gets larger, while the longer end-to-end distances appear less frequently. For even larger values of d, the peak shifts back to larger end-to-end distances, where again P_e lies above the free random walk. For even larger values of d, the distribution will converge to that of a free random walk which is an obvious result as the effects of the wall are rarely noticed by the monomers. This behavior can be observed for both chain lengths. The main difference is the observation that the longer chain prefers longer end-to-end distances.

From our simulations using the united atom model, we observe that the $n = 18$ chain for $d/b = 0$ varies strongly from the $n = 28$ chain. In both cases, it is important to note that the particle is practically embedded in the wall, and the chain starting from that point can only extend in the direction away from the boundary. Therefore, excluded volume effects contribute significantly to the end-to-end distribution, and correspondingly, $P_e(R_e)$ is shifted to larger end-to-end distances. For longer chain lengths, and large distances, the excluded volume effects become less important, and the distribution functions approach the analytical solution for the random walk (see Figures 4.3(b) and (d)). Notably, at a certain distances d, the distribution functions for realistic polymer chains favor shorter end-to-end distances when compared to the random walk. The simulation of chain length $n = 28$ is long enough to behave as

predicted from a random walk model, with the exception of the excluded volume at short end-to-end distances. The shorter chain, however, does not fit the model, and tends towards larger end-to-end distances.

Investigating the excess return probability (Figure 4.3), we observe a maximum in all 4 cases considered. For the analytical solution, we observe a dependency on the reaction radius λ, which is not present in the simulation data. This reaction radius, however, is not of experimental significance, as it corresponds to details of the reaction. The maximum itself on the other hand, tells us that we can have a significant increase in the polymer return probability, which further translates into a boost of the ring-closing probability. For our simulation we therefore would have expanded the ring-closing probability by 18.5%, given the optimal distance to the wall.

As can be observed from our simulation results in Figure 4.3(c) and (d), the simulation show a range where the excess return probability is negative. This is both due to the excluded volume of the **L**ennard-**J**ones (LJ) particles, which repel each other, and the stiffness of the polymer, and thus is expected to also correspond to real polymers anchored close to a wall.

4.4. Summary

We have investigated how the probability distribution of end-to-end distances for a single polymer chain changes when one end of the polymer is fixed at a certain distance from a reflecting wall. For an ideal chain, this can be done analytically via classical polymer theory. While we did not measure the ring-closing probability directly, we assumed that it is linearly
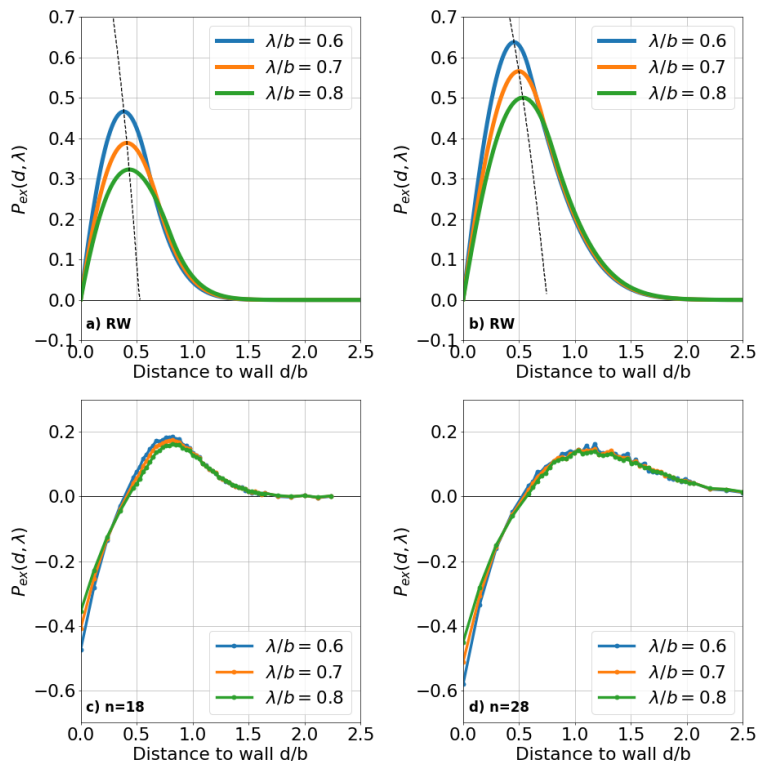
Figure 4.3.: Excess return probability as defined in Equation (4.6). In the top row plots a) and b), we plot P_e of the analytical random walk solution, for three values of λ/b, calculated via the corresponding parameters of the equivalent freely jointed chain. The dotted line indicates the position of maxima for other values of λ/b. In the bottom plots c) and d), we display the corresponding P_e of the simulation results for the united atom alkane chains with n monomers.

related to the probability that both polymer ends find each other within a certain reaction radius λ. Under this assumption, we examined the excess return probability, which shows the corresponding change in said probability due to the wall constraint.

From the theory of classical random walks, there is a non-monotonic excess probability that is always positive and has a maximum that depends on the chain length and varies monotonically with d. Since the Gaussian chain lacks any molecular interactions, we also performed the same investigations by performing molecular dynamics simulations of a united atom alkane model. The comparison with the random walk model was performed by mapping the conformational properties of the united atom model, onto that of an equivalent freely jointed chain. In both theory and simulation, we found an optimum in the excess return probability, revealing a linker length that maximizes the ring-closing probability. For the simulation of a polymer with $n = 18$ monomer units, we could measure an increase of up to 18.5 % in comparison to a free polymer chain, whereas for the $n = 28$ chain, the increase was reduced to about 14.5 %, albeit with a broader maximum. The optimal distances for the spacer length were for both cases about 7 Å, although the distribution is much broader for the longer chain. Interestingly, the ring-closing probability depended only weakly on λ for the interacting chain simulations.

The advantage of single chain simulations is that they run very fast and allow for an easy change of the confining geometry and chain parameters. However, in this study, we completely neglected the polymer-catalyst and polymer-polymer interactions, which may play an important role during process

of ring-closing metathesis.

Overall, we have achieved what we set out to do in this study, namely to show that the geometric constraints imposed on a polymer can improve the ring-closing probability. In the next chapter, we build on these findings to further investigate the ring-closing promoting properties of confinement.

5. Coarse-grained metathesis reaction analysis

This chapter is based on the following publication. My contribution were the development of the metathesis model, system modeling, simulations data analysis.

Knowing from polymer theory that even a flat wall can have a significant effect on the ring-closing probability of the metathesis reaction, we developed a model to emulate this reaction in an MD simulation. However, modeling reactions with MD is usually not an easy task. There are some reactive force fields such as ReaxFF [115, 116, 117] that can model various chemical reactions at the atomic level through the formation and breaking of molecular bonds. With such an approach, one can correctly determine the kinetics of a single reaction. Although it would have been possible to perform a single metathesis reaction with such a force field, we are more interested in the statistics of many reactions. However, this again leads to the problem that the reaction of a single molecular catalyst is very

slow compared to the diffusion processes, and with one reaction every 10 milliseconds on average, it is impossible to collect enough data to do statistics at the atomistic level.

Since an atomistic simulation was out of the question, we knew we needed a coarse-grained approach to model the reaction. Such techniques have proved fruitful before, for example in the Readdy simulation package [118, 119] or in the model of Akkermans et al. [120], which uses specific cutoff lengths for bond formation and breakage and is employed in the study of polymerizations [121, 122, 123]. Since we are only interested in the probabilities of ring closure and polymerization and not the kinetics, we can lower the energy barrier of the reaction so that it happens whenever the reactants are present. This leads to an enormous acceleration, so that many more reactions can take place. On the other hand, this should not affect the selectivity significantly, as it should speed up both reaction pathways in the same way. The model we came up with is able to create bonds on collision of certain particles with the catalyst. These bonds will then be broken at a predefined rate.

With this model, our aim was to investigate which geometrical factors lead to an increase in the ring closure probability of the metathesis reaction when the catalyst is located in mesopores. The SBA15 materials of the experiments [2, 3] are basically cylindrical pores and therefore induce curvature, inclusion and surface effects. Knowing that surface effects themselves increase the probability of ring closure, we wanted to disentangle these three effects by simulating the reaction in different geometries. To measure the surface effects, we chose a flat wall as the system geometry with the catalyst tethered to it. Secondly, we investigated a slit pore system with differ-

ent widths, so that we can increase the confinement step wise while keeping the surface effects constant. And finally, we re-created the cylindrical pore, which produces curvature effects in addition to the other effects.

5.1. Methods

In this section we describe the different models used within our simulations, including the polymer model, the reaction mechanism and the coupling to the reservoir. The simulation framework utilized for this is ESPResSo [20].

5.1.1. Polymer Model

In our simulations, the substrate oligomers are represented by Kremer-Grest polymers [63], which repel via a WCA potential (Equation (2.39)) and attract via a FENE potential (Equation (2.41)).

$$U^{\mathrm{LJ}}(r) = 4\epsilon \left[\left(\frac{\sigma}{r} \right)^{12} - \left(\frac{\sigma}{r} \right)^{6} \right] \quad , \tag{2.38}$$

$$U^{\mathrm{WCA}}(r) = \begin{cases} U^{\mathrm{LJ}}(r) - U^{\mathrm{LJ}}(\sqrt[6]{2}\sigma) & r < \sqrt[6]{2}\sigma \\ 0 & \text{else} \end{cases} \quad , \tag{2.39}$$

$$U^{\mathrm{FENE}}(r) = -\frac{1}{2} K^{\mathrm{FENE}} \Delta r_{\max}^2 \ln \left[1 - \left(\frac{r}{\Delta r_{\max}} \right)^2 \right] \ . \tag{2.41}$$

Here, ϵ and σ define the length and energy scales of the **W**eeks-**C**handler-**A**nderson (WCA) potential, $r_{\max}$ defines the distance where the bonded potential diverges and K is the strength

$$
\begin{array}{ccccc}
& R_0 & & R_0 & & R_0 \\
& / & & / & & / \\
M = C_0 & & M - C_0 & & M \quad C_0 \\
& & | \quad | & & \| \quad \| \\
C_1 = C_2 & & C_1 - C_2 & & C_1 \quad C_2 \\
/ \qquad \backslash & & / \qquad \backslash & & / \qquad \backslash \\
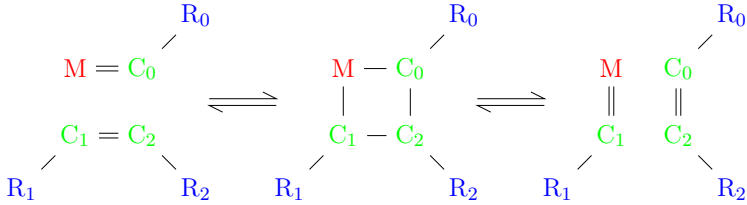R_1 \qquad R_2 & & R_1 \qquad R_2 & & R_1 \qquad R_2
\end{array}
$$

Figure 5.1.: Reaction mechanism of the olefin metathesis. M represents the metal atom at the center of the catalyst.

of the FENE (**f**inite **ex**tension **n**on-linear **e**lastic) potential. For simplicity, we considered only linear chains, consisting of two different numbers of monomers $N_m \in \{22, 29\}$. The number of monomers of these oligomers were chosen to resemble substrates 1 and 4 in the experiments by Ziegler et al. [3], since these resemble reasonably well a linear polymer chain. To include the rigidity of the molecule, we added a harmonic angular potential between the individual beads that has an equilibrium angle of $\phi_0 = 180°$:

$$
U^{\text{angle}}(\phi) = \frac{K^{\text{angle}}}{2}(\phi - \phi_0)^2 \quad . \tag{5.1}
$$

The strength of this potential K^{angle} is a free parameter of the model used to fit the selectivity of our homogeneous reaction to the experimental values.

5.1.2. The Metathesis Model

The reaction mechanism [124, 17] of the olefin metathesis we want to mimic is illustrated in Figure 5.1. A metal atom is

located in the center of the catalyst complex. This metal atom is the central part of the reaction and can form or break bonds to the substrate molecules. We assume that initially, the metal atom has already formed a double bond with a carbon atom which we will call C_0. Substrate carbon atoms that share a double bond can attach to the catalyst and are denoted by C_1 and C_2. When C_1 binds to the catalyst, the double bond between C_1 and C_2 is reduced to a single bond. The same happens to the bond between the metal atom and C_0. To keep the total number of bonds constant, C_0 and C_2 also form a bond. Thus, C_0, C_2, C_1 and the metal atom have formed a 4-fold ring. Two carbon atoms can then split off from this ring, so that the carbon pair C_0 and C_2 are freed and C_1 remains bonded to the metal atom. During this reaction the bonding partners of the substrate double bonds have swapped. This process does not interfere with any other chains attached to the carbon atoms.

In our coarse-grained approach, we model the catalyst as a large particle that has two active sites on its surface which can form the two bonds that the metal atom can accept. If one of the active sites already has a bond, it will be deactivated until it releases the bond particle. The substrate molecules are simple bead-spring chains in which each bead corresponds to a carbon atom. The first two and last two monomers of each chain are labeled as the carbon atoms that share a double bond. These labeled carbon atoms can form a bond with the catalyst once they collide with the active site. The probability that this bond will be accepted is called P_{bond}. The carbon atom of a pair that collides first obtains the bond, while the other forms a bond with the particle that was bonded to the catalyst before

the reaction. These bonds formed during the reaction process are treated as harmonic bonds, because distance between the particles when the bonds are created can vary strongly, which can lead the FENE bonds to be over extended. The such created a 4-fold ring can break open to release another pair of labeled particles. This breakup is triggered at a predefined rate τ_{break}^{-1}. During the breaking process, if C_0 and C_2 remain bonded together, the harmonic bond between them is replaced by a FENE bond to be consistent with the rest of the oligomer.

Although this method technically allows for modeling a generic metathesis reaction, we applied it here to the specific case of a α, ω-diene metathesis reaction. In that case there are two opposite reaction paths of ring-closing and polymerization. In both cases, a substrate molecule is already bound to the catalyst, and the reaction pathway depends on whether the next metathesis process starts with the olefin bond on the other side of the molecule or from a completely different substrate molecule. A schematic picture of how this diene metathesis proceeds in the model can be seen in Figure 5.2. Technically, it is also possible for the olefin bond to attach with C_1 and C_2 atoms being swapped, but this only leads to an unproductive reaction cycle in which only the carbon atom bonded to the catalyst is exchanged and the reaction continues as if this has not happened.

While this simple model is subject to some limitations, many of them can be overlooked as we are only interested in modeling the selectivity of the reaction. First, we ignore the inconsistencies in the binding energy of the different molecules during the reaction. When a bond is formed, a pair potential is created between two particles that may not be in equilib-

116

rium, causing a change in local energy. However, due to the thermalization of the entire system, this is quickly dissipated. Additionally, the driving force of the reaction stems more from the entropy of the created ethylene than from the enthalpy change due to the negligible ring strain of macrocycles. Second, since we are not interested in the kinetics of the reaction itself, we accelerate the reaction by increasing the breakage rate of the 4-membered ring and also by increasing the probability of accepting the bond upon collision to $P_{\text{bond}} = 1$. This is done such that reaction and diffusion occur on the same timescale. This acceleration of the reaction should only affect the throughput and not the selectivity. Contrary to the experiments our catalyst is an ideal catalyst that is infinitely stable. However, for our simulations we use a **g**rand **c**anonical **M**onte-**C**arlo (GCMC) reservoir which controls the concentration of the reactants to emulate a system state in which the reaction is always in its early stages. Next, the catalyst is modeled as a sphere and neglects the ligands that strongly affect the reaction. While the ligands usually play an important role in defining the catalytic properties, we have neglected these properties in the development of our model. And finally, due to our coarse grained polymer model, we also avoid the topic of stereoselectivity. These limitations have only a minor effect on the selectivity and are overcome by the parametrization of the bond angle potential mentioned earlier.

5.1.3. GCMC Reservoir

From the experiments there are two important conditions that we would like to keep in our simulational approach: Firstly, that the reaction takes place within the confinement of the pore

(a) Acyclic diene metathesis.
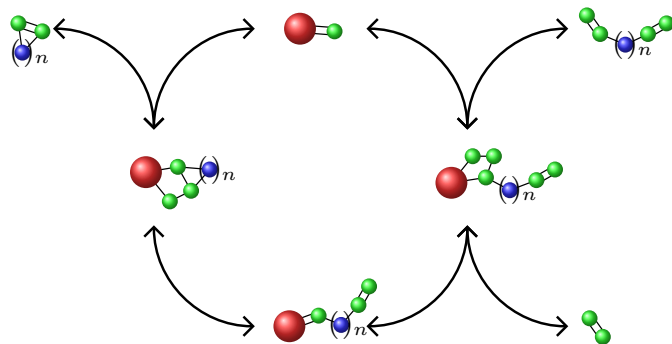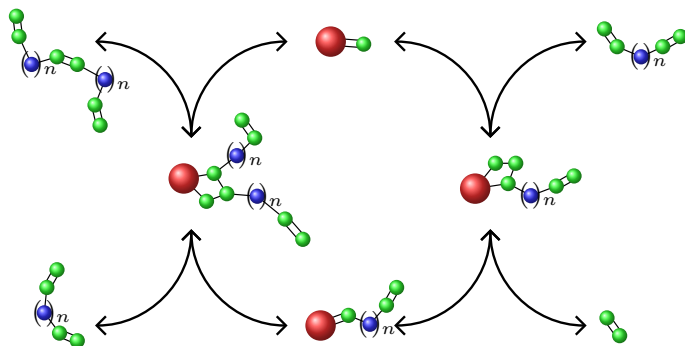

(b) Ring-closing metathesis.

Figure 5.2.: Scheme of different pathways for a diene metathe-
sis reaction. The catalyst is shown in red, the
green particles denote those carbon atoms that
share a double bond. Only these can attach to the
catalyst. The other backbone carbon atoms are
depicted in blue. In (a) we see the different path-
ways of an acyclic diene metathesis. In (b) we ob-
serve a ring-closing metathesis. In the center top,
and center bottom stages, the catalyst can accept
a bond from the the green particles. In the center
of the picture the bonds have been formed. The
reaction can either continue forward, (clockwise)
or backward (counter clockwise). This depends on
the order with which the bonds will break. The
right path for both reactions is the same up to the
point where either (a) a carbon chain is attached
to the catalyst, or (b) the two ends of the chain
close onto themselves to form a ring.

and secondly that the diffusion processes into and out of the pore are handled accordingly. As the reaction is addressed as described above, we now mimic the diffusion of substrate and product in and out of the pore. To model the diffusion process, we consider a finite porous media (i.e., the interface, the slit or the cylindrical pore) embedded in reservoir where the reactants are dissolved in. This reservoir region is treated via the Grand Canonical Monte Carlo (GCMC) technique [125]. Thus, substrate can be introduced into the system and products can be removed from it. GCMC is a simple technique to impose the fixed chemical potential of a reservoir to the system of interest i.e. the pore. It works by removing or inserting a molecule via a trial move. The probability $\mathcal{P}$ for accepting this move is given by the Boltzmann-coefficient, which results in:

$$\mathcal{P}_{\text{in}} = \min\left[1, \frac{V\Lambda^{-3}}{N+1}\exp\left(\frac{\mu - \Delta U}{k_{\text{B}}T}\right)\right] \qquad \text{and} \qquad (5.2)$$

$$\mathcal{P}_{\text{out}} = \min\left[1, \frac{N}{V\Lambda^{-3}}\exp\left(\frac{-\mu - \Delta U}{k_{\text{B}}T}\right)\right] \qquad , \qquad (5.3)$$

where V is the volume of the system, Λ is a normalization factor, N is the number of molecules in the system prior to the move, μ is the desired chemical potential and ΔE is the energy difference of the insertion/removal moves, which are accepted according to a Metropolis scheme. For our simulation, we remove the products from the reservoir region of the system by setting their chemical potential to $\mu_{\text{product}} = -\infty$. This circumvents the problem that one needs to specify the composition of the products when handling them with a finite chemical potential. To account for diffusion effects, we define a specific region around the catalyst that is not coupled to

the reservoir, which means that the molecules must diffuse toward and away from the catalyst. The latter allows to count the ratio of polymerized N_P and ring-closed N_P molecules to determine the ring-closing selectivity S_{RC}:

$$S_{RC} = \frac{N_{RC}}{N_{RC} + N_P} \quad . \tag{2.4}$$

Following this protocol, we simulate the reaction in a steady state, mimicking the experimental situation at the beginning of the reaction.

5.2. System Set-up

In order to study the various effects when confining a system, we investigated a total of four different realizations, with varying levels of confinement: bulk, a flat wall, slit pores and cylindrical pores (as seen in Figure 5.3). The bulk system represents the homogeneous catalysis without any confinement. A flat wall with periodic boundary conditions is used to study surface effects with an otherwise open system. The slit pore goes further in the sense that it confines the catalyst from both sides. By varying the slit width we can therefore control the contribution of this confinement effect. Finally, using a cylindrical pore with variable radius, we also add the effect of curvature to our study.

The bulk system is depicted in Figure 5.3a. The positions of the catalysts are fixed within the system box. This was done to suppress possible catalyst-catalyst interactions. The spacial region that couples to the reservoir has some distance from the catalysts. This is similar to homogeneous reaction experiments. In the experiments of Ziegler et al., a catalyst loading
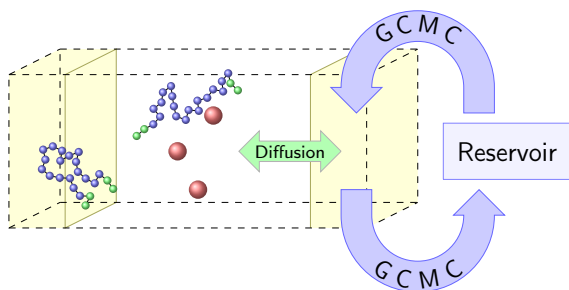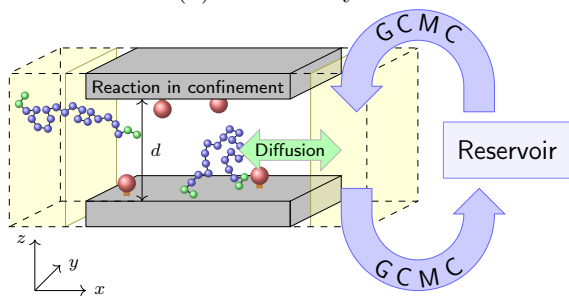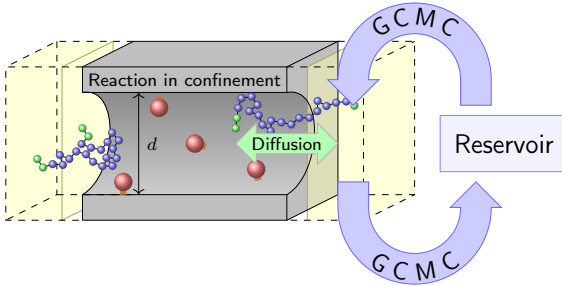
(a) Bulk system
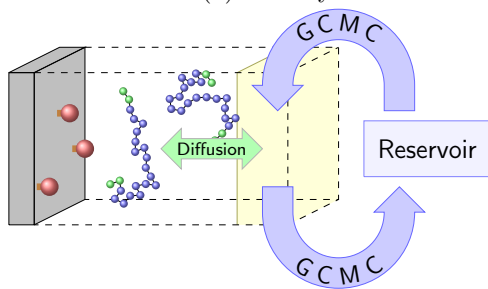
(b) Flat wall system

(c) Slit pore system

(d) Cylindrical pore system

Figure 5.3.: Illustration of the different systems. In all systems, the catalysts are fixed in space, so the reactants must diffuse to them. Only the areas highlighted in yellow are coupled to the reservoir, which imposes a chemical potential on the system. Substrates are introduced into this coupled volume and products are withdrawn. The system itself is periodic in all directions.

of 1 mol % is used, meaning that the catalyst to substrate ratio is 1:100. However, due to the influx of substrate particles from the reservoir the catalyst loading cannot be rigorously defined for our system. Therefore, we used the catalyst density as a free parameter and after some testing it turned out not to have a significant impact on the selectivity as long as the catalysts are far enough apart such that the attached chains do not interact with one another. The resulting catalyst density that we chose was $\rho_{\text{cat}}^{\text{bulk}} = 0.0018$ nm^{-3} at an average substrate density of $\rho = 0.015$ nm^{-3}.

In the other systems, the catalyst is placed near a wall. An illustration of the catalysts near a wall can be seen in Figure 5.4. The catalyst consists of a central impenetrable sphere to which two permeable active sites are attached. The position and rotation of the catalysts are fixed. The centers of the active sites are spaced $d_{\text{cat}} = 0.7$ nm from the wall. According to a previous study [126], this should maximize the probability that the end of the molecule returns to its origin, increasing the probability of ring closure. The catalyst model has many parameters, which could potentially influence the selectivity. For simplicity, we chose a size for the core that is similar to the size of the actual catalyst. The active sites are large enough such that the reaction event is triggered sufficiently frequent to gather good statistics. The spacing between the active sites was chosen such that the 4-fold ring that occurs during the reaction is not overstretched. The reaction is calibrated by parametrizing the angular binding potential of the substrate oligomers as discussed above.

For the number of catalysts in the pore, in order to make the different systems comparable, we chose a constant cata-
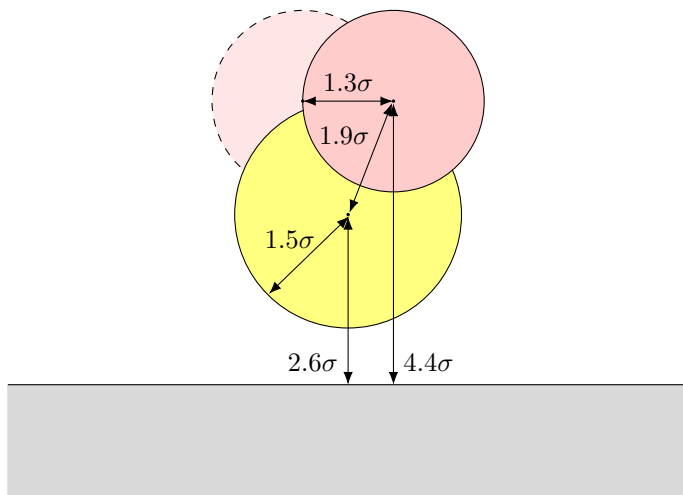
Figure 5.4.: Illustration of the catalyst geometry. All length-
scales are given with respect to the diameter of our
carbon atoms, $\sigma = 1.535$ Å. The yellow sphere is
the impenetrable holder of the reactive sites (red).
The pale, dashed one resembles the inactive reac-
tion side, which already has a particle bond to it.
These reactive sites are permeable, but if the cen-
ter of a particle with an olefin bond passes into
this region, it will attach to the reactive site. Dur-
ing the reaction it is impossible that both reactive
sites are active at the same time.

lyst surface density for all pore types at $\sigma_{\text{cat}} = 0.036$ nm^{-2}. Due to the curvature of the cylindrical pore, we chose not to measure the surface density at the pore wall, but rather at the place where all active sites are located. This corresponds to a distance of d_{cat} from the curved wall. This allows for a better comparison between slit and cylindrical pores.

The flat wall system is depicted in Figure 5.3b. The volume coupled to the reservoir starts at a distance of $d = 9$ nm perpendicular to the boundary. This system will provide insight into the interfacial effects that occur in this and the two following systems. All wall surfaces are treated as analytical walls, meaning that there are no explicit wall atoms and the interaction between the wall and the molecules is treated by a purely repulsive WCA potential with the length scale $\sigma = 1.535$ Å and the energy scale $\epsilon = 0.833$ $k_{\text{B}}T$. This is approach is also the followed in the pore systems.

The slit pore system (Figure 5.3c) consists of a finite slit pore with length $l = 35.8$ nm. The width of the pore in the periodic direction is $L_y = 10.21$ nm. The catalysts are located at a fixed location inside. We varied the distance between the two walls between 2 nm $\leq d_{\text{slit}} \leq 6$ nm. Due to the constant pore surface area of these different runs, the number of catalysts in the pore was kept constant at $N_{\text{slit}} = 13$.

The cylindrical pore system (Figure 5.3d) is the one most similar to the experimental setup (by Ziegler et al.). Here, we employ a finite cylindrical pore that is open at both ends. The length of the pore itself is $l = 35.8$ nm. We varied the radius between 1.15 nm $\leq r \leq 3.15$ nm. To extrapolate to the limit of large pores, we also ran a simulation with $r = 6.15$ nm.

The simulation box also consists of a volume outside the

pore that spans $L_x = 34.2$ nm in the longitudinal direction and $L_y = L_z = 10.21$ nm in the other two directions. Within this volume, GCMC moves can take place, however, we also added a padding of $L_{pad} = 5$ nm away from the pore entry to account for diffusional effects.

The substrate density in this reservoir in the simulations is chosen to match the experiments by Ziegler et al. with 0.015 molecules per nm^3. At this low density, molecules on average are not close enough to interact when molecules are added or removed. This allows us to treat the substrate as if it were an ideal gas. However, due to intramolecular interactions, the internal energy of the inserted chains is non-zero. Therefore, the inserted molecules must be in a configuration that follows Boltzmann statistics. We obtained these configurations by sampling configurations of a single molecule. For each inserted molecule, one of these configurations is randomly selected.

Since the intramolecular energy is accounted for from the collected samples and the intermolecular energy is negligible due to the low density ($\Delta U \approx 0$), we can assume that the chemical excess potential $\mu_{\text{substrate}} = 0$. The resulting equilibrium substrate densities are $\rho_{22}^{\text{bulk}} = 0.0145\text{nm}^{-3}$ and $\rho_{29} = 0.0142\text{nm}^{-3}$, which is about 5% less than the concentration in the experiments. This deviation is caused by an underestimation of the chemical potential, by assuming that the interaction energy of the substrate oligomers is zero.

Each system examined in this study was simulated using $N = 8$ independent simulation runs and the average values were used for analysis. The marked errors in the graphs are the standard deviation over all runs. The run time of the simu-
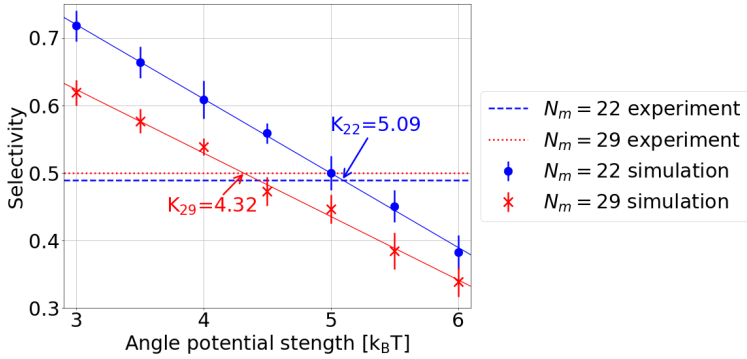
Figure 5.5.: Calibration simulation of the angle bond stiffness, which has been determined to be $K_{22} = 5.09 k_{\mathrm{B}}T$ and $K_{29} = 4.32 k_{\mathrm{B}}T$.

lation was not predefined, but rather the simulation were interrupted once the errorbars were considered small enough. The system temperature was set to $T = 300$ K using a Langevin thermostat.

5.3. Simulation Results

5.3.1. Bond Angle Calibration

For the bond angle potential of our polymer model, we determined $K_{22}^{\mathrm{angle}} = 5.09 \ k_{\mathrm{B}}T$ and $K_{29}^{\mathrm{angle}} = 4.32 \ k_{\mathrm{B}}T$, to yield sufficient agreement with the experimental data (see Figure 5.5). With this stiffness the hydrodynamic radii of our substrate
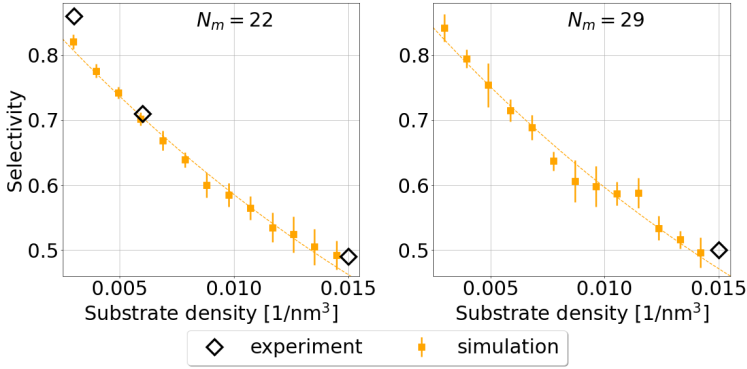
Figure 5.6.: Density dependence of the homogeneous reaction. The fitting curve is an exponential function.

oligomers were calculated according to Doi and Edwards [52]:

$$\frac{1}{R_H} = \frac{2}{N(N-1)} \sum_{i=1} \sum_{j<i} \frac{1}{|\mathbf{r}_i - \mathbf{r}_j|} \quad . \tag{5.4}$$

For the longer chain we obtained $R_{H29} = 0.59 \pm 0.01$ nm, while the experimental value is $R_{H29}^{\text{ex}} = 0.53$ nm. For the shorter chain we compare the simulated value of $R_{H22} = 0.51 \pm 0.01$ nm to the experimentally determined value of $R_{H22}^{\text{ex}} = 0.44$ nm. With respect to the coarse-grained level of our simulations, we found the agreement to be sufficient.

5.3.2. Homogeneous Reaction

We first investigated the concentration dependence of the substrate on the ring-closing selectivity. A decrease in concentration leads to a lower probability that a molecule from the
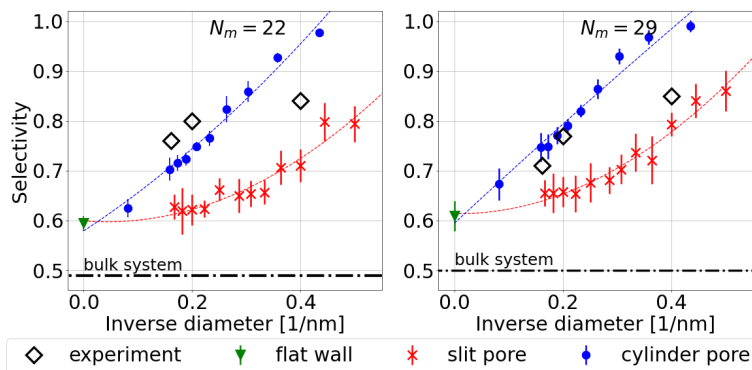
Figure 5.7.: Selectivity against the inverse pore diameter/slit width. The result of the bulk reaction at the same reservoir substrate concentration is shown in the dash dotted line. The fitting function is a second degree polynomial.

solution will collide with a catalyst. This subsequently will increase the residence time that a molecule is bound to a catalyst which in turn increases the time a substrate has for ring closure. The resulting data of the substrate concentration dependence on the ring-closing selectivity is shown in Figure 5.6. It clearly demonstrates that lower densities lead to a higher ring-closing selectivity. Our results are in excellent agreement with the experimental data by Ziegler et al. [3] and thus validate the calibration of the simulation model.

5.3.3. Reaction inside of Different Pores

We now place the catalysts into systems which are bound by a single flat interface, inside slit pores of different widths, and cylindrical pores of different radii in order to investigate varying degrees of confinement: interfacial effects, the presence of confining surfaces, and geometrical curvature effects. In Figure 5.7, we report the measured selectivities of our simulations. In detail, we plot the selectivities against the inverse diameter of the pores in order to highlight the convergence towards the limiting case of a flat wall, which is reached in the limit $d \to \infty$. The selectivity significantly increases with increasing degree of confinement. Interestingly we note that the pure planar interface effect emerging from a flat wall alone increases the ring-closing selectivity already from 49% to 58%. Investigating a slit pore, where we added a second surface at some distance away, further enhances the selectivity depending on the width of the pore. This way, we achieved selectivities ranging from 63% for $d = 6.0$ nm up to 79% for $d = 2$ nm. Moving further from a slit to a cylindrical pore, curvature effects come into play: The selectivity changes from 70% for a diameter of $d = 6.3$ nm up to 97.7% for $d = 2.3$ nm. We additionally simulated a cylindrical pore with $d = 12.3$ nm in order to bridge the gap to the case of a flat wall. If we plot the simulated selectivity against the inverse diameter, the selectivity increase is found to be almost linear for the cylindrical pores (Figure 5.7). Importantly, both, the cylindrical and the slit pore selectivities, converge towards the flat planar interface result in the case of large diameters.

While the simulations slightly underestimate the experimental values for the larger pore sizes ($d \in \{6.3 \text{ nm}, 5.0 \text{ nm}\}$), the selectivity was overestimated for smaller pores. The main reason
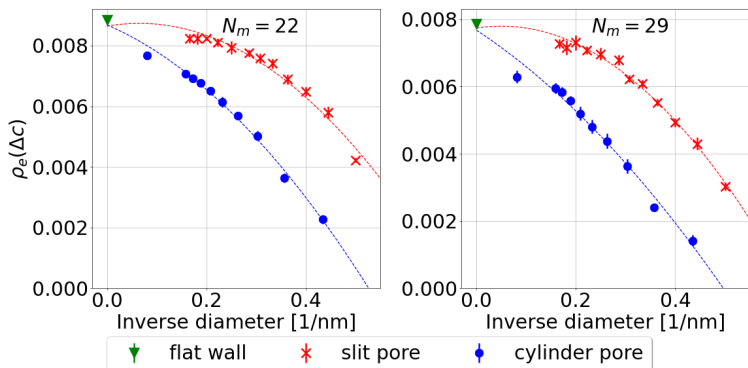
Figure 5.8.: Local end-monomer density of the substrates at the region of the catalyst $\rho_e(\Delta c)$ vs the inverse pore diameter. The region of the catalyst is defined as the position of the active centers with an added margin. So measured from the wall the region is: $\Delta c = (0.7\pm0.3)$nm. The fitting function is a second degree polynomial.

for this is that our model does not include any specific polymer-wall interactions that occur between the ester compounds and the silica pore. Since the goal of this study is not to investigate chemistry specific effects we explicitly decided to not include this kind of interactions in our approach, which might explain some of the deviations between the simulated and experimental values.

More in detail, in our model we have only steric, and therefore repulsive interactions included, thus there are only a few factors that can cause confinement effects. To shed further

light onto this, we investigated the local density profile of the end-monomers, $\rho_e(\Delta c)$, of the substrate as a function of the distance to the wall. The end-monomer density instead of e.g. the center of mass density was chosen since only the ends can bind to the catalyst. The distance range away from the surface, in which we measured was the position of the reactive centers plus/minus the catalyst size, correspondingly is $\Delta c = (0.7 \pm 0.3)$ nm. In Figure 5.8, this local density is plotted against the inverse diameter. Classical polymer theory predicts that the oligomer density decreases near an impenetrable wall for entropic reasons. This can be observed in our simulations in the case of a flat wall, where the density near the wall, $\rho_e^{\text{flat}} = 0.0089\text{nm}^{-3}$, is much lower than far from the wall, $\rho^{\text{bulk}} = 0.0145\text{nm}^{-3}$. This effect is even more pronounced inside a pore, where two interfaces or a curved boundary act on the substrate. For decreasing pore size, the reduction in the local density around the catalyst is increased. Additionally, due to curvature effects, the cylindrical pores have a lower local density than the slit pores with the same diameter.

The local end-monomer density for the slit pores (red data in Figure 5.8) appears to saturate for small inverse pore width, yet this saturating local density in the large pores is lower than the local density near a single flat wall (green triangle in Figure 5.8). This can be explained by the fact that the system is not in diffusive equilibrium, i.e., there is a substrate density gradient along the longitudinal pore axis due to the drainage of the substrate during the reaction. This gradient can be observed in Figure 5.9. For a better comparison we simulated a slit pore system, without catalysts or reactions. In that case, the local density for large slit pores recovered the same value
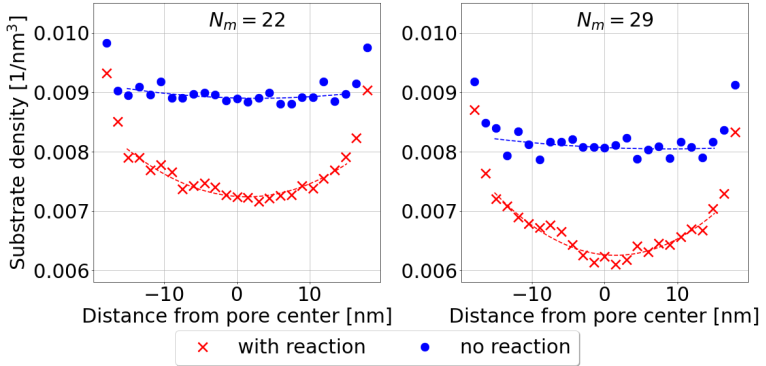
Figure 5.9.: Density distribution of the substrate along the axis of a slit pore with a width of $d = 4$ nm. For comparison, the system was simulated with and without reactions. The density increase at the end of the pore ($|x| > 16$ nm) indicates the transition to the bulk outside the pore. Diffusion of substrates into the pore and drainage of substrates within the pore due to the reaction result in a density gradient toward the center of the pore.
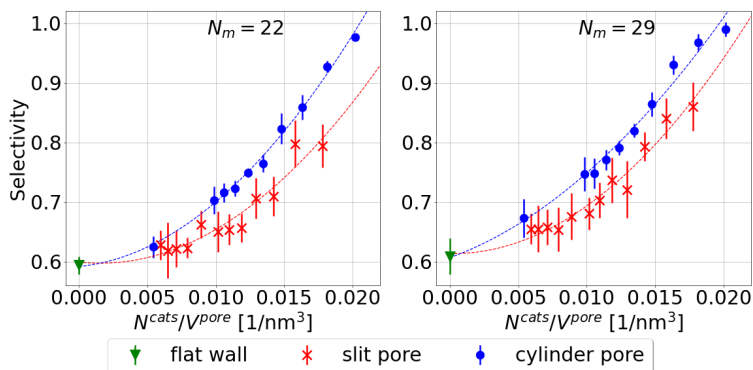
Figure 5.10.: Selectivity vs the catalyst density inside the pore. The difference in selectivity of the cylindrical and the slit pore within this image allows for an insight into the curvature effects. The fitting function is a second degree polynomial.

as in the flat wall case. Although the observed density gradient along the pore axis in our simulations is partially due to the increased reaction rate in the simulations compared to the experimental olefin metathesis, such effects are always appearing in the case of fast reactions or in sufficiently long pores, which depending on the material can easily extend to the micrometer scale.

In general, comparing cylindrical and slit pores at the same diameter can be misleading, since volume and surface area scale differently for the two types of pores. For our simulations, where we vary the pore size, we therefore used a constant catalyst surface density to eliminate the different surface scaling.

In order to elucidate the effect of the catalyst volume density $\frac{N^{\text{cat}}}{V^{\text{pore}}}$ on the selectivity, we present the corresponding simulation data in Figure 5.10. This representation allows comparing confinement and surface effects at the same volume and surface density of the catalyst. Our simulation results reveal – as expected – a strong increase of the selectivity with increasing catalyst volume density, however, the cylindrical pores at the same values $\frac{N^{\text{cat}}}{V^{\text{pore}}}$ reveal selectivities that are about 10% higher for the cylindrical pores. Since the simulations are performed at fixed catalyst surface density, relating the pore volume to a degree of confinement allows identifying this difference in the selectivity with curvature effects.

Finally, our simulations allow for correlating the obtained local end-monomer density and selectivity for the different systems examined. In the limit of large pores (right data in Figure 5.11), the selectivity increase in pores perfectly coincides with the change of the substrate density in bulk (yellow data) and also with the selectivity increase at a planar interface (green triangle). The vertical dashed line in Figure 5.11 indicates the limit where a direct proportionality to the density change is observed, i.e. the transition to confinement effects. For the parameters investigated here this transition occurs roughly at $r \approx 6\,\text{nm}$ for cylindrical pores and $d \approx 3\,\text{nm}$ for the slit pores. For smaller pores, the measured selectivity outperforms the bulk reaction at the same density, implying that the local end-monomer density cannot be the only source for the selectivity increase. Confinement must therefore directly affect the ring closure process by reducing the number of possible configurations for the substrate. Again, the increase is more pronounced for cylindrical pores than for slit pores,
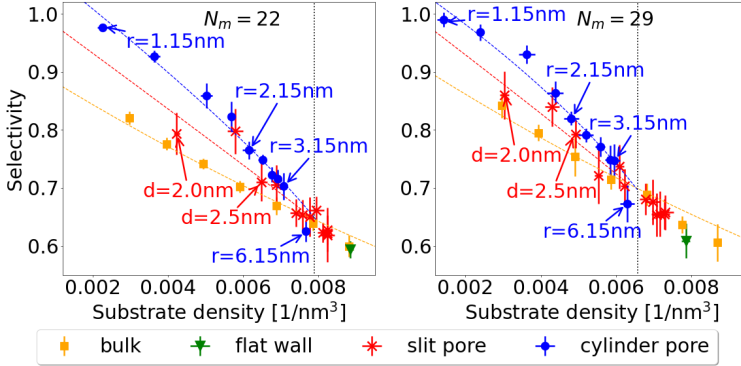
Figure 5.11.: Selectivity vs. local density of the substrate ends. Smaller pores show lower local substrate densities. Bulk here refers to the homogeneous reaction at the given substrate density. For small pores the measured selectivity is larger than the selectivity of a homogeneous reaction at the same density and cylindrical pores reveal a higher selectivity compared to slit pores. The vertical dotted line marks the upper bound of the region, where confinement effects are observed, i.e. data for bulk, in the pores and at a planar interface become indistinguishable.

revealing that curvature amplifies this effect, i.e. the configurational degrees of freedom of the substrate at a curved interface are reduced much stronger than at a planar interface, and thus enhancing the ring-closing probability.

5.4. Summary

We have developed a coarse-grained model for studying a generic catalytically activated ring-closing polymerization reaction near an unstructured catalyst. Using particle-based grand-canonical molecular dynamics simulations and a collision-based reaction mechanism we parametrized our model to reproduce the bulk ring closing selectivities of a diene metathesis reaction studied in a recent work by Ziegler et al. [3]. This was done for substrate polymers consisting of $N_m = 22$ and $N_m = 29$ monomers. For the homogeneous reaction we recovered the expected reduction of the ring-closing selectivity with increasing substrate density. While this is a well-known fact, it demonstrates the validity of our modeling approach.

Using this model we performed an extensive investigation of the effects of the presence of a wall near the catalysts. In accordance with our previous analytical work [126], we also found with our simulational approach that the presence of a wall enhances the excess return probability of chain ends, which leads to a corresponding change in the ring-closing probability due the wall constraint. For all systems investigated in the present work, we could measure an increase in the ring-closing selectivity when compared to the selectivity measured in a homogeneous system at the same substrate reservoir density. We quantified this wall-effect and demonstrated that it stems from

the reduction of the density of substrate chain ends near the catalysts.

We then continued to investigate slit pores and cylindrical nanopores of various sizes to systematically disentangle confinement effects from wall induced effects. Interestingly enough, there is a further increase in ring-closing selectivity if we geometrically confine the catalysis. This stems from the fact that the density of chain ends near the catalysts decrease further due to a reduction in overall substrate density within the pore and is therefore a pure confinement effect. Noteworthy, we observed that for small pores the increase cannot be related to the local density alone, but is rather due to two additional effects: (i) if the pore size becomes comparable to the typical length of the substrate, the conformational degrees of freedom are restricted and thus, the return probability is further enhanced (this can be observed e.g. for slit pores < 3 nm). (ii) the observed selectivity enhancement is much stronger for the cylindrical pores studied, indicating that curvature further enhances the return probability and thus the selectivity. The latter effect increases with the pore curvature, i.e. as $1/r$ in perfect agreement with the observations from our simulations. The experimental data of the metathesis reactions studied by Ziegler et al. [3] show a good agreement with our observed trends.

Summing up, we can always relate the increase of the ring-closing selectivity to the reduction of substrate density close to the catalyst which, however, varied for the different systems. In particular, the strong dependence on wall curvature effects was unexpected and could likely be exploited with specially corrugated surfaces that have optimal shape for the em-

ployed substrate particles. With our catalytic coarse-grained model at hand, one could investigate confinement effects also for other pore geometries and substrates to make a prediction about which kind of geometry would be optimal for the catalytic process.

6. Conclusion

In this work, we used computer simulations to investigate the topic of molecular catalysis in confinement. We started from a continuum scale with a fluctuating-advection-diffusion-reaction system where the transport properties were of interest. To gain a more detailed insight into the confinement-induced changes in the internal polymer structure during the diene metathesis reaction, we moved to a finer scale using particle based models. Here random walk theory was applied to polymers near boundaries and we compared them to particle based simulations modeled with a united atom force field. For the final part, we scaled up this polymer reaction and developed a model to study the different effects of surface, confinement and curvature within a mesoporous system.

We have extended the electrokinetic method in ESPResSo by adding flux thermalization and reactions. The thermal fluctuations allowed us to study smaller systems where these fluctuations become relevant. The reactions, on the other hand, enable us to model the transformation of the different species either locally at a defined catalyst or as a bulk reaction. We discussed the implementation and were able to show the excellent scaling with system size of this method. For validation, different systems were tested to show the correct behavior. It was also demonstrated that the fluctuations are important when studying reactions that have a reaction order not equal to one. In the end, however, it turned out that this method

was not applicable for the current study of molecular catalysis in mesopores, as the reaction of individual catalysts is too slow compared to the diffusion inside the pores. In the future, however, this method could be of use when transport pores are considered.

Realizing that the scale of continuum simulations is too coarse, we went a step down on the refinement scale and decided to investigate the issue using particle-based simulations. To this end, we studied the ring-closing metathesis reaction to analyze how and to what extent confinement affects the selectivity of this reaction. In the beginning polymer theory was applied to a random walk originating at a fixed distance from a flat reflecting wall. Under this constraint, it could be shown that the end-to-end distance distribution is significantly affected by the distance between the origin and the wall. The maximum of this distribution can shift to smaller end-to-end distances for small distances between the origin and the wall, or be more pronounced for larger distances between the origin and the wall. For comparison, a simulation with united atoms was also utilized, which showed similar behavior, but due to the excluded volume of this model, these effects were less pronounced.

In addition, we analyzed how likely it was that the random walk/polymer would end near its origin. We defined the excess return probability as the increase in return probability when the origin is near a wall compared to the free polymer model. This analysis yielded a maximum for both the random walk and **m**olecular **d**ynamics (MD) simulations, suggesting that there is an optimal linker length that maximizes the probability of a polymer closing in on itself. This optimal linker length is

longer for the MD simulation because the excluded volume prevents the ends from being close together. At the optimal linker length, which is about 7 Å for the MD simulation, the probability of return increases by 14.5% to 18.5%, depending on the chain length, compared to the unconstrained polymer. Since the ends must be close together to cause ring closing, this increase in return probability also leads to an increase in ring closing probability.

We have also developed a coarse-grained model that can represent the ring-closing metathesis reaction. This was used to investigate the possible causes of the increase in ring-closing selectivity when the reaction takes place in confinement. We were able to distinguish between surface, confinement and curvature effects, all of which separately increase selectivity. The measured surface effect can be explained in part by the lower local oligomer substrate density near a repulsive surface compared to an unconfined reaction. This lower density leads to a lower number of possible polymerizations and thus favors the ring-closing reaction. While this density depletion due to confinement and curvature effects is stronger than that of a single flat surface, it is not sufficient on its own to explain the selectivity increase for these cases. Thus, within the boundary of a slit or cylindrical pore, the oligomers are restricted in their movements such that the ring-closing process is directly favored. This effect proved to be even more pronounced in curved cylindrical pores than in flat slit pores.

The results obtained in this work are based on idealized assumptions and only work for purely repulsive interactions. In reality, however, these molecular catalytic processes in confinement depend on several other parameters that were not taken

into account. Nevertheless, the measured effects can play an important role, as they complement the results of the other **C**ollaborative **R**esearch **C**enter (CRC) 1333 projects and contribute to a better understanding of the topic of ring-closing metathesis. The presented topics in this thesis laid the foundation for more complex systems. Moreover, with the presented electrokinetic continuum solver, effective models including ionic species can be modeled, such as electrochemical CO_2 conversion, which is a topic of the second funding period of the CRC 1333.

A. Calculation of the normalization factor

This appendix is reused from our publication [127]. The normalization factor A_0 was introduced to ensure that the sum over all included neighbours does not depend on the stencil used. When considering the case with only face neighbours, we obtain

$$\sum_{i \in \text{face}} \frac{1}{a_i A_{0,DdQ(2d+1)}} = 2d, \tag{A.1}$$

where the distance to the face neighbours is always $a_i = 1$. Since we have $2d$ face neighbours there is no need for normalization, and $A_0 = 1$. However, when including edge and corner neighbours for the D3Q27 stencils, the summation becomes

$$\sum_{i \in \text{face}} \frac{1}{a_i A_{0,D3Q27}} + \sum_{i \in \text{edge}} \frac{1}{a_i A_{0,D3Q27}} + \sum_{i \in \text{corner}} \frac{1}{a_i A_{0,D3Q27}} = 6. \tag{A.2}$$

Inserting the number of faces, edges, and corners and their respective distances we get:

$$6 \frac{1}{A_{0,D3Q27}} + 12 \frac{\sqrt{2}}{A_{0,D3Q27}} + 8 \frac{\sqrt{3}}{A_{0,D3Q27}} = 6. \tag{A.3}$$

This yields a normalization factor of $A_{0,D3Q27} = 1 + 2\sqrt{2} + \frac{4}{3}\sqrt{3}$. The same procedure can be used to calculate the normalization factor for any other stencil.

B. Fluctuating advection-diffusion-reaction pystencils script

B.1. Introduction

This script should give an introduction of how to use the fluctuating electrokinetics model in `pystencils`. For the sake of simplicity we are not using `lbmpy` to generate the velocity field, but rather set the velocity to be constant.

B.2. Set-Up

B.2.1. Imports

importing `pystencils.sessions` lets us use many pystencil functions via the abbreviation `ps` and `sympy` functions via `sp`. The also supplyied `poisson.py` will handle the electrostatic interaction using numpys FFT.

```
[1]: from pystencils.session import *
     from pystencils.rng import random_symbol
     import poisson
     import numpy as np
```

B.2.2. Create the grid and needed fields and variables

We will be using the datahandling module of `pystencils` to manage all the fields and communicaions.

```
[2]: L = (32, 32, 32)
     stencil = 19
     species = 2
     dh = ps.create_data_handling(domain_size=L,
                                  periodicity=True,
                                  default_target='cpu')

     # define the fields
     c_fields = []
     j_fields = []
     r_flux_fields = []
     for i in range(species):
         c_fields.append(dh.add_array(f'c_{i}',
                                      values_per_cell=1))
         j_fields.append(dh.add_array(f'j_{i}',
                         values_per_cell=stencil // 2,
                         field_type=ps.FieldType.STAGGERED_FLUX))
         r_flux_fields.append(dh.add_array('r_' + str(i),
      ↪values_per_cell=1))
     velocity_field = dh.add_array('v', values_per_cell=dh.dim)
     pot_field = dh.add_array('Phi', values_per_cell=1)
     charge_field = dh.add_array('q', values_per_cell=1)

     #define the constants
     kT = sp.Symbol("kT")
     dt = sp.Symbol("dt")
     r_rate_const = sp.Symbol("gamma")
     D = sp.Matrix([ps.TypedSymbol(f'D_{i}', np.float64) for i
      ↪in range(species)])
     z = sp.Matrix([ps.TypedSymbol(f'z_{i}', np.float64) for i
      ↪in range(species)])
```

```
r_coefs = sp.Matrix([ps.TypedSymbol(f'n_{i}', np.float64)␣
 ↪for i in range(species)])
r_order = sp.Matrix([ps.TypedSymbol(f'O_{i}', np.float64)␣
 ↪for i in range(species)])

stencil_factor = 1.0
if dh.dim == 2:
    if stencil == 9:
        stencil_factor = np.sqrt(1/(1+np.sqrt(2)))
if dh.dim == 3:
    if stencil == 19:
        stencil_factor = np.sqrt(1/(1+2*np.sqrt(2)))
    if stencil == 27:
        stencil_factor = np.sqrt(1/(1+2*np.sqrt(2)+ 4.0/3.0␣
 ↪* np.sqrt(3)))
```

B.2.3. Specify the diffusion-migration-advection equation and use the automatic FVM discretizer

Here we define the basic advection diffusion equation and write it in `sympy`. THen we use `pystencils` to create a finite volume method out of it. Afterwards the velocity field gets applied and everything is beeing put together.

[3]:
```
def grad(f):
    return sp.Matrix([ps.fd.diff(f, i) for i in range(dh.
 ↪dim)])
def diffusion_equation(c_field, i):
    return - D[i] * grad(c_field) - D[i] * z[i] * c_field.
 ↪center * grad(pot_field)
def advection_diffusion_flux(c_field, j_field, index):
    flux_eq = diffusion_equation(c_field, index)
    fvm_eq = ps.fd.FVM1stOrder(c_field, flux=flux_eq)
    vof_adv = ps.fd.VOF(j_field, velocity_field, c_field)
    flux = []
```

```
    for adv, div in zip(vof_adv, fvm_eq.
↪discrete_flux(j_field)):
        assert adv.lhs == div.lhs
        flux.append(ps.Assignment(adv.lhs, (adv.rhs + div.
↪rhs)*dt))
    return ps.AssignmentCollection(flux)
```

B.2.4. Add the fluctuations to the discrete flux

For the fluctuation we take the flux from the advection diffusion equations, and loop over every direction. From the density of the cells which are connected by the flux, we calculate the amplitude of the fluctuations. This fluctuation term is then added to the advection diffusion assignments.

[4]:
```
def add_fluctuations(flux, c_field, j_field,
                     species_index, stencil_factor):
    rng_symbol_gen = random_symbol(flux.subexpressions,
                                   dim=dh.dim)
    for i in range(len(flux.main_assignments)):
        n = j_field.staggered_stencil[i]
        assert flux.main_assignments[i].lhs == j_field.
↪staggered_access(n)

        # calculate mean density
        dens = (c_field.neighbor_vector(n) + c_field.
↪center_vector)[0]/2
        # multyply by smoothed haviside function so that
↪fluctuation will not get bigger that the density
        dens *= sp.Max(0,sp.Min(1.0,c_field.
↪neighbor_vector(n)[0]) * sp.Min(1.0,c_field.
↪center_vector[0]))

        # lenght of the vector
        length = sp.sqrt(len(j_field.staggered_stencil[i]))
```

```
        # amplitude of the random fluctuations
        fluct = sp.sqrt(2*dens*D[species_index]*dt) * sp.
↪sqrt(1/length) * stencil_factor
        # add fluctuations
        fluct *= 2 * (next(rng_symbol_gen) - 0.5) * sp.
↪sqrt(3)

        flux.main_assignments[i] = ps.Assignment(flux.
↪main_assignments[i].lhs, flux.main_assignments[i].rhs +␣
↪fluct)
    return flux
```

Because the random number on both side of the periodic boundary need to be equal, we fold the system so that the offsets of at the periodic boundary conditions are the same. And with this the RNG will calculate identical numbers for those cases.

[5]:
```
def add_ghostlayer_folding(flux):
    ''' Add the folding to the flux, so that the random␣
↪numbers persist through the ghostlayers.'''
    fold = {ps.astnodes.LoopOverCoordinate.
↪get_loop_counter_symbol(i):
            ps.astnodes.LoopOverCoordinate.
↪get_loop_counter_symbol(i) % L[i] for i in range(len(L))}
    flux.subs(fold)
    return flux
```

B.2.5. Poisson solver via FFT

To solve the electrostatic Poisson equation, the charges are transformed via `numpy` into the fourier space and are solved there.

```
[6]: def init_fft():
         charge_field_rhs = 0
         for i in range(species):
             charge_field_rhs += z[i] * c_fields[i].center
         gather_charges = ps.Assignment(charge_field.center,
                                        charge_field_rhs)
         fft = poisson.FFTReal(dh=dh,
                               phi_field=pot_field,
                               epsilon=sp.Number(1),
                               charge_access=charge_field.center,
                               prefactor=sp.Number(1),
                               opts=None)
         return fft, ps.AssignmentCollection([gather_charges])
```

B.2.6. Add the reaction between the species

Adding the reactions is rather staight forward: loop over the
species to calculate the raction rate via the reaction order equa-
tion. Apply the stochastic fluctuations to the reaction term
and turn the into an `pystencil` assignment.

```
[7]: def reaction_description():
         r_flux = ps.AssignmentCollection([ps.
     ↪Assignment(r_flux_fields[i].center, 0) for i in␣
     ↪range(species)])
         r_cont = ps.AssignmentCollection(
             [ps.Assignment(c_fields[i].center, c_fields[i].
     ↪center + r_flux_fields[i].center) for i in␣
     ↪range(species)])
         rng_symbol_gen = random_symbol(r_flux.subexpressions,
                                        dim=dh.dim)
         rand_number = next(rng_symbol_gen)
         reaction = r_rate_const * dt
         for i in range(species):
             reaction *= sp.Pow(c_fields[i].center, r_order[i])
```

```
    reaction_fluctuations = sp.sqrt(sp.Abs(reaction)) * 2 *␣
→(rand_number - 0.5) * sp.sqrt(3)
    reaction_fluctuations *= sp.Min(1,sp.Abs(reaction)**2)
    for i in range(species):
        r_flux.main_assignments[i] = ps.
→Assignment(r_flux_fields[i].center, (reaction +␣
→reaction_fluctuations) * r_coefs[i])
    return r_flux, r_cont

def reaction_description_no_fluctuations():
    r_flux = ps.AssignmentCollection([ps.
→Assignment(r_flux_fields[i].center, 0) for i in␣
→range(species)])
    r_cont = ps.AssignmentCollection(
        [ps.Assignment(c_fields[i].center, c_fields[i].
→center + r_flux_fields[i].center) for i in␣
→range(species)])
    reaction = r_rate_const * dt
    for i in range(species):
        reaction *= sp.Pow(c_fields[i].center, r_order[i])
    for i in range(species):
        r_flux.main_assignments[i] = ps.
→Assignment(r_flux_fields[i].center, reaction *␣
→r_coefs[i])
    return r_flux, r_cont
```

B.2.7. Init Fields

As initiation we will set the species to a defined desnity and
the other field values to be zeros.

```
[8]:  def init_fields(dens_init):
          for i in range(species):
              dh.fill(c_fields[i].name, np.nan,
                      ghost_layers=True, inner_ghost_layers=True)
              dh.fill(j_fields[i].name, np.nan,
```

```
                ghost_layers=True, inner_ghost_layers=True)
        dh.fill(c_fields[i].name, dens_init[i])
    dh.fill(velocity_field.name, 0,
            ghost_layers=True, inner_ghost_layers=True)
    dh.fill(pot_field.name, 0,
            ghost_layers=True, inner_ghost_layers=True)
    dh.fill(charge_field.name, 0,
            ghost_layers=True, inner_ghost_layers=True)
```

B.2.8. Create the method

Now we call the before defined functions to obtain the pystencils desctription of the model.

```
[9]: fluxes = []
     fluxes_no_fluctuations = []
     for i in range(species):
         flux = advection_diffusion_flux(c_fields[i],
                                         j_fields[i], i)
         fluxes_no_fluctuations.append(flux.copy())
         flux = add_fluctuations(flux, c_fields[i], j_fields[i],
                                 i, stencil_factor)
         flux = add_ghostlayer_folding(flux)
         fluxes.append(flux)

     r_flux, r_cont = reaction_description()
     r_flux_no_fluctuations, r_cont =␣
      ↪reaction_description_no_fluctuations()
```

B.2.9. Compile the generated expressions and set up the ghost-layer communication

The last thing that needs to be done is to compile the assignments into runnable kernels. During this step we also create

154

the synchronization function of the density so that the periodic boundaries can be applied.

```
[10]: flux_kernels = []
      flux_kernels_no_fluctuations = []
      continuity_kernels = []
      sync_fields = []
      for i in range(species):
          flux_kernels.append(ps.
      ↪create_staggered_kernel(fluxes[i]).compile())
          flux_kernels_no_fluctuations.append(ps.
      ↪create_staggered_kernel(fluxes_no_fluctuations[i]).
      ↪compile())
          fvm_eq = ps.fd.FVM1stOrder(c_fields[i],␣
      ↪flux=diffusion_equation(c_fields[i],i))
          continuity_kernels.append(ps.create_kernel(fvm_eq.
      ↪discrete_continuity(j_fields[i])).compile())
          sync_fields.append(c_fields[i].name)

      sync_conc = dh.synchronization_function(sync_fields)

      fft, gather_charges = init_fft()

      gather_charges_kernel = ps.create_kernel(gather_charges).
      ↪compile()
      reaction_kernel = ps.create_kernel(r_flux).compile()
      reaction_kernel_no_fluctuations = ps.
      ↪create_kernel(r_flux_no_fluctuations).compile()
      reaction_continuity_kernel = ps.create_kernel(r_cont).
      ↪compile()
```

B.3. Checking the probability density distribution without electrostatics

Now that the whole method is set up, we will have a look if it functios properly. In ther first test we will analyse the density distribution due to the fluctuation. For this we will set up one species at a constant density and let the fluctuations do their work. At fixed intervalls we will measure the density in cell. Afterwards we plot a histogram of the local densites and compair it with the density distribution of an ideal gas and one obtained from an MD simulation. The data of the MD simulation can be found in the file `ideal_gas_md_hist.dat`.

B.3.1. Set the parameters

```
[11]: time_end = 5000
      save_time = 10
      warm_up = 1000
      seed = 42

      dens_init = [27.0,0.0]
      params = {'dt': 0.001,
                'kT': 1.0,
                'D_0': 1, 'D_1': 1,
                'z_0': 0, 'z_1': 0}
```

B.3.2. Run the simulation

Right now we only need the kernels for the flux and the continuity equation of the first species. After these are handeld the densities are syncronized to handel the parallel boundary conditions.

B.3. Checking the probability density distribution without electrostatics

```
[12]: init_fields(dens_init)

      sync_conc()
      data=[]
      for time in range(time_end+warm_up):
          dh.run_kernel(flux_kernels[0], seed=seed+i,
                        time_step=time, **params)
          dh.run_kernel(continuity_kernels[0])
          sync_conc()
          if(time%save_time==0 and time > warm_up):
              data = np.append(data, dh.gather_array(c_fields[0].
      ↪name).ravel(), 0)
```

B.3.3. Plot the density distribution

```
[13]: def P(rho, dens_init):
          res=[]
          for r in rho:
              res.append(np.power(dens_init,r) * np.
      ↪exp(-dens_init) / np.math.gamma(r+1))
          return np.array(res)
```

```
[14]: md_data = np.loadtxt("ideal_gas_md_hist.dat",skiprows=1)

      dens_value ,bins =np.histogram(data,density=True, bins=300)
      bins_mean=bins[:-1] + (bins[1:]-bins[:-1])/2

      plt.plot(bins,P(np.
      ↪array(bins),dens_init[0]),label="Poisson")
      plt.plot(md_data[:,0],md_data[:,1],'o',label="MD")
      plt.plot(bins_mean,dens_value,label="EK")
      plt.legend()
      plt.xlim(dens_init[0]-2*np.
      ↪sqrt(dens_init[0]),dens_init[0]+2*np.sqrt(dens_init[0]))
```

[14]:   (16.6076951545867, 37.3923048454133)
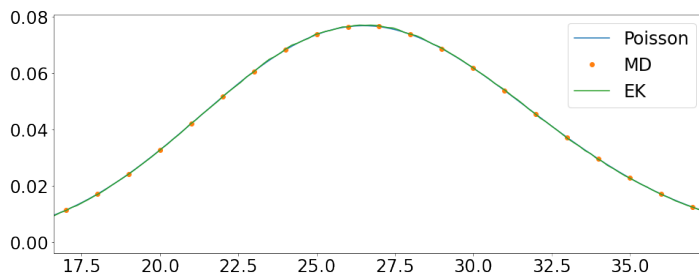
B.4. Checking the probability density distribution with electrostatics

Similar to the first test, we will check the density distribution, however this time we have a coulomb gas of positivly and negativly charged species. The main difference when running this simulation is that we need to loop over every species and that the electeostatics kernels need to be called. To compair the measured data with the MD simulation, the MD data is found in `coulomb_gas_md_hist.dat`

B.4.1. Set the parameters

```
[15]: time_end = 5000
      save_time = 10
      warm_up = 1000
      dens_init = [108.0,108.0]
      seed = 42


      params = {'dt': 0.001,
```

```
          'kT': 1.0,
          'D_0': 1, 'D_1': 1,
          'z_0': 1, 'z_1': -1}
```
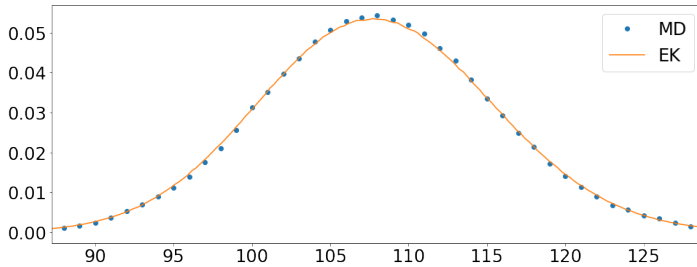
B.4.2. Run the simulation

[16]:
```
init_fields(dens_init)

sync_conc()
data=[]
for time in range(time_end+warm_up):
    dh.run_kernel(gather_charges_kernel, **params)
    fft(**params)
    for i in range(species):
        dh.run_kernel(flux_kernels[i], seed=seed+i,
                      time_step=time, **params)
        dh.run_kernel(continuity_kernels[i])
    sync_conc()
    if(time%save_time==0 and time > warm_up):
        data = np.append(data, dh.gather_array(c_fields[0].
↪name).ravel(), 0)
```

B.4.3. Plot the density distribution

[17]:
```
md_data = np.loadtxt("coulomb_gas_md_hist.dat",skiprows=1)

dens_value ,bins =np.histogram(data,density=True, bins=300)
bins_mean=bins[:-1] + (bins[1:]-bins[:-1])/2

plt.plot(md_data[:,0],md_data[:,1],'o',label="MD")
plt.plot(bins_mean,dens_value,label="EK")
plt.legend()
plt.xlim(dens_init[0]-2*np.
↪sqrt(dens_init[0]),dens_init[0]+2*np.sqrt(dens_init[0]))
```

[17]: (87.2153903091735, 128.784609690827)

B.5. Influence of the fluctuations on the reaction rate

For the last test we simulate a system of two species where they are coupled via the reaction 2A &rightarrow B. At the begining there will be no species B. During the Simulation at fixed time intervalls we sum up the density of species by to measure how much has been created up to this point. This simulation is run with and without fluctuations for comparison.

B.5.1. Set the parameters

[18]:
```
time_end = 5000
save_time = 10
warm_up = 0
dens_init = [8.0, 0.0]
seed = 42

params = {'dt': 0.001,
```

```
            'kT': 1.0,
            'gamma': 0.001,
            'D_0': 1, 'D_1': 1,
            'n_0':-2, 'n_1': 1,
            'O_0': 2, 'O_1': 0,
            'z_0': 0, 'z_1': 0}
```

B.5.2. Run the simulation with fluctuations

[19]:
```
init_fields(dens_init)

sync_conc()
data=[]
for time in range(time_end):
    dh.run_kernel(reaction_kernel, seed=seed+species,
                  time_step=time, **params)
    for i in range(species):
        dh.run_kernel(flux_kernels[i], seed=seed+i,
                      time_step=time, **params)
        dh.run_kernel(continuity_kernels[i])
    dh.run_kernel(reaction_continuity_kernel)
    sync_conc()
    if(time%save_time==0):
        data = np.append(data, dh.gather_array(c_fields[1].
→name).mean())
```

B.5.3. Run the simulation without fluctuations

[20]:
```
init_fields(dens_init)

sync_conc()
data_no_fluctuations=[]
for time in range(time_end):
    dh.run_kernel(reaction_kernel_no_fluctuations, **params)
```

B. Fluctuating advection-diffusion-reaction *pystencils* script

```
    for i in range(species):
        dh.run_kernel(flux_kernels_no_fluctuations[i],
                    **params)
        dh.run_kernel(continuity_kernels[i])
    dh.run_kernel(reaction_continuity_kernel)
    sync_conc()
    if(time%save_time==0):
        data_no_fluctuations = np.
↪append(data_no_fluctuations, dh.gather_array(c_fields[1].
↪name).mean())
```

B.5.4. Plot the average product density over time

```
[21]: def g(t,r,n0,fac=1):
          return 1/fac*(n0- (1/(fac * r*t+(1/n0))))
      def g2(t,r,n0, fac=1):
          return 1/fac*(n0 + n0/(n0 - (n0 + 1)*np.exp(fac * r*t)))

      x = np.linspace(0,time_end*params['dt'],time_end//save_time)
      y_with_fluct = g2(x, params['gamma'], dens_init[0], 2.0)
      y_without_fluct = g(x, params['gamma'], dens_init[0], 2.0)
      plt.plot(x,y_with_fluct,label="theory with fluctuations")
      plt.plot(x,y_without_fluct,label="theory without␣
      ↪fluctuations")
      plt.plot(x[::20],data[::20],'o',label="simulation with␣
      ↪fluctuations")
      plt.plot(x[::20],data_no_fluctuations[::
      ↪20],'o',label="simulation_without fluctuations")
      plt.legend()
```

[21]: <matplotlib.legend.Legend at 0x7fd4b4df5cd0>

162

B.5. Influence of the fluctuations on the reaction rate
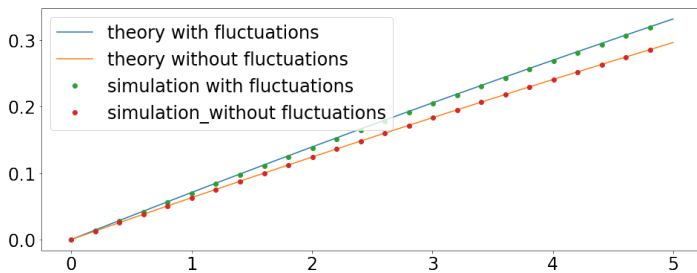
Bibliography

[1] Jens Hagen. *Industrial Catalysis: A Practical Approach, 3rd Edition.* Wiley, 2015.

[2] Felix Ziegler, Johannes Teske, Iris Elser, Michael Dyballa, Wolfgang Frey, Hamzeh Kraus, Niels Hansen, Julia Rybka, Ulrich Tallarek, and Michael R. Buchmeiser. Olefin metathesis in confined geometries: A biomimetic approach toward selective macrocyclization. *Journal of the American Chemical Society*, 141(48):19014–19022, nov 2019. `https://doi.org/10.1021/jacs.9b08776`.

[3] Felix Ziegler, Hamzeh Kraus, Mathis J. Benedikter, Dongren Wang, Johanna R. Bruckner, Michal Nowakowski, Kilian Weißer, Helena Solodenko, Guido Schmitz, Matthias Bauer, Niels Hansen, and Michael R. Buchmeiser. Confinement effects for efficient macrocyclization reactions with supported cationic molybdenum imido alkylidene n-heterocyclic carbene complexes. *ACS Catalysis*, 11(18):11570–11578, sep 2021. `https://doi.org/10.1021/acscatal.1c03057`.

[4] Barry E. Smith. Nitrogenase reveals its inner secrets. *Science*, 297(5587):1654–1655, sep 2002. `https://doi.org/10.1126/science.1076659`.

[5] Brian P. Callahan and Brian G. Miller. OMP decarboxylase—an enigma persists. *Bioorganic Chemistry*,

35(6):465–469, dec 2007. `https://doi.org/10.1016/j.bioorg.2007.07.004`.

[6] W KAEDING. Selective alkylation of toluene with methanol to produce para-xylene. *Journal of Catalysis*, 67(1):159–174, jan 1981. `https://doi.org/10.1016/0021-9517(81)90269-4`.

[7] Jian Zhang, Liang Wang, Yi Shao, Yanqin Wang, Bruce C. Gates, and Feng-Shou Xiao. A pd@zeolite catalyst for nitroarene hydrogenation with high product selectivity by sterically controlled adsorption in the zeolite micropores. *Angewandte Chemie International Edition*, 56(33):9747–9751, aug 2017. `https://doi.org/10.1002/anie.201703938`.

[8] Martin Hartmann and Marcus Fischer. Amino-functionalized basic catalysts with MIL-101 structure. *Microporous and Mesoporous Materials*, 164:38–43, dec 2012. `https://doi.org/10.1016/j.micromeso.2012.06.044`.

[9] Sabine Opelt, Verena Krug, Jan Sonntag, Michael Hunger, and Elias Klemm. Investigations on stability and reusability of [pd(2-pymo)2]n as hydrogenation catalyst. *Microporous and Mesoporous Materials*, 147(1):327–333, jan 2012. `https://doi.org/10.1016/j.micromeso.2011.07.003`.

[10] Frédéric Hapiot, Anne Ponchel, Sébastien Tilloy, and Eric Monflier. Cyclodextrins and their applications in aqueous-phase metal-catalyzed reactions. *Comptes Ren-*

dus Chimie, 14(2-3):149–166, feb 2011. `https://doi.org/10.1016/j.crci.2010.04.003`.

[11] Sebastian T. Emmerling, Robin Schuldt, Sebastian Bette, Liang Yao, Robert E. Dinnebier, Johannes Kästner, and Bettina V. Lotsch. Interlayer interactions as design tool for large-pore COFs. *Journal of the American Chemical Society*, 143(38):15711–15722, sep 2021. `https://doi.org/10.1021/jacs.1c06518`.

[12] Sebastian T. Emmerling, Felix Ziegler, Felix R. Fischer, Roland Schoch, Matthias Bauer, Bernd Plietker, Michael R. Buchmeiser, and Bettina V. Lotsch. Olefin metathesis in confinement: Towards covalent organic framework scaffolds for increased macrocyclization selectivity. *Chemistry – A European Journal*, 28(8), jan 2022. `https://doi.org/10.1002/chem.202104108`.

[13] Ann-Katrin Beurer, Manuel Kirchhof, Johanna R. Bruckner, Wolfgang Frey, Angelika Baro, Michael Dyballa, Frank Giesselmann, Sabine Laschat, and Yvonne Traa. Efficient and spatially controlled functionalization of SBA-15 and initial results in asymmetric Rh-catalyzed 1,2-additions under confinement. *ChemCatChem*, 13(10):2407–2419, apr 2021. `https://doi.org/10.1002/cctc.202100229`.

[14] Daniel Beinke, Felicitas Bürger, Helena Solodenko, Rachana Acharya, Hagen Klauk, and Guido Schmitz. Extracting the shape of nanometric field emitters. *Nanoscale*, 12(4):2820–2832, 2020. `https://doi.org/10.1039/c9nr08226c`.

Bibliography

[15] Patrick Stender, Baptiste Gault, Tim M Schwarz, Eric V
Woods, Se-Ho Kim, Jonas Ott, Leigh T Stephenson,
Guido Schmitz, Christoph Freysoldt, Johannes Kästner,
and Ayman A El-Zoka. Status and direction of atom
probe analysis of frozen liquids. *Microscopy and Mi-
croanalysis*, 28(4):1150–1167, aug 2022. `https://doi.
org/10.1017/s1431927621013994`.

[16] Carolin Rieg, Daniel Dittmann, Zheng Li, Alan Kurtz,
Elif Kaya, Stefan Peters, Benny Kunkel, Magdalena
Parlinska-Wojtan, Sebastian Wohlrab, Ali M. Abdel-
Mageed, and Michael Dyballa. Introducing a novel
method for probing accessibility, local environment, and
spatial distribution of oxidative sites on solid cata-
lysts using trimethylphosphine. *The Journal of Physical
Chemistry C*, 126(31):13213–13223, aug 2022. `https:
//doi.org/10.1021/acs.jpcc.2c04114`.

[17] Manoj K. Kesharwani, Iris Elser, Janis V. Musso, Mi-
chael R. Buchmeiser, and Johannes Kästner. Reaction
mechanism of ring-closing metathesis with a cationic
molybdenum imido alkylidene *N*-heterocyclic carbene
catalyst. *Organometallics*, 39(17):3146–3159, aug 2020.
`https://doi.org/10.1021/acs.organomet.0c00311`.

[18] Christopher Kessler, Robin Schuldt, Sebastian Emmer-
ling, Bettina V. Lotsch, Johannes Kästner, Joachim
Gross, and Niels Hansen. Influence of layer slipping on
adsorption of light gases in covalent organic frameworks:
A combined experimental and computational study. *Mi-
croporous and Mesoporous Materials*, 336:111796, may

2022. `https://doi.org/10.1016/j.micromeso.2022.111796`.

[19] Hamzeh Kraus and Niels Hansen. An atomistic view on the uptake of aromatic compounds by cyclodextrin immobilized on mesoporous silica. *Adsorption*, 28 (3-4):125–136, mar 2022. `https://doi.org/10.1007/s10450-022-00356-w`.

[20] Florian Weik, Rudolf Weeber, Kai Szuttor, Konrad Breitsprecher, Joost de Graaf, Michael Kuron, Jonas Landsgesell, Henri Menke, David Sean, and Christian Holm. ESPResSo 4.0 – an extensible software package for simulating soft matter systems. *European Physical Journal Special Topics*, 227(14):1789–1816, 2019. `https://doi.org/10.1140/epjst/e2019-800186-9`.

[21] Martin Bauer, Johannes Hötzer, Dominik Ernst, Julian Hammer, Marco Seiz, Henrik Hierl, Jan Hönig, Harald Köstler, Gerhard Wellein, Britta Nestler, and Ulrich Rüde. Code generation for massively parallel phase-field simulations. In *Proceedings of the International Conference for High Performance Computing, Networking, Storage and Analysis*, New York, 2019. Association for Computing Machinery. ISBN 9781450362290. `https://doi.org/10.1145/3295500.3356186`.

[22] Jordi Burés. What is the order of a reaction? *Topics in Catalysis*, 60(8):631–633, may 2017. `https://doi.org/10.1007/s11244-017-0735-y`.

[23] McNaught and Wilkinson. *IUPAC. Compendium of Chemical Terminology, 2nd ed. (the "Gold Book")*.

1997. ISBN 0-9678550-9-8. `https://doi.org/10.1351/goldbook`. URL `http://goldbook.iupac.org`.

[24] Marie Deckers, Dieter Deforce, Marie-Alice Fraiture, and Nancy H.C. Roosens. Genetically modified microorganisms for industrial food enzyme production: An overview. *Foods*, 9(3):326, mar 2020. `https://doi.org/10.3390/foods9030326`.

[25] Congcong Yin, Ya-Fei Jiang, Fanping Huang, Cong-Qiao Xu, Yingmin Pan, Shuang Gao, Gen-Qiang Chen, Xiaobing Ding, Shao-Tao Bai, Qiwei Lang, Jun Li, and Xumu Zhang. A 13-million turnover-number anionic ir-catalyst for a selective industrial route to chiral nicotine. *Nature Communications*, 14(1), jun 2023. `https://doi.org/10.1038/s41467-023-39375-8`.

[26] Bert M. Weckhuysen and Jihong Yu. Recent advances in zeolite chemistry and catalysis. *Chemical Society Reviews*, 44(20):7022–7024, 2015. `https://doi.org/10.1039/c5cs90100f`.

[27] Frédéric Goettmann and Clément Sanchez. How does confinement affect the catalytic activity of mesoporous materials? *Journal of Materials Chemistry*, 17(1):24–30, 2007. `https://doi.org/10.1039/b608748p`.

[28] Zoltan Blum, Stephen T. Hyde, and Barry W. Ninham. Adsorption in zeolites, dispersion self-energy, and gaussian curvature. *The Journal of Physical Chemistry*, 97(3):661–665, jan 1993. `https://doi.org/10.1021/j100105a021`.

[29] Michito Yoshizawa, Masazumi Tamura, and Makoto Fujita. Diels-alder in aqueous molecular hosts: Unusual regioselectivity and efficient catalysis. *Science*, 312 (5771):251–254, apr 2006. `https://doi.org/10.1126/science.1124985`.

[30] Yuki Nishioka, Takumi Yamaguchi, Masaki Kawano, and Makoto Fujita. Asymmetric [2 + 2] olefin cross photoaddition in a self-assembled host with remote chiral auxiliaries. *Journal of the American Chemical Society*, 130 (26):8160–8161, jun 2008. `https://doi.org/10.1021/ja802818t`.

[31] Development of the metathesis method in organic synthesis. URL `https://www.nobelprize.org/uploads/2018/06/advanced-chemistryprize2005.pdf`.

[32] David Hughes, Philip Wheeler, and Doina Ene. Olefin metathesis in drug discovery and development—examples from recent patent literature. *Organic Process Research & Development*, 21(12):1938–1962, nov 2017. `https://doi.org/10.1021/acs.oprd.7b00319`.

[33] R.L. Banks, D.S. Banaslak, P.S. Hudson, and J.R. Norell. Specialty chemicals via olefin metathesis. *Journal of Molecular Catalysis*, 15(1-2):21–33, apr 1982. `https://doi.org/10.1016/0304-5102(82)80002-3`.

[34] J Mol. Industrial applications of olefin metathesis. *Journal of Molecular Catalysis A: Chemical*, 213(1):39–45, apr 2004. `https://doi.org/10.1016/j.molcata.2003.10.049`.

[35] Eric Marsault and Mark L. Peterson. Macrocycles are great cycles: Applications, opportunities, and challenges of synthetic macrocycles in drug discovery. *Journal of Medicinal Chemistry*, 54(7):1961–2004, apr 2011. `https://doi.org/10.1021/jm1012374`.

[36] Vicente Marti-Centelles, Mrituanjay D. Pandey, M. Isabel Burguete, and Santiago V. Luis. Macrocyclization reactions: The importance of conformational, configurational, and template-induced preorganization. *Chemical Reviews*, 115(16):8736–8834, aug 2015. `https://doi.org/10.1021/acs.chemrev.5b00056`.

[37] Philipp Ermert. Design, properties and recent application of macrocycles in medicinal chemistry. *CHIMIA International Journal for Chemistry*, 71(10):678–702, oct 2017. `https://doi.org/10.2533/chimia.2017.678`.

[38] Carolyn S. Higman, Justin A. M. Lummiss, and Deryn E. Fogg. Olefin metathesis at the dawn of implementation in pharmaceutical and specialty-chemicals manufacturing. *Angewandte Chemie International Edition*, 55(11):3552–3565, feb 2016. `https://doi.org/10.1002/anie.201506846`.

[39] Miao Yu, Sha Lou, and Francisco Gonzalez-Bobes. Ring-closing metathesis in pharmaceutical development: Fundamentals, applications, and future directions. *Organic Process Research & Development*, 22(8):918–946, jun 2018. `https://doi.org/10.1021/acs.oprd.8b00093`.

[40] Carolyn S. Higman, Daniel L. Nascimento, Benjamin J. Ireland, Stephan Aud?rsch, Gwendolyn A. Bailey,

Robert McDonald, and Deryn E. Fogg. Chelate-assisted ring-closing metathesis: A strategy for accelerating macrocyclization at ambient temperatures. *Journal of the American Chemical Society*, 140(5):1604–1607, jan 2018. https://doi.org/10.1021/jacs.7b13257.

[41] Homer Jacobson, Charles O. Beckmann, and Walter H. Stockmayer. Intramolecular reaction in polycondensations. II. ring-chain equilibrium in polydecamethylene adipate. *The Journal of Chemical Physics*, 18(12):1607–1612, dec 1950. https://doi.org/10.1063/1.1747548.

[42] Sebastien Monfette and Deryn E. Fogg. Equilibrium ring-closing metathesis. *Chemical Reviews*, 109(8):3783–3816, aug 2009. https://doi.org/10.1021/cr800541y.

[43] Choon Woo Lee and Robert H. Grubbs. Formation of macrocycles via ring-closing olefin metathesis. *The Journal of Organic Chemistry*, 66(21):7155–7158, sep 2001. https://doi.org/10.1021/jo0158480.

[44] Adrian Sytniczuk, Michał Dąbrowski, Łukasz Banach, Mateusz Urban, Sylwia Czarnocka-Śniadała, Mariusz Milewski, Anna Kajetanowicz, and Karol Grela. At long last: Olefin metathesis macrocyclization at high concentration. *Journal of the American Chemical Society*, 140 (28):8895–8901, jun 2018. https://doi.org/10.1021/jacs.8b04820.

[45] Markus Jeschek, Raphael Reuter, Tillmann Heinisch, Christian Trindler, Juliane Klehr, Sven Panke, and Thomas R. Ward. Directed evolution of artificial

metalloenzymes for in vivo metathesis. *Nature*, 537 (7622):661–665, aug 2016. `https://doi.org/10.1038/nature19114`.

[46] Michael Rubinstein and Ralph H. Colby. *Polymer Physics*. Oxford University Press, Oxford, UK, 2003.

[47] Prince E. Rouse. A Theory of the Linear Viscoelastic Properties of Dilute Solutions of Coiling Polymers. 21 (7):1272–1280. ISSN 0021-9606. `https://doi.org/10.1063/1.1699180`. URL `https://aip.scitation.org/doi/10.1063/1.1699180`.

[48] Albert Einstein. Über die von der molekularkinetischen Theorie der Wärme geforderte Bewegung von in ruhenden Flüssigkeiten suspendierten Teilchen. *Annalen der Physik*, 322(8):549–560, 1905. `https://doi.org/10.1002/andp.19053220806`.

[49] Marian von Smoluchowski. Zur kinetischen theorie der brownschen molekularbewegung und der suspensionen. *Annalen der Physik*, 326(14):756–780, 1906. `https://doi.org/10.1002/andp.19063261405`.

[50] I. Teraoka. *Polymer Solutions: An Introduction to Physical Properties*. Wiley, 2002. ISBN 9780471389293. URL `http://books.google.com.au/books?id=9DpRAAAAMAAJ`.

[51] B. H. Zimm. Dynamics of polymer molecules in dilute solution: Viscoelasticity, flow birefringence and dielectric loss. *The Journal of Chemical Physics*, 24(2):269–278, 1956.

[52] Masao Doi and Samuel Frederick Edwards. *The Theory of Polymer Dynamics*. Clarendon Press: Oxford, 1986. ISBN 9780198519768.

[53] P. J. Flory. *Principles of Polymer Chemistry*. Cornell University Press, Ithaca, NY, 1953.

[54] Gordon E. Moore. Cramming more components onto integrated circuits, reprinted from electronics, volume 38, number 8, april 19, 1965, pp.114 ff. *IEEE Solid-State Circuits Society Newsletter*, 11(3):33–35, sep 2006. `https://doi.org/10.1109/n-ssc.2006.4785860`.

[55] P. Hohenberg and W. Kohn. Inhomogeneous electron gas. *Physical Review*, 136(3):864–871, 1964.

[56] W. Kohn and L. J. Sham. Self-consistent equations including exchange and correlation effects. *Physical Review*, 140(4A):A1133–A1138, November 1965. `https://doi.org/10.1103/PhysRev.140.A1133`.

[57] Johannes Diderik van der Waals. *Over de continuïteit van den Gas- en Vloeistoftoestand*. PhD thesis, Hogeschool Leiden, Leiden, June 1873. URL `https://books.google.com/books?id=1A1jAAAAcAAJ`.

[58] F. London. The general theory of molecular forces. *Transactions of the Faraday Society*, 33:8–26, 1937. `https://doi.org/10.1039/tf937330008b`.

[59] Wolfgang Pauli. Über den zusammenhang des abschlusses der elektronengruppen im atom mit der komplexstruktur der spektren. *Zeitschrift für Physik*, 31(1):

765–783, Feb 1925. ISSN 0044-3328. `https://doi.org/ 10.1007/BF02980631`.

[60] J. E. Lennard-Jones. Cohesion. *Proceedings of the Physical Society*, 43 pt. 5(240):461–482, September 1931. `https://doi.org/10.1088/0959-5309/43/5/301`.

[61] John D. Weeks, David Chandler, and Hans C. Andersen. Role of repulsive forces in determining the equilibrium structure of simple liquids. *The Journal of Chemical Physics*, 54(12):5237–5247, June 1971. `https: //doi.org/10.1063/1.1674820`.

[62] Harold R. Warner, Jr. Kinetic theory and rheology of dilute suspensions of finitely extendible dumbbells. *Industrial & Engineering Chemistry Fundamentals*, 11 (3):379–387, August 1972. `https://doi.org/10.1021/ i160043a017`.

[63] Kurt Kremer and Gary S. Grest. Dynamics of entangled linear polymer melts: A molecular-dynamics simulation. *The Journal of Chemical Physics*, 92(8):5057–5086, 1990. `https://doi.org/10.1063/1.458541`.

[64] William L. Jorgensen and Julian Tirado-Rives. The OPLS potential functions for proteins. Energy minimizations for crystals of cyclic peptides and crambin. *Journal of the American Chemical Society*, 110(6):1657–1666, 1988. `https://doi.org/10.1021/ja00214a001`.

[65] W. D. Cornell, P Cieplak, C. I. Bayly, I. R. Gould, K. M. Merz J.R, D. M. Ferguson, D. C. Spellmeyer, T. Fox, J. W. Caldwell, and P. A. Kollman. A second generation

force field for the simulation of proteins, nucleic acids, and organic molecules. *Journal of the American Chemical Society*, 117:5179–5197, 1995.

[66] S. A. Adelman and J. D. Doll. Generalized Langevin equation approach for atom/solid-surface scattering: General formulation for classical scattering off harmonic solids. *The Journal of Chemical Physics*, 64(6):2375–2388, 1976. `https://doi.org/10.1063/1.432526`.

[67] Paul Langevin. Sur la théorie du mouvement brownien. *Comptes rendus de l'Académie des sciences Paris*, 146 (530-533), 1908.

[68] Siewert J. Marrink, H. Jelger Risselada, Serge Yefimov, D. Peter Tieleman, and Alex H. de Vries. The MARTINI force field: Coarse grained model for biomolecular simulations. *Journal of Physical Chemistry B*, 111 (27):7812–7824, jul 2007. ISSN 1520-6106. `https://doi.org/10.1021/jp071097f`.

[69] P. P. Ewald. Die Berechnung optischer und elektrostatischer Gitterpotentiale. *Annalen der Physik*, 369 (3):253–287, 1921. `https://doi.org/10.1002/andp.19213690304`.

[70]

[71] Adolf Fick. Ueber diffusion. *Annalen der Physik*, 170(1):59–86, 1855. `https://doi.org/10.1002/andp.18551700105`.

[72] Georg Rempfer, Sascha Ehrhardt, Nadanai Laohakunakorn, Gary B. Davies, Ulrich F. Keyser, Christian

Holm, and Joost de Graaf. Selective trapping of DNA using glass microcapillaries. *Langmuir*, 32(33):8525–8532, 2016. `https://doi.org/10.1021/acs.langmuir.6b02071`.

[73] Fabrizio Capuani, Ignacio Pagonabarraga, and Daan Frenkel. Discrete solution of the electrokinetic equations. *The Journal of Chemical Physics*, 121:973–986, 2004. `https://doi.org/10.1063/1.1760739`.

[74] Rudolf Weeber, Jean-Noël Grad, David Beyer, Pablo M. Blanco, Patrick Kreissl, Alexander Reinauer, Ingo Tischler, Peter Košovan, and Christian Holm. ESPResSo, a versatile open-source software package for simulating soft matter systems. In *Reference Module in Chemistry, Molecular Sciences and Chemical Engineering*. Elsevier, 2023. ISBN 978-0-12-409547-2. `https://doi.org/10.1016/B978-0-12-821978-2.00103-3`.

[75] P. Debye and E. Hückel. Zur Theorie der Elektrolyte. I. Gefrierpunktserniedrigung und verwandte Erscheinungen. *Physikalische Zeitschrift*, 24(9):185–206, 1923.

[76] I. Pagonabarraga, B. Rotenberg, and D. Frenkel. Recent advances in the modelling and simulation of electrokinetic effects: bridging the gap between atomistic and macroscopic descriptions. *Physical Chemistry Chemical Physics*, 12:9566–9580, 2010. `https://doi.org/10.1039/C004012F`.

[77] Benjamin Rotenberg and Ignacio Pagonabarraga. Electrokinetics: insights from simulation on the microscopic

scale. *Molecular Physics*, 111(7):827–842, 2013. `https://doi.org/10.1080/00268976.2013.791731`.

[78] Michael Kuron, Georg Rempfer, Florian Schornbaum, Martin Bauer, Christian Godenschwager, Christian Holm, and Joost de Graaf. Moving charged particles in lattice Boltzmann-based electrokinetics. *The Journal of Chemical Physics*, 145(21):214102, 2016. `https://doi.org/10.1063/1.4968596`.

[79] Hirofumi Daiguji, Yukiko Oka, and Katsuhiro Shirono. Nanofluidic diode and bipolar transistor. *Nano Letters*, 5(11):2274–2280, November 2005. ISSN 1530-6984. `https://doi.org/10.1021/nl051646y`.

[80] Georg Rempfer, Sascha Ehrhardt, Christian Holm, and Joost de Graaf. Nanoparticle translocation through conical nanopores: A finite element study of electrokinetic transport. *Macromolecular Theory and Simulations*, 26(1):1600051, 2017. `https://doi.org/10.1002/mats.201600051`.

[81] Nicolas Rivas, Stefan Frijters, Ignacio Pagonabarraga, and Jens Harting. Mesoscopic electrohydrodynamic simulations of binary colloidal suspensions. *The Journal of Chemical Physics*, 148(14):144101, 2018. `https://doi.org/10.1063/1.5020377`.

[82] Changho Kim, Andy Nonaka, John B. Bell, Alejandro L. Garcia, and Aleksandar Donev. Fluctuating hydrodynamics of reactive liquid mixtures. *The Journal of Chemical Physics*, 149(8):084113, aug 2018. `https://doi.org/10.1063/1.5043428`.

[83] Michael Kuron, Patrick Kreissl, and Christian Holm. Toward understanding of self-electrophoretic propulsion under realistic conditions: From bulk reactions to confinement effects. *Accounts of Chemical Research*, 51 (12):2998–3005, 2018. `https://doi.org/10.1021/acs.accounts.8b00285`.

[84] Joost de Graaf, Georg Rempfer, and Christian Holm. Diffusiophoretic self-propulsion for partially catalytic spherical colloids. *IEEE Transactions on NanoBioscience*, 14(3):272–288, apr 2015. ISSN 1536-1241. `https://doi.org/10.1109/TNB.2015.2403255`.

[85] Aidan T. Brown and Wilson C. K. Poon. Ionic effects in self-propelled Pt-coated janus swimmers. *Soft Matter*, 10(22):4016–4027, 2014. `https://doi.org/10.1039/c4sm00340c`.

[86] Sergi Molins, David Trebotich, Carl I. Steefel, and Chaopeng Shen. An investigation of the effect of pore scale flow on average geochemical reaction rates using direct numerical simulation. *Water Resources Research*, 48(3), mar 2012. `https://doi.org/10.1029/2011wr011404`.

[87] David A. Kessler and Herbert Levine. Fluctuation-induced diffusive instabilities. *Nature*, 394(6693):556–558, aug 1998. `https://doi.org/10.1038/29020`.

[88] A. Lemarchand and B. Nowakowski. Do the internal fluctuations blur or enhance axial segmentation? *EPL (Europhysics Letters)*, 94(4):48004, may 2011. `https://doi.org/10.1209/0295-5075/94/48004`.

[89] Amit Kumar Bhattacharjee, Kaushik Balakrishnan, Alejandro L. Garcia, John B. Bell, and Aleksandar Donev. Fluctuating hydrodynamics of multi-species reactive mixtures. *The Journal of Chemical Physics*, 142 (22):224107, jun 2015. `https://doi.org/10.1063/1.4922308`.

[90] David Fange and Johan Elf. Noise-induced min phenotypes in e. coli. *PLoS Computational Biology*, 2(6):e80, jun 2006. `https://doi.org/10.1371/journal.pcbi.0020080`.

[91] Aleksandar Donev, John B Bell, Anton de la Fuente, and Alejandro L Garcia. Enhancement of diffusive transport by non-equilibrium thermal fluctuations. *Journal of Statistical Mechanics: Theory and Experiment*, 2011 (06):P06014, jun 2011. `https://doi.org/10.1088/1742-5468/2011/06/p06014`.

[92] Aleksandar Donev, Andy Nonaka, Yifei Sun, Thomas Fai, Alejandro Garcia, and John Bell. Low mach number fluctuating hydrodynamics of diffusively mixing fluids. *Communications in Applied Mathematics and Computational Science*, 9(1):47–105, may 2014. `https://doi.org/10.2140/camcos.2014.9.47`.

[93] Burkhard Dünweg, Ulf D. Schiller, and Anthony J. C. Ladd. Statistical mechanics of the fluctuating lattice Boltzmann equation. *Physical Review E*, 76(3): 036704, 2007. `https://doi.org/10.1103/PhysRevE.76.036704`.

Bibliography

[94] B. Dünweg, U. D. Schiller, and A. J. C. Ladd. Progress in the understanding of the fluctuating lattice Boltzmann equation. *Computer Physics Communications*, 180(4): 605–608, 2009.

[95] Mingge Deng, Faisal Tushar, Luis Bravo, Anindya Ghoshal, George Karniadakis, and Zhen Li. Theory and simulation of electrokinetic fluctuations in electrolyte solutions at the mesoscale. *Journal of Fluid Mechanics*, 942, May 2022. `https://doi.org/10.1017/jfm.2022.377`.

[96] Jean-Philippe Péraud, Andy Nonaka, Anuj Chaudhri, John B Bell, Aleksandar Donev, and Alejandro L Garcia. Low mach number fluctuating hydrodynamics for electrolytes. *Physical Review Fluids*, 1(7):074103, 2016. `https://doi.org/10.1103/PhysRevFluids.1.074103`.

[97] Aleksandar Donev, Andrew J. Nonaka, Changho Kim, Alejandro L. Garcia, and John B. Bell. Fluctuating hydrodynamics of electrolytes at electroneutral scales. *Physical Review Fluids*, 4(4), apr 2019. `https://doi.org/10.1103/physrevfluids.4.043701`.

[98] D. R. Ladiges, A. Nonaka, K. Klymko, G. C. Moore, J. B. Bell, S. P. Carney, A. L. Garcia, S. R. Natesh, and A. Donev. Discrete ion stochastic continuum overdamped solvent algorithm for modeling electrolytes. *Physical Review Fluids*, 6(4), apr 2021. `https://doi.org/10.1103/physrevfluids.6.044309`.

[99] David S Dean. Langevin equation for the density of a system of interacting Langevin processes. *Journal of Phys-*

ics A, 29(24):L613, 1996. `https://doi.org/10.1088/0305-4470/29/24/001`.

[100] Bernt Øksendal. *Stochastic Differential Equations.* Springer Berlin Heidelberg, 2003. `https://doi.org/10.1007/978-3-642-14394-6`.

[101] Daniel T. Gillespie. The chemical Langevin equation. *The Journal of Chemical Physics*, 113(1):297–306, jul 2000. `https://doi.org/10.1063/1.481811`.

[102] Georg Rempfer, Gary B. Davies, Christian Holm, and Joost de Graaf. Reducing spurious flow in simulations of electrokinetic phenomena. *The Journal of Chemical Physics*, 145(4):044901, 2016. `https://doi.org/10.1063/1.4958950`.

[103] Axel Arnold, Olaf Lenz, Stefan Kesselheim, Rudolf Weeber, Florian Fahrenberger, Dominic Röhm, Peter Košovan, and Christian Holm. ESPResSo 3.1 – molecular dynamics software for coarse-grained models. In Michael Griebel and Marc Alexander Schweitzer, editors, *Meshfree Methods for Partial Differential Equations VI*, volume 89 of *Lecture Notes in Computational Science and Engineering*, pages 1–23. Springer Berlin Heidelberg, 2013. `https://doi.org/10.1007/978-3-642-32979-1_1`.

[104] Irina Ginzburg, Frederik Verhaeghe, and Dominique d'Humières. Two-relaxation-time lattice Boltzmann scheme: About parametrization, velocity, pressure and mixed boundary conditions. *Communications in*

Computational Physics, 3(2):427–478, 2008. URL https://www.global-sci.com/intro/article_detail/cicp/7862.html.

[105] H. J. Limbach, A. Arnold, B. A. Mann, and C. Holm. ES-PResSo – an extensible simulation package for research on soft matter systems. *Computer Physics Communications*, 174(9):704–727, May 2006. https://doi.org/10.1016/j.cpc.2005.10.005.

[106] Dominic Roehm, Kai Kratzer, and Axel Arnold. Heterogeneous and homogeneous crystallization of soft spheres in suspension. In Wolfgang E. Nagel, Dietmar H. Kröner, and Michael M. Resch, editors, *High Performance Computing in Science and Engineering '13*, pages 33–52. Springer International Publishing, 2013. ISBN 978-3-319-02165-2. https://doi.org/10.1007/978-3-319-02165-2_3.

[107] Martin Bauer, Harald Köstler, and Ulrich Rüde. lbmpy: Automatic code generation for efficient parallel lattice Boltzmann methods. *Journal of Computational Science*, 49:101269, 2021. ISSN 1877-7503. https://doi.org/10.1016/j.jocs.2020.101269.

[108] Phillip Colella. Multidimensional upwind methods for hyperbolic conservation laws. *Journal of Computational Physics*, 87(1):171–200, 1990. https://doi.org/10.1016/0021-9991(90)90233-Q.

[109] John K. Salmon, Mark A. Moraes, Ron O. Dror, and David E. Shaw. Parallel random numbers: As easy as 1,

2, 3. In *Proceedings of 2011 International Conference for High Performance Computing, Networking, Storage and Analysis*. ACM Press, November 2011. `https://doi.org/10.1145/2063384.2063405`.

[110] Vladimir Lobaskin and Burkhard Dünweg. A new model for simulating colloidal dynamics. *New Journal of Physics*, 6:54, May 2004. `https://doi.org/10.1088/1367-2630/6/1/054`.

[111] Anthony JC Ladd. Numerical simulations of particulate suspensions via a discretized Boltzmann equation. part 2. numerical results. *Journal of Fluid Mechanics*, 271: 311–339, 1994.

[112] Ingo Tischler, Christian Holm, Rudolf Weeber, Michael Kuron, Florian Weik, and Robert Kaufmann. Replication data of C6 group for: "A thermalized electrokinetics model including stochastic reactions suitable for multiscale simulations of reaction-advection-diffusion systems", 2021.

[113] S. Chandrasekhar. Stochastic problems in physics and astronomy. *Reviews of Modern Physics*, 15:1, 1943.

[114] Kim Bolton, Bosio, William L. Hase, William F. Schneider, and Kenneth C. Hass. Comparison of explicit and united atom models for alkane chains physisorbed on α-al2o3(0001). *The Journal of Physical Chemistry B*, 103(19):3885–3895, may 1999. `https://doi.org/10.1021/jp9840026`.

[115] Adri C. T. van Duin, Siddharth Dasgupta, Francois Lorant, and William A. Goddard. Reaxff: A reactive force field for hydrocarbons. *The Journal of Physical Chemistry A*, 105:9396–9409, 2001.

[116] K. Chenoweth, A. C. T. van Duin, and W. A. Goddard III. Reaxff reactive force field for molecular dynamics simulation of hydrocarbon oxidation. *Journal of Physical Chemistry A*, 112, 2008.

[117] Thomas P Senftle, Sungwook Hong, Md Mahbubul Islam, Sudhir B Kylasa, Yuanxia Zheng, Yun Kyung Shi, Chad Junkermeier, Roman Engel-Herbert, Michael J Janik, Hasan Metin Aktulga, Toon Verstraelen, Ananth Grama, and Adri C T van Duin. The ReaxFF reactive force-field: development, applications and future directions. *Computational Materials*, 2:15011, 2016. `https://doi.org/10.1038/npjcompumats.2015.11`.

[118] Johannes Schöneberg and Frank Noé. ReaDDy - a software for particle-based reaction-diffusion dynamics in crowded cellular environments. *PLoS ONE*, 8(9):e74261, sep 2013. `https://doi.org/10.1371/journal.pone.0074261`.

[119] Moritz Hoffmann, Christoph Fröhner, and Frank Noé. ReaDDy 2: Fast and flexible software framework for interacting-particle reaction dynamics. *PLOS Computational Biology*, 15(2):e1006830, feb 2019. `https://doi.org/10.1371/journal.pcbi.1006830`.

[120] Reinier L. C. Akkermans, So/ren Toxvaerd, and W. J. Briels. Molecular dynamics of polymer growth. *The*

Journal of Chemical Physics, 109(7):2929–2940, aug 1998. `https://doi.org/10.1063/1.476845`.

[121] Karim Farah, Hossein A. Karimi-Varzaneh, Florian Müller-Plathe, and Michael C. Böhm. Reactive molecular dynamics with material-specific coarse-grained potentials: Growth of polystyrene chains from styrene monomers. *The Journal of Physical Chemistry B*, 114(43):13656–13666, oct 2010. `https://doi.org/10.1021/jp107001e`.

[122] Pierre de Buyl and Erik Nies. A parallel algorithm for step- and chain-growth polymerization in molecular dynamics. *The Journal of Chemical Physics*, 142 (13):134102, apr 2015. `https://doi.org/10.1063/1.4916313`.

[123] Jakub Krajniak, Zidan Zhang, Sudharsan Pandiyan, Eric Nies, and Giovanni Samaey. Coarse-grained molecular dynamics simulations of polymerization with forward and backward reactions. *Journal of Computational Chemistry*, 39(22):1764–1778, jun 2018. `https://doi.org/10.1002/jcc.25348`.

[124] Jean-Louis Hérisson and Yves Chauvin. Catalyse de transformation des oléfines par les complexes du tungstène. II. télomérisation des oléfines cycliques en présence d'oléfines acycliques. *Die Makromolekulare Chemie*, 141(1):161–176, February 1971. `https://doi.org/10.1002/macp.1971.021410112`.

[125] G. E. Norman and V. S. Filinov. Investigations of phase

transitions by a Monte Carlo method. 7(2):216–222, 1969.

[126] Ingo Tischler, Alexander Schlaich, and Christian Holm. The presence of a wall enhances the probability for ring-closing metathesis: Insights from classical polymer theory and atomistic simulations. *Macromolecular Theory and Simulations*, 30(2):2000076, 2021. `https://doi.org/10.1002/mats.202000076`.

[127] Ingo Tischler, Florian Weik, Robert Kaufmann, Michael Kuron, Rudolf Weeber, and Christian Holm. A thermalized electrokinetics model including stochastic reactions suitable for multiscale simulations of reaction–advection–diffusion systems. *Journal of Computational Science*, 63:101770, September 2022. `https://doi.org/10.1016/j.jocs.2022.101770`.

Acknowledgment

There are a lot of people without whom this PhD thesis would not be possible.

Bibliography

- I want to thank all my fellow PhD colleagues of the CRC for all the great exchanges at the seminars and status meetings.

- I thank my friends and fellow students Frank and ~~Bardak~~ Robin for our neat little Feierabendbier-sessions.

- I thank my friends for being there with me.

- I want to give a special tribute to my family for all their love and support.

Erklärung

Hiermit erkläre ich, dass ich diese Dissertation selbständig
verfasst habe. Alle verwendeten Quellen wurden angegeben.

Stuttgart, den

Ingo Tischler